UNIVERSITÉ DU LUXEMBOURG

PhD-FSTM-2020-74
The Faculty of Sciences, Technology and Medicine

DISSERTATION

Defence held on 16/11/2021 in Esch-sur-Alzette
to obtain the degree of

DOCTEUR DE L'UNIVERSITÉ DU LUXEMBOURG EN SCIENCES DE L'INGÉNIEUR

by

Li CHEN

Born on 1 July 1990 in Tiantai (China)

A QUASICONTINUUM APPROACH TOWARDS MECHANICAL SIMULATIONS OF PERIODIC LATTICE STRUCTURES

Dissertation defence committee

Dr Thierry J. Massart, dissertation supervisor
Professor, Université Libre du Bruxelles
Dr Stéphane P. A. Bordas, dissertation supervisor
Professor, Université du Luxembourg
Dr Andreas Zilian, Chairman
Professor, Université du Luxembourg
Dr Bertrand Francois, Vice Chairman
Professor, Université Libre du Bruxelles
Dr Michael Ortiz
Professor, California Institute of Technology
Dr Rémy Dendievel
Professor, Genoble, Institut National Polytechnique

Contents

Summary

Thanks to the advancement of additive manufacturing, periodic metallic lattice structures are gaining more and more attention. A major attraction of them is that their design can be tailored to specific applications by changing the basic repetitive pattern of the lattice, called the unit cell. This may involve the selection of optimal strut diameters and orientations, as well as the connectivity and strut lengths. Numerical simulation plays a vital role in understanding the mechanical behavior of metallic lattices and it enables the optimization of design parameters. However, conventional numerical modeling strategies in which each strut is represented by one or more beam finite elements yield prohibitively time-consuming simulations for metallic lattices in engineering-scale applications. The reasons are that millions of struts are involved, as well as that geometrical and material nonlinearities at the strut level need to be incorporated.

The aim of this thesis is the development of multi-scale quasicontinuum (QC) frameworks to substantially reduce the simulation time of nonlinear mechanical models of metallic lattices. For this purpose, this thesis generalizes the QC method by a multi-field interpolation enabling amongst others the representation of varying diameters in the struts' axial directions (as a consequence of the manufacturing process). The efficiency is further increased by a new adaptive scheme that automatically adjusts the model reduction whilst controlling the (elastic or elastoplastic) model's accuracy.

The capabilities of the proposed methodology are demonstrated using numerical examples, such as indentation tests and scratch tests, in which the lattice is modeled using geometrically nonlinear elastic and elastoplastic beam finite elements. They show that the multi-scale framework combines a high accuracy with substantial model reduction that are out of reach of direct numerical simulations.

1

Introduction

Periodic lattices are gaining more and more attention for their outstanding mechanical performances with respect to their weight, and for the flexibility of tailoring the shape of the lattice unit cell for specific applications. Computational modeling plays an indispensable role in predicting and designing periodic lattices. The main bottleneck of mechanical simulations of periodic lattices is the large computational model size for engineering applications: the direct numerical simulations include millions of struts. The aim of this thesis is to develop an adaptive generalized quasicontinuum framework that can achieve accurate and cheaper mechanical models for periodic lattices made of arbitrary shaped unit cells at a much lower computational cost than that of direct numerical simulations. The multi-scale quasicontinuum principle is employed because of its ability to incorporate localized mechanical phenomena in small fully resolved regions, while the lattice is coarse-grained in the remainder of the domain. This thesis proposes an adaptive generalization of the conventional quasicontinuum method to a multi-field like interpolation approach so that truly general, yet periodic unit cells can be incorporated.

1

1.1. Periodic lattices

Periodic lattices [1] are superior to bulk material in terms of weight-to-strength ratio because of their configurable sparsity (e.g. strut orientations, diameters and connectivity). This can ultimately enable their structural optimization for specific applications by selecting the underlying discrete topology, for instance selecting stretching dominated or bending dominated topologies. Consequently, more and more research developments in the automobile, aerospace and biomedical fields focus on lattice materials, also driven by the advancement of additive manufacturing technologies. For example, selective laser melting [2] is a relatively mature additive manufacturing technology for the production of such lattice materials. It has the capacity to fabricate metallic lattices with a controlled degree of quality (e.g. porosity) (see Fig. 1.1).

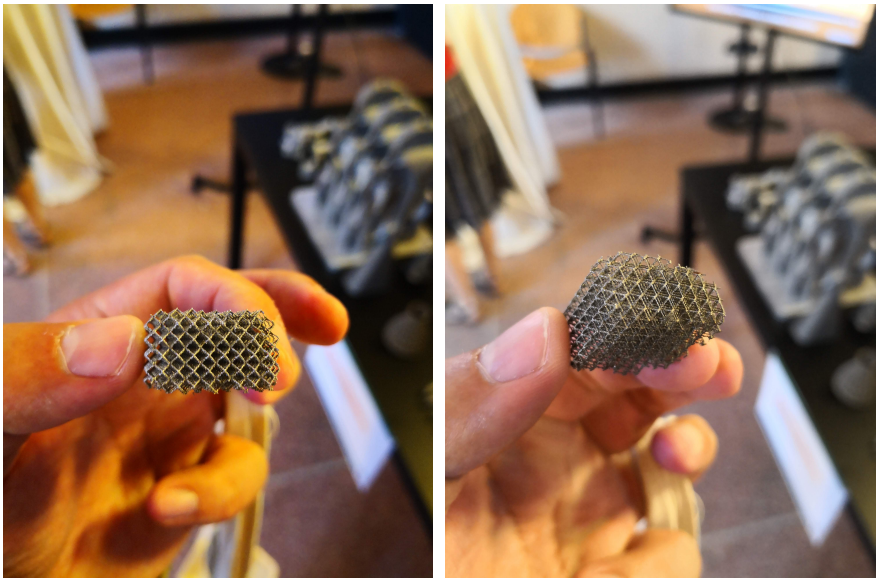

Figure 1.1: Metallic BCC (Body Centered Cubic) lattice on exhibition at II International Conference on Simulation for Additive Manufacturing in Pavia, Italy, 2019.

Topologically, a periodic lattice is organized by repeating a *unit cell* in three spatial directions. The unit cell consists of struts with a diameter that possibly varies along its length: a strut can for instance be manufactured more bulky at its extremities where it is connected to other struts. To optimize the configuration of the unit cell for a specific application, several design factors are intertwined, which include, but are not limited to, the size of the unit cell, the strut diameters, the strut orientations and the connection patterns of the struts (which also influence the relative density of the lattice).

A step prior to lattice topology tailoring is the ability to predict and understand the mechanical behavior of these materials – which are actually structures on the

small scale. The mechanical behavior of periodic lattices is complex as revealed with the help of modern investigation methods such as in situ-synchrotron radiation micro tomography [3]. The progressive failure of lattice structures includes nonlinear mechanical effects such as elastic and plastic post-buckling (features of structural mechanics), plasticity and material rupture (features of strut scale material mechanics). Such failure modes often appear *locally* in the lattice, but progressively lead to total failure of the lattice structure [4]. Tracing rigorously the structural behavior with buckling involves the incorporation of geometrical nonlinearity in the computational model. Buckling is dominated by the slenderness, the waviness and the loading condition of the struts. Plasticity is a material nonlinearity and according to [3], it is primarily manifested at strut junctions. Therefore, appropriate numerical models for the mechanical behavior of periodic lattices should incorporate such geometrical and material nonlinearity at the strut scale for a proper representation of the lattice response.

The deformation behavior of lattice structures can be classified into two categories: bending dominated and stretch dominated. In bending dominated lattices the unit cells deform via the bending moments at the strut junctions and plastic hinges form in case of a ductile material. In stretch dominated lattices tensile or compressive forces in the struts dictate and plastic yielding and buckling are dominant in the struts for ductile material.[5]

1.2. Mechanical modeling of periodic lattices

Numerical modeling can play a very useful role in this respect: advanced models with predictive capabilities yield significantly faster and cheaper design processes than those based on experimental tests of lattice prototypes. Moreover, simulations can give more insight into the deformation process, as they for instance enable an uncoupling of mechanical phenomena that are naturally correlated in reality. A reliable, fast yet accurate and widely-applicable computational methodology to simulate and predict the mechanical response of periodic lattice structures is clearly useful and can accelerate their design for different types of applications.

Finite Element Analysis has been applied intensively in simulating periodic lattices. In FE analyses, lattice struts are represented using either a mesh of solid finite elements [6–9] (e.g. tetrahedral elements) or a string of beam finite elements [10–13]. Compared to solid finite element, beam finite elements are less maneuverable in terms of geometry, but require a significantly lower computationally effort. However, direct FE analyses (or direct numerical simulation–DNS) using beam finite elements are still computationally prohibitively expensive because: (1) a large amount of beam finite elements is needed to discretize moderate size lattices (6 millions for a BCC lattice of $50 \times 50 \times 50$ unit cells); (2) the governing equations are substantially non-linear (i.e. Newton's method is required to iteratively solve the governing equations – for numerous time steps). As a result, only small lattices with a limited number of unit cells can in practice be considered.

Typically, using beam finite elements helps to reducing the computational cost, whereas employing solid finite elements allows for a more accurate description of the strut geometry. Geometric details include strut curvatures, the varying shapes

of the cross section along the strut, the powder adhesion on the strut surface and the actual geometry of the strut junction. Neglecting such geometrical details can in the same cases compromise the accuracy of the prediction of the simulation [14]. However, in the case of highly porous lattice structures containing high aspect ratio struts, the resulting 3D mesh of solid finite elements would yield simulations for other than a few unit cells prohibitively expensive [5].

This makes beam finite element a viable modeling option for problem sizes containing numerous unit cells. Timoshenko beams can be used when the diameter is larger than 10% of the length, i.e. when the shear effect in the strut can no longer be neglected [14], which is the modeling choice adopted in this work.

The difficulty of a beam based finite element model to capture the geometrical details can be addressed using a variety of techniques. Smith et al. [13] used several Timoshenko beam finite elements to represent each strut in BCC and BCCZ unit cells. The beam cross section close to the junction is enlarged in their study to mimic the presence of junctions, as performed in this work. They observed that the beam model and the solid element model were both sufficiently accurate to describe experimental results. Liu et al. [11] used a string of randomly aligned Timoshenko beams to model the non-straightness of the struts and successfully reproduced experimental lattice responses. In a different approach, Portela et al. [15] meshed realistic strut junctions using solid elements. The FE model of the junction was then bridged to Timoshenko beam elements that represent the struts.

It is thus apparent that, although not all forms of geometrical imperfections of the metallic printed lattices can be accounted for in a beam based representation, it is a computationally efficient choice for capturing experimentally observed lattice behaviors. In light of this, the presented work uses a string of Timoshenko beam elements to model each strut and its cross sectional variation as a result of the manufacturing process.

1.3. The quasicontinuum method

In order to simulate lattices for engineering applications, conventional FE analyses using beam finite elements cannot be applied. Instead, some type of model reduction is required.

There are two experimentally observed features that can be exploited for model reduction for metallic printed lattices. The first one is the periodic lattice pattern. Although the manufacturing process introduces random imperfections resulting lattices can generally still be considered as periodic on the global scale, before buckling and damage occurs. The second feature is the *locality* of the deformation of the lattice. In experiments, the failure of the lattice structure starts in small local zones (around the first failing strut). On the strut scale, local deformation modes such as buckling, plastic hinge formation, rupture (in case of brittle material) initially occur. These local deformation modes then propagate through the lattice and activate more global deformation modes such as the occurrence of shear bands. During these processes however, the remaining part of the lattice most often deform in relatively homogeneous manner.

The aforementioned *locality of the deformation* of critical lattice zones and the

periodicity of the lattice provide conditions for the quasicontinuum method – a multi-scale model reduction strategy – to be applied, because it features an appropriate division of periodic lattices into so-called fully-resolved domains (with a high resolution to capture localization) and coarse-grained domains (with simplified kinematics and a lower resolution in order to achieve computational savings). The quasicontinuum method is a concurrent multi-scale method that was initially proposed for simulating large scale atomic lattice systems at an affordable computational cost [16–19]. Particularly, the subsequent development of the virtual-power-based quasicontinuum method [20] enables accurate and efficient modeling of structural lattices with dissipative mechanisms and motivates the tailoring of this approach to the correct application incorporating struts with varying diameters and their elastoplastic behavior.

The quasicontinuum features two model reduction steps: *interpolation* and *summation*. During the interpolation step, all the kinematic variables of the lattice are preserved in the fully-resolved domains (FRDs), much like in a DNS, so as to be kinematically rich to describe localized deformation phenomena. In the coarse-grained domains (CGDs) however, the kinematic variables of the lattice are interpolated using finite element shape functions and a reduced set of kinematic variables that are defined at the representative lattice nodes. This yields large domains with simplified kinematics, to describe slowly fluctuating (linear and non-linear) deformations. The summation step constructs the governing equations of the system using a reduced set of interactions (e.g. trusses in a truss lattice, inter-atomic interactions in atomistic lattices): each interaction in the FRDs is accounted for, but a limited number of sampling interactions is used in the CGDs.

It needs to be emphasized that the quasicontinuum method is primarily applied to address periodic lattices although its application to irregular lattices was also reported in [21]. The requirement of periodicity for the unit cell is needed in the CGDs due to the *interpolation* and *summation* operations. Periodicity however does not limit the FRDs, e.g. a strut can deform in this domain in a way that the local periodicity of the lattice is no longer satisfied.

The conventional quasicontinuum method only allows for a single beam per strut [22]. The ability to describe buckling and the representation of geometrical variations along the strut axis however necessitate the use of multiple beam finite elements along a strut, being the first main identified gap in the literature and the first main contribution to the state of the art. Moreover, to trace the evolution of local deformation in a computationally efficient way, an accurate and robust adjustment of the FRDs and CGDs during a simulation, referred to as adaptive scheme, is also missing for the generalized quasicontinuum method developed in this thesis. The second and third main contributions of this work are the implementation of such adaptive scheme for elastic and elastoplastic lattice behaviors, respectively.

1.4. The multi-scale methods

Since the quasicontinuum method falls into the category of the multi-scale methods, it is worth mentioning the position of the quasicontinuum method within the family of the multi-scale methods.

Multi-scale methods are capable of bridging the material behavior and the structural geometries at small scales with the physical behaviors at higher scales. A variety of materials ranging from metals, ceramics, polymers (both synthetic and biological) are by essence multi-scale and thus necessitate multi-scale methods for analysis [23]. According to [24], multi-scale methods can be broadly categorized into two groups: (1) hierarchical (e.g. the FE^2 method); (2) concurrent methods (e.g. the quasicontinuum method). Hierarchical methods allow for bidirectional passage of information between fine and coarse scales. In FE^2 methods, the condition of scale separation is a prerequisite. The macroscopic deformation is passed onto the representative volume element (RVE) of the material micro-structure. An independent boundary value problem is defined and solved at the RVE scale. The average stress of the RVE is passed back to the macroscopic model. The solution of the boundary value problems at the quadrature points makes FE^2 methods computationally demanding. Moreover, the incorporation of local behaviors (e.g. cracks) in FE^2 methods requires additional complexities [25].

Concurrent methods employ the fine and coarse scales simultaneously and therefore entail a "handshake" procedure between different co-existing scales at the interface. No scale separation is needed, nor postulating macro-to-micro and micro-to-macro relations. Local behaviors/deformation can be more naturally accounted for as they simply need to be embraced at the fine scale.

The quasicontinuum method investigated in the presented work is a kind of concurrent multi-scale method. In particular, the interaction at the fine scale is modeled using beam finite elements. The response of beams are local (in contrast to the non-local inter-atom interaction in the quasicontinuum modeling of atomic lattices that leads to the spurious forces) so that the spurious forces across the FRD-CGD interfaces are less prevalent. Moreover, an innovative adaptive scheme is proposed for the quasicontinuum method so as to automatically deploy FRDs and CGDs whenever and wherever needed.

1.5. Objectives & Originalities

This thesis presents an adaptive (FRD/CGD automatic adjustment) generalized quasicontinuum method (incorporating multiple diameter struts) that can describe the nonlinear mechanical response of periodic lattices of arbitrary shaped unit cells with computational efficiency, allowing for the simulation of lattice volumes out of reach with DNS.

The simulations conducted using the method proposed in this work can serve to predict the loading bearing capacity of different unit cell designs such as the unit cell shape, strut connectivity and strut diameters, for large and geometrically complex macroscopic domains with relatively little computational costs. A possible application is the prediction of the mechanical behaviour of orthopedic implants [26]. The adaptive updating of FRDs and CGDs furthermore enable localized deformation to evolve through the entire domain, whilst the accuracy and computational savings remain high.

From a material engineer's perspective, the quantities of interest in the mechanical model that can investigated include, and are not limited to, the load bearing

capacity (i.e. the peak strength), the loading curve until damage occurs, which can be used to assess the energy absorption of the lattice, the location and the orientation of the potential shear bands, particularly for lattices under complex loading, the failure of the lattices caused by strut bending, and the occurrence of plastic hinges at strut junctions.

Even though strut rupture and the inter-strut contact in the stages of failure and densification are out of consideration in the proposed numerical model, it incorporates a set of ingredients to yield relevant results. Note that incorporating strut rupture and contact into the adaptive generalized quasicontinuum method is possible without modifying the framework, considering that these phenomena are generally limited to the FRDs and involve the micro model itself and not the QC methodology.

Although naturally present in the real world, random distributions of defects in the lattice are not considered in the proposed numerical model as they are considered to be out of scope. It is worth noting that since a string of beam elements is used to represent a single strut, it is possible to misalign the centroid axes of the beams to mimic strut waviness. However, the prerequisite of applying the quasicontinuum method is the periodicity of the unit cell in the CGDs. Therefore, unless the strut waviness is considered to be a periodic feature or if it merely appears in the FRDs, strut waviness cannot be easily accounted for in the proposed numerical model.

The developed tool accounts for

- geometrical variability along the strut;
- localized deformation/failure induced by the buckling and plastic bending of individual struts;
- automatic adaptation of the quasicontinuum model (FRD/CGD adjustment) following the evolution of lattice deformation during a simulation.

To this end, original computational developments are reported that are relevant contributions to the state of art, bridging the identified gaps in the literature. The main computational developments are summarized as follows:

- formulation and implementation of two types of 3D co-rotational elastoplastic beam finite elements;
- formulation and implementation of a generalized quasicontinuum method incorporating several beam finite elements with different diameters along a single strut;
- formulation and implementation of an adaptive scheme for the generalized quasicontinuum method, based on a novel and general refinement indicator for elastic and elastoplastic lattice behaviors.

The resulting computational tool is applied to relevant mechanical problems, and its accuracy and computational efficiency are assessed by comparing the framework's results and time requirements to those of the DNS. The performance of the

framework is furthermore demonstrated by simulating lattice volumes that are well beyond of the reach of DNS.

Similar efforts are carried out by Phlipot and Kochmann[27] using 3D co-rotational Euler-Bernoulli beam finite elements to model the struts of multi-lattices and employing a similar multi-field like interpolation and incorporating adaptivity. Therefore, it is useful to highlight the significant differences of this work:

(i) elastic Euler-Bernoulli beam FEs are used in [27] whereas elastoplastic Timoshenko beam FEs are adopted here;

(ii) [27] focuses on a multi-lattice (by adopting terminology from atomistics [28], unit cells with multiple unique nodes are referred to as multi-lattices), which is decomposed into several single Bravais lattices and an individual strut in the single lattice is represented using one beam FE, while a string of several beam FEs are used here to represent single struts to account for a more realistic strut geometry;

(iii) in [27], the sampling unit cells are placed at the nodes of the interpolation element and an additional Cauchy-Born rule based sampling unit cell is chosen at the barycenter of the interpolation elements, while, in the presented work, the sampling unit cells are selected at the Gauss quadrature points of the interpolation elements and each type of beam node family comes with its own interpolation function and separately stored kinematic variables are used for each beam node family;

(iv) the refinement indicator in [27] uses the second invariant criterion from atomistic lattice [19], while in this thesis a refinement indicator based on measuring the strain energy is proposed, together with an new adaptive scheme.

1.6. Outline

In Chapter 2, the generalization of the quasicontinuum method (GQC) is reported, incorporating a multi-field like interpolation scheme, which categorizes the beam nodes into different groups according to the beam properties and interpolate their kinematic variables group-wise. This enables multiple beam finite elements of different geometrical properties to represent a single strut with a spatially varying diameter. A 3D co-rotational beam finite element with embedded plastic hinges is developed in this chapter to capture the buckling and plastic bending of individual struts.

In Chapter 3, a novel and general refinement indicator and an adaptive scheme are proposed for the generalized quasicontinuum method for elastic lattice behavior. The refinement indicator is general in the sense that it is also applicable to the conventional quasicontinuum method. Based on the defined refinement indicator, an adaptive scheme is established for the GQC. The adaptive scheme triggers (1) the transformation of coarse-grained domain into fully-resolved domain and (2) the refinement of the interpolation in the coarse-grained domain – wherever the refinement indicator exceeds a user defined tolerance. A thorough study of the effect of the tolerance on the accuracy and efficiency of the generalized quasicontinuum modeling is conducted. Guidance on choosing appropriate threshold values for the parameters of the refinement indicator is also provided.

In Chapter 4, the adaptive scheme of Chapter 3 is extended to account for elastoplastic lattice behavior. The extension of the adaptive scheme is based on

restricting plasticity to the FRDs, being an additional criterion to the ones developed in Chapter 3. The upgraded adaptive GQC is successfully applied to model the scratch of an elastoplastic Kelvin lattice in an accurate and efficient manner.

Finally, conclusions are drawn in Chapter 5, complemented with some suggestions for future developments.

References

[1] M. Rashed, M. Ashraf, R. Mines, and P. Hazell, *Metallic microlattice materials: A current state of the art on manufacturing, mechanical properties and applications,* Materials & Design **95**, 518 (2016).

[2] C. Y. Yap, C. K. Chua, Z. L. Dong, Z. H. Liu, D. Q. Zhang, L. E. Loh, and S. L. Sing, *Review of selective laser melting: Materials and applications,* Applied Physics Reviews **2**, 041101 (2015), https://doi.org/10.1063/1.4935926 .

[3] H. D. Carlton, J. Lind, M. C. Messner, N. A. Volkoff-Shoemaker, H. S. Barnard, N. R. Barton, and M. Kumar, *Mapping local deformation behavior in single cell metal lattice structures,* Acta Materialia **129**, 239 (2017).

[4] R. Mines, *Some fundamental structural ideas for conventional metallic lattice structures,* in *Metallic Microlattice Structures: Manufacture, Materials and Application* (Springer International Publishing, Cham, 2019) pp. 7–15.

[5] B. Lozanovski, M. Leary, P. Tran, D. Shidid, M. Qian, P. Choong, and M. Brandt, *Computational modelling of strut defects in slm manufactured lattice structures,* Materials & Design **171**, 107671 (2019).

[6] P. Li, Z. Wang, N. Petrinic, and C. R. Siviour, *Deformation behaviour of stainless steel microlattice structures by selective laser melting,* Materials Science and Engineering: A **614**, 116 (2014).

[7] P. Li, *Constitutive and failure behaviour in selective laser melted stainless steel for microlattice structures,* Materials Science and Engineering: A **622**, 114 (2015).

[8] H. Cho, Y. Cho, and H. N. Han, *Finite element analysis for mechanical response of Ti foams with regular structure obtained by selective laser melting,* Acta Materialia **97**, 199 (2015).

[9] M. R. Karamooz-Ravari and M. Kadkhodaei, *A computationally efficient modeling approach for predicting mechanical behavior of cellular lattice structures,* Journal of Materials Engineering and Performance **24**, 245 (2015).

[10] M. R. Karamooz-Ravari and M. Kadkhodaei, *Finite element modeling of the elastic modulus of T-6Al-4V scaffold fabricated by SLM,* in *Fifth Biot Conference on Poromechanics*, edited by C. Hellmich, B. Pichler, and D. Adam, Technische Universitat Wein (American Society of Civil Engineers, Reston, Virginia, U.S., 1993) pp. 1021–1028, https://ascelibrary.org/doi/pdf/10.1061/9780784412992.122 .

[11] L. Liu, P. Kamm, F. García-Moreno, J. Banhart, and D. Pasini, *Elastic and failure response of imperfect three-dimensional metallic lattices: the role of geometric defects induced by selective laser melting,* Journal of the Mechanics and Physics of Solids **107**, 160 (2017).

[12] G. Campoli, M. S. Borleffs, S. A. Yavari, R. Wauthle, H. Weinans, and A. A. Zadpoor, *Mechanical properties of open-cell metallic biomaterials manufactured using additive manufacturing,* Materials & Design **49**, 957 (2013).

[13] M. Smith, Z. Guan, and W. J. Cantwell, *Finite element modelling of the compressive response of lattice structures manufactured using the selective laser melting technique,* International Journal of Mechanical Sciences **67**, 28 (2013).

[14] R. Gümrük and R. A. W. Mines, *Compressive behaviour of stainless steel micro-lattice structures,* International Journal of Mechanical Sciences **68**, 125 (2013).

[15] C. M. Portela, J. R. Greer, and D. M. Kochmann, *Impact of node geometry on the effective stiffness of non-slender three-dimensional truss lattice architectures,* Extreme Mechanics Letters **22**, 138 (2018).

[16] E. B. Tadmor, R. Phillips, and M. Ortiz, *Mixed atomistic and continuum models of deformation in solids,* Langmuir **12**, 4529 (1996), https://doi.org/10.1021/la9508912 .

[17] E. B. Tadmor, M. Ortiz, and R. Phillips, *Quasicontinuum analysis of defects in solids,* Philosophical Magazine A **73**, 1529 (1996), https://doi.org/10.1080/01418619608243000 .

[18] R. Miller, M. Ortiz, R. Phillips, V. Shenoy, and E. B. Tadmor, *Quasicontinuum models of fracture and plasticity,* Engineering Fracture Mechanics **61**, 427 (1998).

[19] J. Knap and M. Ortiz, *An analysis of the quasicontinuum method,* Journal of the Mechanics and Physics of Solids **49**, 1899 (2001), the JW Hutchinson and JR Rice 60th Anniversary Issue.

[20] L. A. A. Beex, R. H. J. Peerlings, K. van Os, and M. G. D. Geers, *The mechanical reliability of an electronic textile investigated using the virtual-power-based quasicontinuum method,* Mechanics of Materials **80**, 52 (2015).

[21] K. Mikeš and M. Jirásek, *Quasicontinuum method extended to irregular lattices,* Computers & Structures **192**, 50 (2017).

[22] L. A. A. Beex, P. Kerfriden, T. Rabczuk, and S. P. A. Bordas, *Quasicontinuum-based multiscale approaches for plate-like beam lattices experiencing in-plane and out-of-plane deformation,* Computer Methods in Applied Mechanics and Engineering **279**, 348 (2014).

[23] M. F. Horstemeyer, *Multiscale Modeling: A Review,* in *Practical Aspects of Computational Chemistry* (2010) p. 87.

[24] P. R. Budarapu, X. Zhuang, T. Rabczuk, and S. P. Bordas, *Chapter one - multiscale modeling of material failure: Theory and computational methods,* in *Advances in Crystals and Elastic Metamaterials, Part 2*, Advances in Applied Mechanics, Vol. 52, edited by M. I. Hussein (Elsevier, 2019) pp. 1 – 103.

[25] A. van den Eijnden, P. Bésuelle, R. Chambon, and F. Collin, *A fe2 modelling approach to hydromechanical coupling in cracking-induced localization problems,* International Journal of Solids and Structures **97-98**, 475 (2016).

[26] X.-Y. Zhang, G. Fang, and J. Zhou, *Additively manufactured scaffolds for bone tissue engineering and the prediction of their mechanical behavior: A review,* Materials **10** (2017), 10.3390/ma10010050.

[27] G. P. Phlipot and D. M. Kochmann, *A quasicontinuum theory for the nonlinear mechanical response of general periodic truss lattices,* Journal of the Mechanics and Physics of Solids **124**, 758 (2019).

[28] M. Dobson, R. S. Elliott, M. Luskin, and E. B. Tadmor, *A multilattice quasicontinuum for phase transforming materials: Cascading cauchy born kinematics,* Journal of Computer-Aided Materials Design **14**, 219 (2007).

2

Generalized quasicontinuum modeling of metallic lattices with geometrical and material nonlinearity and variability*

In this chapter, a generalized quasicontinuum method is proposed to model the mechanical response of 3D lattice structures. The method relies on the spatial coupling of fully-resolved domains and coarse-grained domains. In the fully-resolved domain, the full micro-structure is taken into account. In the coarse-grained domain, the kinematics of the micro-structure are individually interpolated based on their connectivity. On top of that, the contributions of the micro-structure to the governing equations in the coarse-grained domain are sampled using only a few unit cells. In both domains, geometrical and material variability along the strut can be naturally taken into account using a 3D co-rotational beam finite element with embedded plastic hinges. The approach is applied for BCC lattices, demonstrating that the new method can capture both material and geometrical non-linearities of single struts at a fraction of the cost of a direct numerical simulation.

* Parts of this chapter have been published in Computer Methods in Applied Mechanics and Engineering **366**, 112878 (2020) [1].

2.1. Introduction

Additive manufacturing enables the fabrication of metallic lattice structures layer by layer. Metallic lattice structures consist of repeating geometrically similar units, known as unit cells, and are of interest thanks to their high strength-to-weight ratio. A unit cell is composed of struts that are connected through a prescribed pattern. Fig. 2.1 illustrates a Body Centered Cubic (BCC) metallic lattice. The BCC unit cell consists of 8 struts with varying cross sections. Unit cells can be adjusted and optimized to desired mechanical responses.

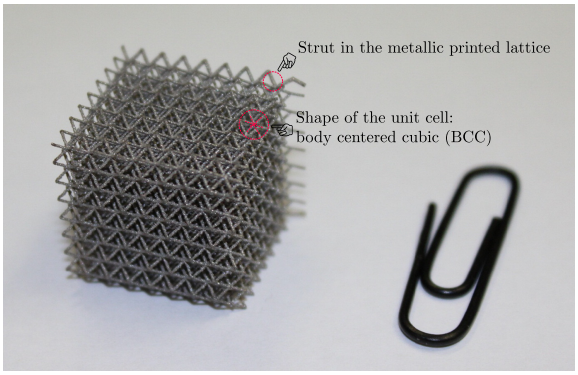

(a) Size comparison between a metallic BCC lattice and a paper clip. Reprinted from [2] with permission from Elsevier.

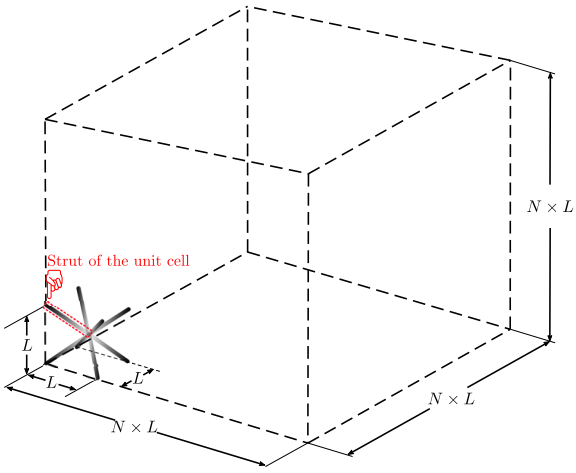

(b) Definition of a BCC lattice, L is the size of the BCC unit cell and N denotes the number of unit cells along one spatial dimension.

Figure 2.1: Illustration of a BCC metallic lattice.

The main failure modes of metallic lattice structures include the buckling and

the plastic bending of individual struts [3, 4]. Both failure modes can be observed in the tomographic reconstructions of Fig. 2.2 and clearly occur within a strut. Therefore, the failure of metallic lattice structures can largely be attributed to localized geometrically and materially non-linear behavior of individual struts.

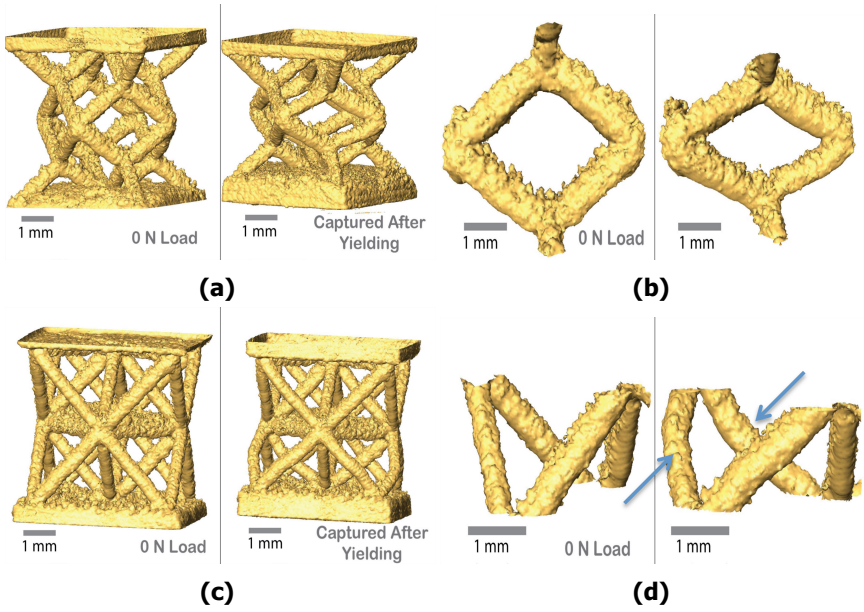

Figure 2.2: 3D images of deformed lattice structures. The 3D tomographic images show a Rhombic Dodecahedron (RD) and an Octet Truss (OT) before (left) and after deformation (right). Images in (2.2a, 2.2c) show the crushing or yielding behavior of the RD structure, and images in (2.2b, 2.2d) show the buckling observed in OT structures with low relative densities (10%). Reprinted from [4] with permission from Elsevier.

Predicting the mechanical behavior with simulation software avoids the manufacturing and experimental testing of physical prototypes. If mechanical simulations of virtual prototypes are to replace the experimental testing of physical prototypes, time and money are saved. On top of that, simulation results reveal more detailed information. Computational approaches to simulate the mechanical behavior of metallic lattice structures have therefore been addressed in several studies.

Noor [5, 6] homogenized the beam-like lattice structure to obtain an effective material model. The continuum-based analogy may however be considered to contradict the inherent discrete nature of metallic lattice structures. This entails amongst others that predicting localized deformation/failure in the continuum model is challenging. Ushijima [7] and Gümrük [8] instead focused on a single unit cell. Using beam theory and the plastic bending moment of beams with circular cross section with a bi-linear elastoplastic material, they derived closed-form expressions to predict the initial stiffness and the plastic collapse strength of a BCC

lattice structure. Nevertheless, the approach must be suitably adapted to each new type of unit cell to be studied. Moreover, localization cannot be considered. Other approaches discretized each strut with many 3D finite elements [9–12], but come with the obvious disadvantage that not more than a few unit cells can be modeled due to the significant computational costs. An advantage is that they are able to include small-scale strut and lattice imperfections. Consequently, localized deformation/failure can be captured, but at a high, often prohibitive computational cost. As a compromise, FE discretizations using beam elements [13–16] were proposed. Each strut is then modeled using one or more beam elements in which imperfections can be incorporated to some extent. This can be achieved by misaligning the axes of the beam elements (to mimic strut waviness), and by varying the cross sectional radius (to mimic strut thickness variation) [14].

Leveraging the periodic characteristics of lattice structures, Beex and co-workers [17–20], Kochmann and Amelang [21], and Phlipot and Kochmann [22] used the quasicontinuum method [23–26] to establish multi-scale models of lattice structures. In the quasicontinuum method [17–22], each strut in the unit cell of the lattice is simulated using one truss/beam element. The lattice is then divided into a so-called fully-resolved domain and a coarse-grained domain. In the fully-resolved domain, all kinematic variables of the truss/beam elements are represented. In the coarse-grained domain, the kinematic variables are interpolated to reduce the number of degrees of freedom. On top of that, only a few truss/beam elements are sampled in the coarse-grained domain so that less computational efforts are required to construct the governing equations. The concurrent character of the quasicontinuum method, i.e. the use of fully-resolved and coarse-grained domains, allows localized deformation and failure of lattices to be relatively accurately described.

If the quasicontinuum method in its current state is to be applied to metallic printed lattices, each strut must be represented with a single beam element. Besides the fact that complex strut deformations such as buckling cannot accurately be described with a single beam element, essential strut characteristics such as a spatially varying cross sectional radius cannot be accounted for.

To alleviate these limitations, we propose an essential enhancement of the quasicontinuum method such that several beam elements per strut can be incorporated, where the geometrical and material properties of each beam element can vary. We achieve this by assigning beam nodes to specific families and interpolating the kinematic variables of these families independently of each other in coarse-grained domains. The coarse-grained domains are kinematically coupled to regions in which the beam model is fully resolved. As the coarse-grained domain is substantially complexified compared to conventional quasicontinuum approaches, we also study which unit cells in the coarse-grained domain need to be sampled to approximate the governing equations accurately, yet efficiently.

It can be noted that the generalized quasicontinuum that we propose here, only allows large deformation fluctuations (e.g. caused by fracture) in the fully resolved region. From that perspective, the method is not different from the conventional quasicontinuum method, or most other nested multi-scale methods for that matter.

The remainder of this contribution is organized as follows. Section 2.2 introduces the concepts of the generalized quasicontinuum method. Section 2.3 explains the 3D co-rotational beam element with embedded plastic hinges. Section 2.4 presents a performance study while Section 2.5 summarizes the conclusions of this work.

2.2. Generalized quasicontinuum method

Metallic lattice structures can be deemed multi-scale. One can then distinguish the meso-scale as the scale of a single unit cell (or a few) and the micro-scale as the scale of a single constituent of a unit cell (a strut, a beam, a spring, etc.). The macro-scale refers to the whole lattice structure, which is built up by repeating the unit cell in the three spatial directions (see Fig. 2.1b). This section presents a novel multi-scale method that is applicable to such periodic metallic lattice structures.

Multi-scale approaches can be classified in many ways. One way is to group them in nested and non-nested approaches. In non-nested approaches, macroscopic deformations (deformation paths in case of dissipation) are applied to a unit cell and the macroscopic stress–deformation responses are measured. A constitutive description is then fitted to the measured response which is used for a computation at the macro-scale (in which the unit cell is homogenized). In nested computations, the macroscopic deformation at each quadrature point is applied to a unit cell and the homogenized stress (and its derivative) is extracted and sent back to the macro-scale computation. Nested approaches thus consider the microstructural model at each quadrature point, which makes them more computationally expensive compared to non-nested approaches. On the other hand, nested approaches make no assumptions about the homogenized constitutive model.

Nested and non-nested approaches can each be subdivided into concurrent and non-concurrent schemes. In concurrent schemes, the micro-structure is fully resolved in small regions in which high deformation fluctuations occur. In the remainder of the domain, the homogenization approach (nested or non-nested) ensures that the computational efficiency remains acceptable. Non-concurrent schemes do not use a domain in which the micro-structure is fully resolved.

The approach here is a nested, concurrent approach. It coarse-grains the microstructure in the largest part of the domain and fully resolves it in small regions of interest. Computational homogenization is however not applied in the coarse-grained domain, since no scale-separation is present. This makes the method more straightforward to apply (the ratio between the size of the macro-scale elements and the size of the unit cell is not important) and to implement for high-order macro-scale elements (the method is as easy to implement for linear interpolation elements as for cubic interpolation elements at the macro-scale for instance). The disadvantage is that the computational costs are larger than for computational homogenization approaches.

The proposed method is termed as the *generalized* quasicontinuum (QC) method. As indicated by the name, it is the result of a generalization of the quasicontinuum method. The quasicontinuum method was originally developed by Tadmor et al. [23, 24] as a mixed continuum and atomistic approach for the simulation of polycrystalline materials. It was extensively used and improved by Luskin and Ortner

[27–29] for the simulation of crystal defects. They also performed a comprehensive study on the accuracy and stability of the quasicontinuum method [30]. The quasicontinuum method was later extended to model discrete structural lattices after being reformulated to deal with dissipative spring models [31] and variational approaches [32]. Applications include 2D truss/beam lattices [17–19, 33, 34] and 3D truss lattices [21, 22]. The generalized quasicontinuum method inherits the two model reduction steps of the quasicontinuum method, i.e. 'interpolation' and 'summation'.

For illustration, the generalized quasicontinuum method is applied to a demonstrative 1D truss lattice in Fig. 2.3. The truss lattice consists of 29 unit cells, each consisting of two interconnecting truss finite elements (— and —) and a defect unit cell ($a_{18} - a_{19}$) comprised of a single truss finite element(—). Each unit cell thus contains three nodes (two • and one •. Since these nodes are present inside a unit cell on the micro-scale, we refer to them as micro-structural nodes. The defect unit cell will provoke strain localization because different properties are assigned to the three types of trusses, with truss (—) being the most compliant (Table 2.1). The 1D truss lattice is fixed at the left end and a tensile force with a magnitude of 0.1 N is exerted at its right end. The values in Table 2.1 are of no physical significance here and are only used for numerical demonstration purposes.

Truss color	green	magenta	red
Length (mm)	0.6	0.4	1
Cross section area (mm^2)	0.1	0.1	0.05
Young's modulus (N/mm^2)	10	20	10

Table 2.1: The geometrical dimensions and material properties of the three types of trusses.

This model is referred to as the 'direct model'. The solution of this direct model can be obtained by minimizing the total potential energy, e.g. by using Newton's method. Let $\mathbf{u}$ and $\mathbf{f}_{\text{ext}}$ denote the column vectors of the displacements and of the external forces of all micro-structural nodes and m be the total number of trusses. The total potential energy includes the work of the externally applied forces and the potential energy of each truss, i.e. $\mathbf{E}_i(\mathbf{u})$:

$$\mathbf{u}^* = \underset{\mathbf{u}}{\operatorname{argmin}} \left(-\mathbf{f}_{\text{ext}}^T \mathbf{u} + \sum_{i=1}^{m} \mathbf{E}_i(\mathbf{u}) \right). \tag{2.1}$$

Solving the direct model including all trusses is referred to as the direct numerical simulation (DNS). The displacement profile obtained by solving Eq. (2.1) is shown in Fig. 2.4. The strain localization appears in the defect truss as expected.

The computational cost for the direct numerical simulation of this demonstrative 1D truss lattice is no issue. However, we should bear in mind two fundamental characteristics of the direct numerical simulation. First, the kinematic variables of all the micro-structural nodes are present in the governing equations. Second, in

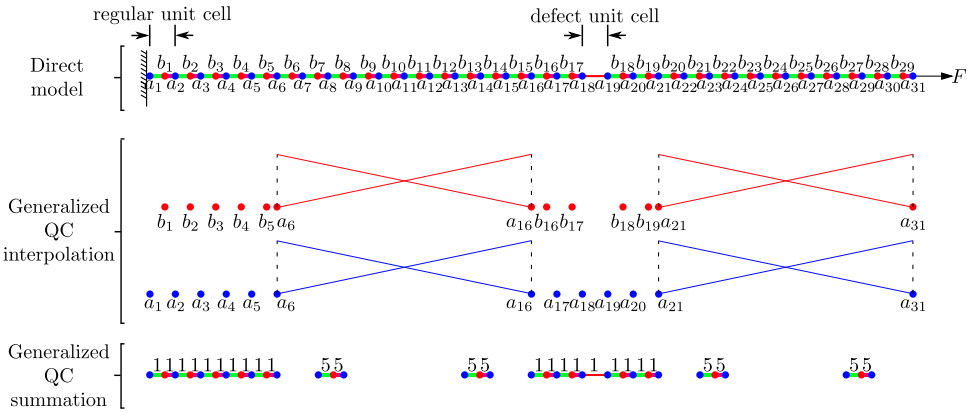

Figure 2.3: The generalized quasicontinuum (QC) modeling of a 1D truss lattice. `Direct model`: The 1D truss lattice consisting of 29 normal unit cells (•—•—•) and a defect unit cell (•—•) and 60 nodes. The nodes are linked by three types of trusses, i.e. the green truss (▬), the magenta truss (▬) and the red truss (—). The nodes are classified into two types, i.e. • and •. Each blue node is connected to a green truss on its RHS and a magenta truss on its LHS. Each red node is connected to a magenta truss on its RHS and a green truss on its LHS. `Generalized QC interpolation`: Intervals $[a_1, a_6]$ and $[a_{16}, a_{21}]$ are considered as the fully-resolved domains (FRDs), intervals $[a_6, a_{16}]$ and $[a_{21}, a_{31}]$ are considered as the coarse-grained domains (CGDs). In each CGD, there is one linear macro-scale interpolation element. The DoFs of the blue and red nodes after the interpolation are shown. At each macro-scale interpolation node, i.e. a_6, a_{16}, a_{21}, a_{31}, two representative DoFs are stored, each used to interpolate the corresponding nodes. `Generalized QC summation`: The trusses that are sampled to construct the governing equations are shown with their weights.

the construction of the governing equations, all the trusses need to be sampled to compute their contributions to the governing equations. Since DNS of 3D lattices for macro-scale (i.e. engineering scale) applications can require billions of degrees of freedom (DoFs) and trusses, they are computationally prohibitive, especially for highly nonlinear analyses.

This is the main motivation of the generalized quasicontinuum method that alleviates the computational demand of the DNS. We discuss the generalized quasicontinuum method in the next two subsections.

2.2.1. Interpolation

This section elaborates on the first model reduction step, the interpolation of the kinematic variables of the direct model. This step aims at reducing the number of DoFs of the DNS in Eq. (2.1).

To implement 'interpolation', the direct model is divided into two kinds of nonoverlapping sub-domains: they are fully-resolved domains (FRDs) and coarse-grained

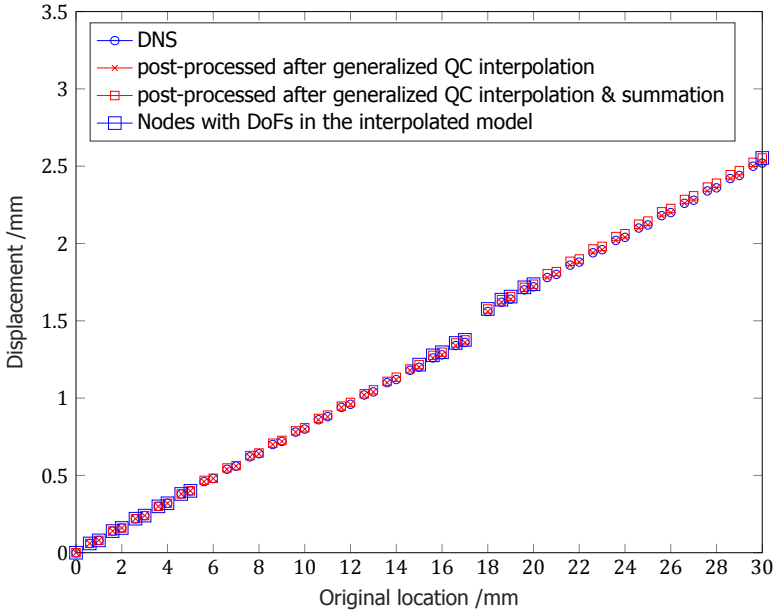

Figure 2.4: The displacement profiles of the micro-structural nodes in the 1D truss lattice obtained by the (1) DNS, (2) generalized QC interpolation, (3) generalized QC interpolation & summation. Because only a subset of micro-structural nodes possess DoFs (i.e. nodal displacement) in the interpolated model, post-processing is performed to show the nodal displacements of all micro-structural nodes.

domains (CGDs). Fig. 2.3 illustrates this for the aforementioned 1D example.

In the FRD, the kinematic variables of each micro-structural node are preserved as DoFs. Therefore, localised lattice behaviour such as the failure of a single strut can be incorporated. The FRD $[a_{16}, a_{21}]$ in Fig. 2.3 is used to capture the lattice behavior around the defect unit cell.

In the CGD, the kinematic variables of the micro-structural nodes are interpolated by the overlapping macro-scale interpolation elements. In the 1D truss lattice example in Fig. 2.3, each CGD is allocated one macro-scale linear interpolation element.

A macro-scale interpolation element uses finite element shape functions to interpolate the kinematic variables of the micro-structural nodes, using the representative kinematic variables stored at the finite element nodes appearing in the macro-scale interpolation mesh. The micro-structural nodes enveloped by the macro-scale interpolation elements are of different types. The kinematic variables of each type of micro-structural node are individually interpolated by corresponding representative kinematic variables of the macro-scale interpolation elements. In Fig. 2.3, the linear macro-scale interpolation element in domain $[a_6, a_{16}]$ has two macro-scale interpolation nodes, i.e. a_6 and a_{16}, each bearing two representative kinematic

variables: one for red and one for blue micro-structural nodes.

The reduced model after implementing interpolation is referred to as the "interpolated model".

Let $\mathbf{u}$ denote the column vector of the kinematic variables of all of the micro-structural nodes. Let $\mathbf{u}_\mathrm{r}$ denote the column vector which stores the reduced kinematic variables, i.e. the DoFs of the interpolated model, after the interpolation. The reduced kinematic variables can be related to the conventional kinematic variables by interpolation matrix $\mathbf{N}$ through

$$\mathbf{u} = \mathbf{N}\,\mathbf{u}_\mathrm{r}. \tag{2.2}$$

The minimization problem for the interpolated system now reads:

$$\mathbf{u}_\mathrm{r}^* = \underset{\mathbf{u}_\mathrm{r}}{\operatorname{argmin}} \left(-\mathbf{f}_\mathrm{ext}^T \mathbf{N}\,\mathbf{u}_\mathrm{r} + \sum_{i=1}^{m} \mathbf{E}_i(\mathbf{N}\,\mathbf{u}_\mathrm{r}) \right). \tag{2.3}$$

For the 1D truss lattice example, the 60 kinematic variables of the direct model are reduced to 26 in the interpolated model. Interpolation reduces the computational demand by decreasing the number of DoFs in the governing equations.

The generalized quasicontinuum method is a concurrent multi-scale method, because the kinematic variables at the micro-scale (i.e. the kinematic variables of the micro-structural nodes in the fully-resolved domain) and the kinematic variables at the macro-scale (i.e. the representative kinematic variables of the macro-scale interpolation nodes) co-exist in the governing equations. The fine and coarse scales are solved concurrently, as in [35, 36].

Care is required when imposing the boundary conditions (BCs) of the direct model onto the interpolated model. If the BCs are applied at the macro-scale interpolation nodes, the correct representative kinematic variables must be selected. The same care is required when applying external loads.

The displacement profile obtained by solving Eq. (2.3) exactly matches that of the DNS (Fig. 2.4).

2.2.2. Summation

The interpolated model has far fewer DoFs than the direct model and the amount of reduction increases with the spatial dimensions, being most beneficial in 3D. However, to solve the minimization problem of Eq. (2.3), all the trusses need to be sampled. It is worth noting that fro m now on, when a truss is said to be 'sampled', it means it is selected to construct the total potential energy of the system. In other words, sampled trusses/beams contribute to the governing equations (i.e. the internal forces and tangent stiffnesses), whereas non-sampled trusses/beams do not (and are instead represented by sampled ones). The approach proposed here consists of selecting a limited number of representative trusses and corresponding weights to represent the contributions of all the other trusses in the CGDs. This model reduction step is referred to as 'summation' and is akin to hyper-reduction in model order reduction [35–38]. In [37], a particular general approach to this

discrete optimization problem is proposed which also allows directly identifying the non-linear zone within the domain whilst optimizing the selection of hyper-reduced integration points.

Let $\mathbf{S}$ be the set of the trusses that are sampled to approximate the governing equations. Let ω_i b the number of trusses that truss i represents. After summation, the minimization problem in Eq. (2.4) becomes:

$$\mathbf{u}_\mathrm{r}^* = \underset{\mathbf{u}_\mathrm{r}}{\operatorname{argmin}} \left(-\mathbf{f}_\mathrm{ext}^T \mathbf{N}\, \mathbf{u}_\mathrm{r} + \sum_{i \in \mathbf{S}} \omega_i \mathbf{E}_i(\mathbf{N}\, \mathbf{u}_\mathrm{r}) \right). \tag{2.4}$$

The main question is how to select the sampling trusses and how to determine their weights ω_i. In the fully-resolved domain, each truss is selected as a sampling truss. Their corresponding weights are set to one because they only represent themselves (Fig. 2.3).

In the coarse-grained domain, different approaches to select the sampling trusses were formulated [17, 19, 33, 36, 39]. Specifically, [33] is based on an in-depth understanding of how the linear interpolation influences the potential energy of the interpolated lattice. [17, 19] consider the non-trivial effect of higher order interpolation on the potential energy of the interpolated lattice and propose to select the trusses which are positioned at the Gauss quadrature points as the sampling trusses.

Although a linear interpolation is used in the 1D truss example, the macro-scale interpolation nodes store the kinematic variables of several types of micro-structural nodes, which is similar to higher order interpolation in terms of the number of kinematic variables per element. Therefore, the sampling trusses are selected in a manner that is analogous to the manner proposed in [17] and [19] which investigated the preferential summation rule for quasicontinuum methods with higher order interpolation schemes. [17] and [19] proposed to select the trusses that are closest to the Gauss quadrature points as the sampling trusses for quasicontinuum methods with higher order interpolation schemes. Specifically, a sufficient number of Gauss quadrature points (GQPs) are determined for a macro-scale interpolation element. Here, a sufficient number of Gauss quadrature points means an appropriate number that can guarantee the convergence of the simulation while minimizing the number of sampling trusses in a macro-scale interpolation element. For higher order interpolation schemes and its analogies (e.g. the multi-field like interpolation scheme that is proposed in our method), too few Gauss quadrature points results in insufficient number of sampling trusses and thus diverges the simulation. However, if too many Gauss quadrature points are used, the computational efficiency is compromised due to the unnecessarily large number of sampling trusses. Then a unit cell centered at the position of each Gauss quadrature point of this macro-scale interpolation element is assumed. The trusses inside this unit cell are selected as the sampling trusses of this macro-scale interpolation element.

Let V_e and V_UC be the volume of the macro-scale interpolation element and of the unit cell, respectively, and W_GQP the normalized Gauss quadrature weight [40].

The weights of all of the sampling trusses in this unit cell equate

$$\omega_i = \mathrm{W}_{\mathrm{GQP}} \cdot \frac{V_{\mathrm{e}}}{V_{\mathrm{UC}}}, \qquad \text{with} \sum \mathrm{W}_{\mathrm{GQP}} = 1. \tag{2.5}$$

In Eq. (2.5), $V_{\mathrm{e}}/V_{\mathrm{UC}}$ gives the nominal number of unit cells that are present in the macro-scale interpolation element. Eq. (2.5) guarantees that each unit cell in the macro-scale interpolation element is represented by sampling unit cells.

For the 1D truss lattice example in Fig. 2.3, two Gauss quadrature points are used for each macro-scale interpolation element. The positions and the normalized weights of the two Gauss quadrature points are ($\xi_1 = -\frac{1}{\sqrt{3}}$, $\mathrm{W}_{\mathrm{GQP}_1} = 0.5$) and ($\xi_2 = \frac{1}{\sqrt{3}}$, $\mathrm{W}_{\mathrm{GQP}_2} = 0.5$) respectively in the 1D parent coordinate system $\xi \in [-1, 1]$. The sum of the normalized weights of GQPs equals 1 in Eq. (2.5). This ensures that the sum of weights of the sampling unit cells in a macro-scale interpolation element equals the nominal number of unit cells within the macro-scale interpolation element. In 2D and 3D settings however, an error is introduced at each FRD-CGD interface that is not aligned with the unit cell stacking.

The length of each macro-scale interpolation element is 10 mm and the length of a unit cell is 1 mm. According to Eq. (2.5), the weight of each sampling truss in the macro-scale interpolation element is 5. The direct model and the interpolated model require all 59 trusses of the truss lattice example to be considered. In the generalized quasicontinuum model (the interpolated and summed model) however, only 27 trusses need to be sampled in Fig. 2.3.

The displacement profile obtained by solving Eq. (2.4) is shown in Fig. 2.4 with a maximum relative error of 1.81% with respect to that of the DNS. The generalized quasicontinuum method results in a decrease of 56.7% ($60 \rightarrow 26$) in the number of DoFs and in 54.2% ($59 \rightarrow 27$) fewer sampling trusses.

Summation is thus a key step for nonlinear models to increase the computational efficiency, without which interpolation is relatively ineffective. In fact, it was shown that interpolation (model reduction) without summation (hyper reduction) may lead to an increase in the overall computational expense [39] due to the worsening of the stiffness matrix' condition number.

Thanks to the proposed generalized quasicontinuum method, we are able to use multiple beam elements with different geometrical and material parameters to model a single strut in the metallic printed lattices (one can imagine each unit cell in the 1D truss lattice of Fig. 2.3 consists of a single strut that is represented using three different beam elements). This is achieved by assigning beam nodes to specific families and interpolating the kinematic variables of these families independently of each other in coarse-grained domains. It amounts to a significant improvement compared to the conventional quasicontinuum method. The conventional quasicontinuum method does not have such a multi-field like interpolation mechanism and as a result, each strut can only be represented using one beam element. Consequently, the inherent material and geometrical variation along a single strut in the metallic printed lattices cannot be captured using the conventional quasicontinuum method. Therefore, the applicability of the proposed method is larger than that of existing quasicontinuum implementations.

2.3. 3D co-rotational beam element with embedded plastic hinges

In this work, the struts of the metallic lattice structure are modeled using a string of beam finite elements. To reproduce the basic failure modes of the metallic lattice structure, i.e. the buckling and the plastic bending of individual struts, 3D co-rotational beam finite elements (FEs) with embedded plastic hinges are developed and implemented based on [41, 42].

The co-rotational framework uses the formulation proposed by Rankin and Omid [43, 44] and further developed by Battini and Pacoste [41, 45] to treat structural instabilities and by Bui and Bordas [46, 47] for real time simulation of soft tissues. The plastic hinge model proposed by Powell and Chen [42, 48] was adopted here within the co-rotational framework to allow for capturing material nonlinearity of the metallic lattice. This combination is unprecedented to the authors' best knowledge, and it highlights one of the novelties of this paper.

2.3.1. Co-rotational framework for 3D beam element

This section presents how the overall motion of the beam finite element is decoupled into the rigid body movement and the deformation using a co-rotational approach. The kinematic variables and the coordinate frames in the co-rotational formulation are shown in Fig. 2.5. The global coordinate frame is defined by orthogonal basis $[\mathbf{e}_1, \mathbf{e}_2, \mathbf{e}_3]$ and origin O. In the undeformed configuration, the initial orientation of the straight beam element is $[\mathbf{e}_1^0, \mathbf{e}_2^0, \mathbf{e}_3^0]$. In the deformed configuration, the orientations of the two beam extremities become $[\mathbf{t}_1^1, \mathbf{t}_2^1, \mathbf{t}_3^1]$ and $[\mathbf{t}_1^2, \mathbf{t}_2^2, \mathbf{t}_3^2]$ respectively. Rotation matrix $\mathbf{R}_0$ denotes the 3D finite rotation from $[\mathbf{e}_1, \mathbf{e}_2, \mathbf{e}_3]$ to $[\mathbf{e}_1^0, \mathbf{e}_2^0, \mathbf{e}_3^0]$ and orientates the reference beam configuration with respect to the global basis.

The kinematic variables describing the deformed beam configuration consist of: (1) the displacements of the beam extremities relative to the reference beam configuration, i.e. $\mathbf{u}_1^g$ and $\mathbf{u}_2^g$; (2) the rotation matrices at the beam extremities, i.e. $\mathbf{R}_1^g$ and $\mathbf{R}_2^g$. $\mathbf{R}_1^g$ denotes the 3D finite rotation from $[\mathbf{e}_1^0, \mathbf{e}_2^0, \mathbf{e}_3^0]$ to $[\mathbf{t}_1^1, \mathbf{t}_2^1, \mathbf{t}_3^1]$. $\mathbf{R}_2^g$ denotes the 3D finite rotation from $[\mathbf{e}_1^0, \mathbf{e}_2^0, \mathbf{e}_3^0]$ to $[\mathbf{t}_1^2, \mathbf{t}_2^2, \mathbf{t}_3^2]$.

The key idea of the co-rotational formulation is to introduce a properly defined 'local coordinate frame' defined by orthogonal basis $[\mathbf{r}_1, \mathbf{r}_2, \mathbf{r}_3]$. Its origin is positioned at one extremity of the beam.

The basis vector $\mathbf{r}_1$ aligns with the central axis of the beam element. Therefore, it can be expressed as:

$$\mathbf{r}_1 = \frac{\mathbf{x}_2^g + \mathbf{u}_2^g - \mathbf{x}_1^g - \mathbf{u}_1^g}{\|\mathbf{x}_2^g + \mathbf{u}_2^g - \mathbf{x}_1^g - \mathbf{u}_1^g\|} \tag{2.6}$$

where $\mathbf{x}_i^g, i = 1, 2$ denotes the coordinates of the beam extremities in the undeformed configuration. The basis vectors $\mathbf{r}_2$ and $\mathbf{r}_3$ are defined as:

$$\mathbf{r}_3 = \frac{\mathbf{r}_1 \times \frac{\mathbf{t}_2^1 + \mathbf{t}_2^2}{2}}{\| \mathbf{r}_1 \times \frac{\mathbf{t}_2^1 + \mathbf{t}_2^2}{2} \|}, \qquad \mathbf{r}_2 = \mathbf{r}_3 \times \mathbf{r}_1. \tag{2.7}$$

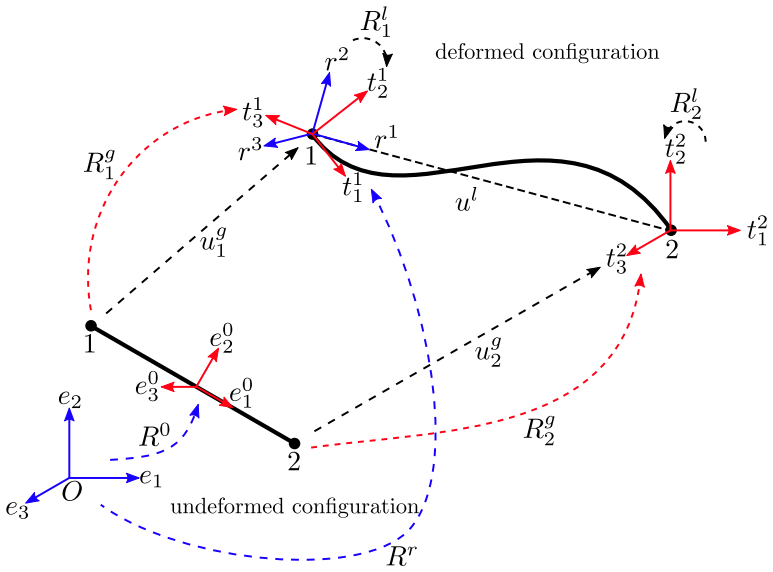

Figure 2.5: Coordinate frames and kinematic variables in the co-rotational formulation for a 3D beam element.

The 'local coordinate frame' is attached to the beam FE and therefore decouples the pure deformation of the beam from the rigid body movement.

The kinematic variables describing the rigid body movement are (1) the displacement of the origin of the 'local coordinate frame', i.e. $\mathbf{u}_1^g$; (2) The rotation matrix $\mathbf{R}_\mathrm{r}$ that denotes the 3D finite rotation from $[\mathbf{e}_1, \mathbf{e}_2, \mathbf{e}_3]$ to $[\mathbf{r}_1, \mathbf{r}_2, \mathbf{r}_3]$. The kinematic variables describing the deformation of the beam are (1) nominal beam elongation u^l, which is defined as:

$$\mathrm{u}^l = \|\mathbf{x}_2^g + \mathbf{u}_2^g - \mathbf{x}_1^g - \mathbf{u}_1^g\| - \|\mathbf{x}_2^g - \mathbf{x}_1^g\|. \tag{2.8}$$

and (2) rotation matrices of the beam extremities, i.e. $\mathbf{R}_1^l$ and $\mathbf{R}_2^l$. $\mathbf{R}_1^l$ denotes the 3D finite rotation from $[\mathbf{r}_1, \mathbf{r}_2, \mathbf{r}_3]$ to $\left[\mathbf{t}_1^1, \mathbf{t}_2^1, \mathbf{t}_3^1\right]$. $\mathbf{R}_2^l$ denotes the 3D finite rotation from $[\mathbf{r}_1, \mathbf{r}_2, \mathbf{r}_3]$ to $\left[\mathbf{t}_1^2, \mathbf{t}_2^2, \mathbf{t}_3^2\right]$.

The orientations of the beam extremities in the deformed configuration can be obtained through two rotation sequences. The first rotation sequence is

$$\mathbf{e}_i \xrightarrow{\mathbf{R}_0} \mathbf{e}_i^0 \xrightarrow{\mathbf{R}_j^g} \mathbf{t}_i^j \ (i = 1, 2, 3, j = 1, 2).$$

Starting from $\mathbf{e}_i$ which is the global Cartesian axes, we apply initial orientation matrix $\mathbf{R}_0$ and arrive at the follower axes $\mathbf{e}_i^0$. Measured from the follower axes, we apply the global nodal rotation $\mathbf{R}_j^g$ and arrive at the current beam extremity

orientation $\mathbf{t}_i^j$. The second rotation sequence is

$$\mathbf{e}_i \xrightarrow{\mathbf{R}_\mathrm{r}} \mathbf{r}_i \xrightarrow{\mathbf{R}_j^l} \mathbf{t}_i^j \ (i = 1,2,3, j = 1,2).$$

Starting from $\mathbf{e}_i$ we apply finite rotation matrix $\mathbf{R}_\mathrm{r}$ and arrive at the local Cartesian axes $\mathbf{r}_i$. From $\mathbf{r}_i$ we apply the local nodal rotation $\mathbf{R}_j^l$ and arrive at the current beam extremity orientation $\mathbf{t}_i^j$. The latter should be viewed as the rotation around fixed axes, i.e. the rotation axes remain fixed but the rotation sequence itself is inverted. Interested readers can refer to Battini's work [49] (Sections 4.1 and 4.2.1) and more retrospectively Argyris' work [50] (Section 2) for elaboration pertaining to the rotation axes and the rotation sequence. Therefore, the rotation from $\mathbf{e}_i$ to $\mathbf{t}_i^j$ can be parameterized either as $\mathbf{R}_j^g \mathbf{R}_0$ or as $\mathbf{R}_\mathrm{r} \mathbf{R}_j^l$ (for the latter case, the multiplication of rotation matrices is inverted). The equivalence of $\mathbf{R}_j^g \mathbf{R}_0 = \mathbf{R}_\mathrm{r} \mathbf{R}_j^l$ decouples the strain inducing rotation $\mathbf{R}_j^l$ from the overall rotation $\mathbf{R}_j^g$ for both beam extremities:

$$\mathbf{R}_j^l = \mathbf{R}_\mathrm{r}^T \mathbf{R}_j^g \mathbf{R}_0 \qquad (j = 1,2). \tag{2.9}$$

To summarize, the kinematic variables of the beam element in the global coordinate frame and the local co-rotational coordinate frame (i.e. rotating with the beam) are aggregated as $\mathbf{d}^g$ and $\mathbf{d}^l$ in Eq. (2.10):

$$\mathbf{d}^g = \left(\mathbf{u}_1^g, \mathbf{R}_1^g, \mathbf{u}_2^g, \mathbf{R}_2^g\right), \qquad \mathbf{d}^l = \left(\mathrm{u}^l, \mathbf{R}_1^l, \mathbf{R}_2^l\right). \tag{2.10}$$

In the implementation, Rodrigues' formula is used to express each rotation matrix in a 3×1 rotation vector Ψ [51]. This rewrites Eq. (2.10) as

$$\mathbf{d}^g = \left(\mathbf{u}_1^g, \Psi_1^g, \mathbf{u}_2^g, \Psi_2^g\right) \qquad \mathbf{d}^l = \left(\mathrm{u}^l, \Psi_1^l, \Psi_2^l\right). \tag{2.11}$$

The internal force and the tangential stiffness conjugate with $\mathbf{d}^g$ and $\mathbf{d}^l$ can be established by resorting to the equality of virtual work. For details about this transformation, the reader is referred to [41].

2.3.2. Plastic hinge model

Powell and Chen's plastic hinge model [42, 48] defines the beam deformation as shown in Fig. 2.7 for a beam bundle in an infinitesimal strain and displacement formulation. In this work, the proposed beam FE with embedded plastic hinges is defined in the local frame of the co-rotational formulation.

The kinematic variables are: (1) the transverse bending curvatures at both extremities, i.e. $\theta_{\mathbf{r}_2}^1$ and $\theta_{\mathbf{r}_3}^1$ for the first beam extremity, $\theta_{\mathbf{r}_2}^2$ and $\theta_{\mathbf{r}_3}^2$ for the second beam extremity; (2) twist angle $\psi_{\mathbf{r}_1}$; and (3) axial strain $\varepsilon_{\mathbf{r}_1}$. The corresponding energy conjugate quantities are: (1) the transverse bending moments at both extremities, i.e. $M_{\mathbf{r}_2}^1$ and $M_{\mathbf{r}_3}^1$ for the first beam extremity, $M_{\mathbf{r}_2}^2$ and $M_{\mathbf{r}_3}^2$ for the second beam extremity; (2) the torque $T_{\mathbf{r}_1}$; (3) the axial force $F_{\mathbf{r}_1}$. More detailed information can be found in [42].

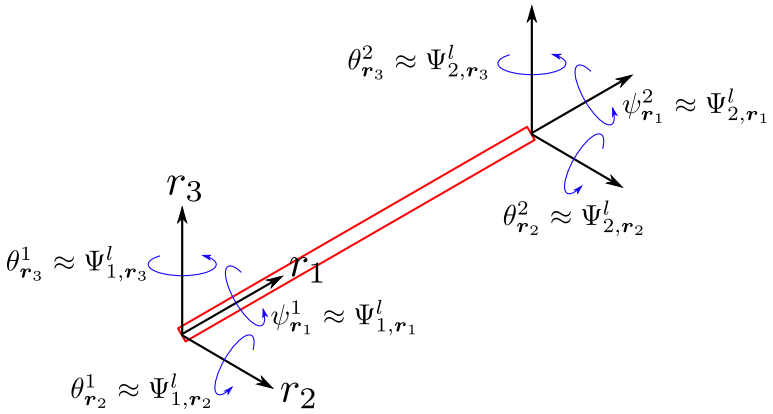

Figure 2.6: Equating the rotation vector to the twist and the transverse curvatures. $[\mathbf{r}_1, \mathbf{r}_2, \mathbf{r}_3]$ denotes the triad of the local coordinate frame. $\Psi^l_i = [\Psi^l_{i,\mathbf{r}_1}, \Psi^l_{i,\mathbf{r}_2}, \Psi^l_{i,\mathbf{r}_3}]$, $i = 1, 2$ denotes the rotation vector of the beam extremity. $\psi^i_{\mathbf{r}_1}$, $i = 1, 2$ is the twist around $\mathbf{r}_1$ axis. $\theta^i_{\mathbf{r}_2}$, $i = 1, 2$ denotes the curvature around $\mathbf{r}_2$ axis. $\theta^i_{\mathbf{r}_3}$, $i = 1, 2$ denotes the curvature around r_3 axis.

The strain definitions above are projected to the kinematic variables of the local frame in the co-rotational formulation by introducing the approximation to equate the three components of the rotation vector to the three rotating angles with respect to the orthogonal basis $[\mathbf{r}_1, \mathbf{r}_2, \mathbf{r}_3]$ of the local coordinate (see Fig. 2.6).

$$\Psi^l_i = [\Psi^l_{i,\mathbf{r}_1}, \Psi^l_{i,\mathbf{r}_2}, \Psi^l_{i,\mathbf{r}_3}] \approx [\psi^i_{\mathbf{r}_1}, \theta^i_{\mathbf{r}_2}, \theta^i_{\mathbf{r}_3}] \qquad i = 1, 2. \tag{2.12}$$

Using Eq. (2.12), the relation between the kinematic variables can be written as:

$$\begin{bmatrix} \theta^1_{\mathbf{r}_3} \\ \theta^2_{\mathbf{r}_3} \\ \theta^1_{\mathbf{r}_2} \\ \theta^2_{\mathbf{r}_2} \\ \psi_{\mathbf{r}_1} \\ \varepsilon_{\mathbf{r}_1} \end{bmatrix} = \begin{bmatrix} 0 & 0 & 1 & 0 & 0 & 0 & 0 \\ 0 & 0 & 0 & 0 & 0 & 1 & 0 \\ 0 & 0 & 0 & 1 & 0 & 0 & 0 \\ 0 & 0 & 0 & 0 & 0 & 0 & 1 \\ 0 & -1 & 0 & 0 & 1 & 0 & 0 \\ \frac{1}{l_0} & 0 & 0 & 0 & 0 & 0 & 0 \end{bmatrix} \begin{bmatrix} u^l \\ \Psi^l_{1,\mathbf{r}_1} \\ \Psi^l_{1,\mathbf{r}_2} \\ \Psi^l_{1,\mathbf{r}_3} \\ \Psi^l_{2,\mathbf{r}_1} \\ \Psi^l_{2,\mathbf{r}_2} \\ \Psi^l_{2,\mathbf{r}_3} \end{bmatrix} \tag{2.13}$$

where l_0 denotes the original length of the beam.

A beam bundle consists of three components (Fig. 2.7): an elastic beam element and two plastic hinges. The deformation of the ensemble is thus the sum of the elastic deformation of the elastic beam and the plastic deformation of the plastic hinges. Table 2.2 and Fig. 2.7 illustrate how the deformations of the elastic beam and the plastic hinges are aggregated into the beam bundle. Superscript $1/2$ denotes the first/second beam extremity. Subscript e/p denotes the elastic or plastic deformation.

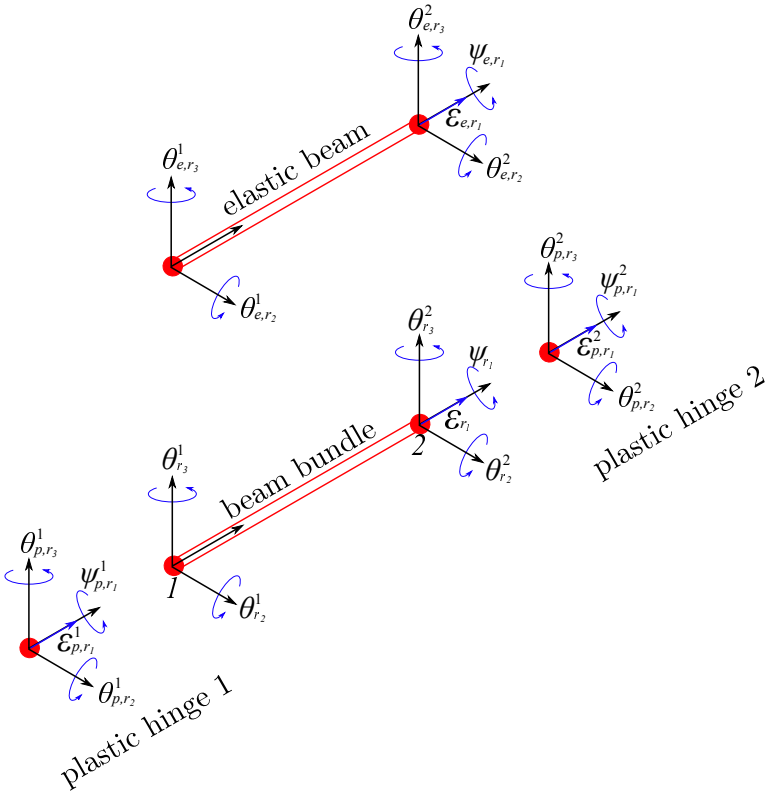

Figure 2.7: The definition and the composition of the beam deformation.

Beam bundle		Elastic beam		Plastic hinge 1		Plastic hinge 2
$\theta^1_{\mathbf{r}_2}$	=	$\theta^1_{e,\mathbf{r}_2}$	+	$\theta^1_{p,\mathbf{r}_2}$		
$\theta^2_{\mathbf{r}_2}$	=	$\theta^2_{e,\mathbf{r}_2}$			+	$\theta^2_{p,\mathbf{r}_2}$
$\theta^1_{\mathbf{r}_3}$	=	$\theta^1_{e,\mathbf{r}_3}$	+	$\theta^1_{p,\mathbf{r}_3}$		
$\theta^2_{\mathbf{r}_3}$	=	$\theta^2_{e,\mathbf{r}_3}$			+	$\theta^2_{p,\mathbf{r}_3}$
$\psi_{\mathbf{r}_1}$	=	$\psi_{e,\mathbf{r}_1}$	+	$\psi^1_{p,\mathbf{r}_1}$	+	$\psi^2_{p,\mathbf{r}_1}$
$\varepsilon_{\mathbf{r}_1}$	=	$\varepsilon_{e,\mathbf{r}_1}$	+	$\varepsilon^1_{p,\mathbf{r}_1}$	+	$\varepsilon^2_{p,\mathbf{r}_1}$

Table 2.2: Decomposition of the total deformation of the beam bundle.

The Timoshenko beam formulation is adopted for the elastic beam element because the strut of the metallic lattice is usually not slender (Fig. 2.2), which makes the shear effect non-negligible. The use of Timoshenko beam FEs formulation is rather common for the modeling of lattice structures [15, 16, 52].

The plastic constitutive setting uses Mróz's multi-layer J_2-plasticity kinematic hardening model [53–56]. It consists of several inclusive and homologous yield surfaces in the generalized stress space and a rigid piecewise linear hardening approximation (Fig. 2.8). This allows for solving the plastic problem efficiently without requiring an iterative return-mapping algorithm.

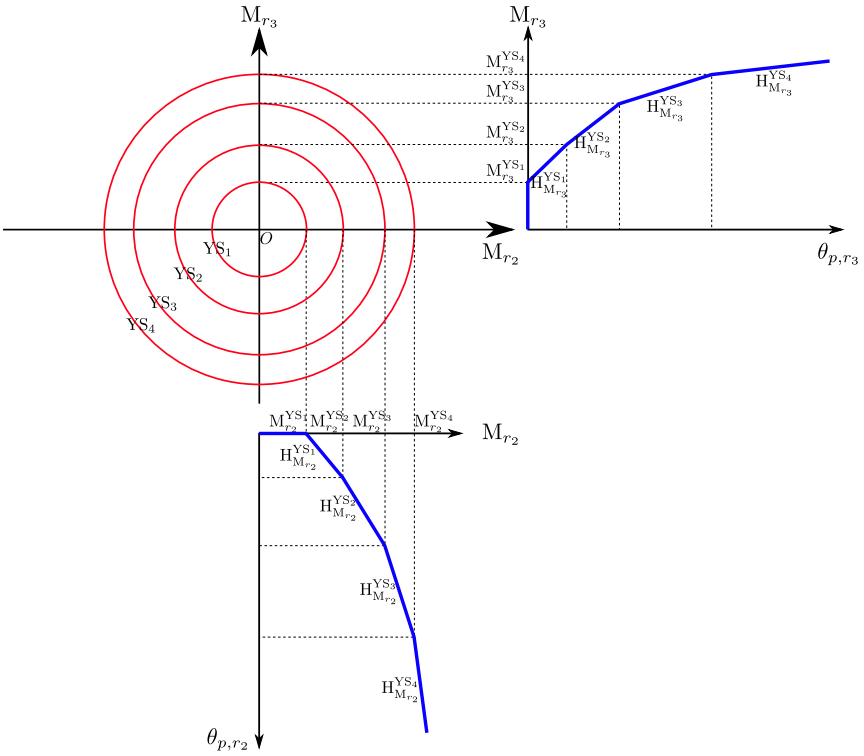

Figure 2.8: The plastic hinge behavior projected onto the plane spanned by bending moments $M_{\mathbf{r}_2}$ and $M_{\mathbf{r}_3}$.

The generalized stress space of the plastic hinge is four-dimensional as it includes the two transverse bending moments ($M_{\mathbf{r}_2}$ and $M_{\mathbf{r}_3}$), the torque ($T_{\mathbf{r}_1}$), and the axial force ($F_{\mathbf{r}_1}$).

The jth yield surface YS_j is assumed to be defined by the yield function ϕ_j as

[42]:

$$\phi_j(M_{r_2}, M_{\mathbf{r}_3}, T_{\mathbf{r}_1}, F_{\mathbf{r}_1}) = \left[\frac{M_{\mathbf{r}_2} - M_{\mathbf{r}_2}^{0,\mathrm{YS}_j}}{M_{\mathbf{r}_2}^{\mathrm{YS}_j}}\right]^2 + \left[\frac{M_{\mathbf{r}_3} - M_{\mathbf{r}_3}^{0,\mathrm{YS}_j}}{M_{\mathbf{r}_3}^{\mathrm{YS}_j}}\right]^2 + \left[\frac{T_{\mathbf{r}_1} - T_{\mathbf{r}_1}^{0,\mathrm{YS}_j}}{T_{\mathbf{r}_1}^{\mathrm{YS}_j}}\right]^2 + \left[\frac{F_{\mathbf{r}_1} - F_{\mathbf{r}_1}^{0,\mathrm{YS}_j}}{F_{\mathbf{r}_1}^{\mathrm{YS}_j}}\right]^2 - 1 = 0 \tag{2.14}$$

where $\left[M_{\mathbf{r}_2}^{0,\mathrm{YS}_j}, M_{\mathbf{r}_3}^{0,\mathrm{YS}_j}, T_{\mathbf{r}_1}^{0,\mathrm{YS}_j}, F_{\mathbf{r}_1}^{0,\mathrm{YS}_j}\right]$ and $\left[M_{\mathbf{r}_2}^{\mathrm{YS}_j}, M_{\mathbf{r}_3}^{\mathrm{YS}_j}, T_{\mathbf{r}_1}^{\mathrm{YS}_j}, F_{\mathbf{r}_1}^{\mathrm{YS}_j}\right]$ denote the center and the size of the jth yield surface in the generalized stress space.

Fig. 2.8 shows an arbitrary configuration of the plastic hinge in the generalized stress space when it is projected onto the plane formed by $M_{\mathbf{r}_2}$ and $M_{\mathbf{r}_3}$ axes. Here the plastic hinge is predefined using four yield surfaces, i.e. YS_1, YS_2, YS_3 and YS_4. Constant hardening moduli are associated with each yield surface so that when the jth yield surface is active, the hardening modulus of the plastic hinge becomes $\left[H_{M_{\mathbf{r}_2}}^{\mathrm{YS}_j}, H_{M_{\mathbf{r}_3}}^{\mathrm{YS}_j}, H_{T_{\mathbf{r}_1}}^{\mathrm{YS}_j}, H_{F_{\mathbf{r}_1}}^{\mathrm{YS}_j}\right]$. Inside the first yield surface YS_1, the plastic hinge is rigid. Therefore, the behavior of the plastic hinge is piecewise-linear-rigid-plastic-strain-hardening.

The solution procedure of the plastic hinge model in case of uniaxial loading is illustrated in Fig. 2.9. Supposing that the beam bundle is initially elastic and in equilibrium (ε_n, F_n), where ε_n denotes the deformation of the beam bundle (i.e. the collection of the transverse bending curvatures, axial twist and axial strain), F_n denotes the corresponding load level (i.e. the collection of the transverse bending moments, torque and axial force). The two plastic hinges remain rigid and ε_n^e is purely elastic, i.e. $\varepsilon_n = \varepsilon_n^e$. With a total strain increment $\Delta\varepsilon$ prescribed, a new equilibrium is achieved with $\varepsilon_{n+1} = \varepsilon_n + \Delta\varepsilon$ and F_{n+1} denotes the unknown to be solved for.

The total strain increment is decomposed into the incremental deformation of the elastic beam $\Delta\varepsilon^e$, and the incremental deformation of the first and second plastic hinges $\Delta\varepsilon^{p_1}$, $\Delta\varepsilon^{p_2}$, respectively. The permissible solution satisfies the following constraint:

$$\Delta\varepsilon = \Delta\varepsilon^e + \Delta\varepsilon^{p_1} + \Delta\varepsilon^{p_2}. \tag{2.15}$$

Thanks to the predefined piece-wise linear responses for the elastic beam and the two plastic hinges (Fig. 2.9), ($F - \Delta\varepsilon^e$, $F - \Delta\varepsilon^{p_1}$, $F - \Delta\varepsilon^{p_2}$) are linear between adjacent deflection points (deflection points are the load levels where the response curve of either of the two plastic hinges changes its slope). This enables Eq. (2.15) to be readily fulfilled in an incremental way, i.e. to accumulate the deformation increments between adjacent deflection points until Eq. (2.15) is satisfied. The internal force of the new equilibrium F_{n+1} can then be determined. This rules out the necessity of an iterative return mapping procedure. Furthermore, the tangential stiffness of the beam bundle is computed by inversing the system compliance, which

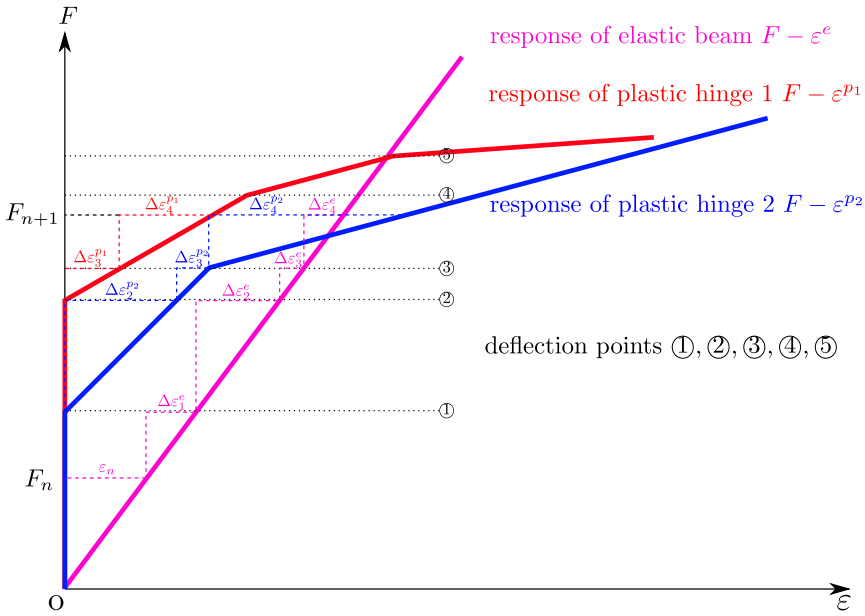

Figure 2.9: Solution procedure of the plastic hinge model illustrated in case of uniaxial loading. $\Delta\varepsilon_i^e$, $\Delta\varepsilon_i^{p_2}$ and $\Delta\varepsilon_i^{p_1}$ are the deformation increments of the elastic beam and the two plastic hinges. Subscript i indexes the intervals between adjacent deflection points $i-1$ and i.

is the sum of the compliance of each component. This avoids solving an system that can be ill-conditioned due to the infinite stiffness of the rigid plastic hinges. For details on the used plastic hinge model the reader is referred to [42].

A drawback of the formulation is that the quadratic rate of convergence is lost. This is attributed to two reasons: (1) Eq. (2.12) is an approximation rather than rigorous and consistent derivation; (2) the plastic hinge behavior is piecewise linear and more iterations are needed to switch between the segments.

2.4. Performance study

In this section, we verify the performance of the proposed generalized quasicontinuum method for BCC lattice structures.

2.4.1. Beam representation of a single BCC unit cell

To model the BCC lattice structure using beam finite elements, we first establish the beam representation for a single BCC unit cell.

The same geometric dimensions and material properties are used here as proposed in [16] for metallic BCC lattice structures fabricated out of 316L stainless steel powder through Selective Laser Melting (SLM) procedure. The unit cell is of dimensions $2\,\text{mm} \times 2\,\text{mm} \times 2\,\text{mm}$. The beam discretization scheme of the BCC unit

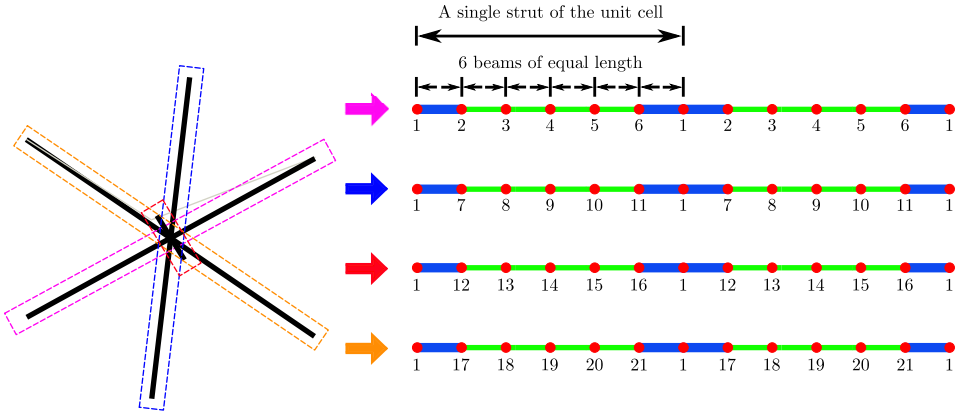

Figure 2.10: Beam discretization of the BCC unit cell and the classification of the types of the micro-structural nodes. Each of the eight struts is represented using six beam elements of equal length. These beam elements are of two kinds. The blue beams (▬) are connected to the junctions of the struts with a larger cross section to mimic material concentration at the strut junctions. The green beams (▬) represent the intermediate parts of the struts with a smaller cross section. Node types are indicated with numbers below each micro-structural node.

cell is illustrated in Fig. 2.10.

Each strut of the unit cell is represented using six beam finite elements of equal length with a circular cross section. To model the inherent material concentration at the junctions of the struts, different diameters are assigned to the beam elements adjacent to the junctions (with a diameter of 0.23 mm) and in the intermediate part of the struts (with a diameter of 0.185 mm) as in [16].

Consequently, 49 micro-structural nodes are present in a unit cell, which are classified into 21 types due to their connectivity (Fig. 2.10). The kinematic variables of each type of micro-structural node are interpolated using the same representative kinematic variables of the macro-scale interpolation elements. How to optimally classify the micro-structural nodes into the lowest number of types is part of future work. Here, the optimal classification of the micro-structural nodes means the micro-structural nodes in a unit cell are classified into the smallest number of types at no compromise of the accuracy. In the most extreme case, each micro-structural node in a unit cell would be considered as an individual type. Such a classification scheme would generate the most accurate results but would surely compromise the computational efficiency. For the current classification scheme, the authors performed a sensitivity analysis by comparing the results of the current classification scheme with that of the most extreme classification scheme and the results were almost the same. This at least confirms that the current classification scheme is better than the most extreme one. Yet how to determine the optimal classification scheme is considered out of scope for the current contribution.

The material parameters of the proposed 3D co-rotational beam with embedded

plastic hinges include the material parameters of the elastic beam component and the two plastic hinges. For the elastic beam component, its Young's modulus is set to $E = 140$ GPa and its Poisson's ratio is set to be $\nu = 0.3$.

For the plastic hinges, it is assumed that the plastic bending of the struts/beams is the only irreversible deformation, neglecting the effects of torque $T_{\mathbf{r}_1}$ and axial force $F_{\mathbf{r}_1}$ from the yield function in Eq. (2.14). This is because the current work aims at reproducing plastic bending failure of metallic printed lattices. Another reason is the lack of knowledge about how the torque and normal force may influence the bending behavior of the strut, which has made us decide to ignore them. Consequently, only the piecewise linear rigid-plastic-strain-hardening curves of the bending moments $M_{\mathbf{r}_2}$ and $M_{\mathbf{r}_3}$ (as in Fig. 2.8) are needed to define the behavior of the plastic hinges.

To configure the piecewise linear rigid-plastic-strain-hardening curves of the bending moments $M_{\mathbf{r}_2}$ and $M_{\mathbf{r}_3}$, the initial yield limit (i.e. $M_{\mathbf{r}_2}^{\mathrm{YS}_1}$ and $M_{\mathbf{r}_3}^{\mathrm{YS}_1}$ in Fig. 2.8) and the hardening responses (i.e. $M_{\mathbf{r}_2/\mathbf{r}_3}^{\mathrm{YS}_2}$, $M_{\mathbf{r}_2/\mathbf{r}_3}^{\mathrm{YS}_3}$, $M_{\mathbf{r}_2/\mathbf{r}_3}^{\mathrm{YS}_4}$, $H_{\mathrm{M}_{\mathbf{r}_2/\mathbf{r}_3}}^{\mathrm{YS}_1}$, $H_{\mathrm{M}_{\mathbf{r}_2/\mathbf{r}_3}}^{\mathrm{YS}_2}$, $H_{\mathrm{M}_{\mathbf{r}_2/\mathbf{r}_3}}^{\mathrm{YS}_3}$, $H_{\mathrm{M}_{\mathbf{r}_2/\mathbf{r}_3}}^{\mathrm{YS}_4}$ in Fig. 2.8) need to be defined.

The initial yield limit of the bending moments $M_{\mathbf{r}_2}$ and $M_{\mathbf{r}_3}$ of the plastic hinge (i.e. $M_{\mathbf{r}_2}^{\mathrm{YS}_1}$ and $M_{\mathbf{r}_2}^{\mathrm{YS}_1}$ in Fig. 2.8) is determined from the plastic bending moment of a circular cross section with a bi-linear material model (with Young's modulus $E = 140$ GPa, hardening modulus $E_T = 1$ GPa and yield stress $\sigma_0 = 140$ MPa) [57]. The initial yield limit of $M_{\mathbf{r}_2}$ and $M_{\mathbf{r}_3}$ is assumed to be the bending moment of the circular cross section when the distance between the neutral axis and the initially yield fiber amounts to 95% of the radius. Using the geometrical and material properties given earlier and the closed form expression for the plastic bending moment in [57], values of $0.9050\,\mathrm{N}\cdot\mathrm{mm}$ and $1.7391\,\mathrm{N}\cdot\mathrm{mm}$ are determined for beams with diameters of 0.185 mm and of 0.230 mm, respectively.

The hardening responses are shown in Fig. 2.11, which using four yield surfaces. To approximate perfect plasticity while facilitating numerical stability, the hardening modulus for the four yield surfaces are set to small values and gradually decrease (the slopes of the four hardening segments are set to be $4°$, $3°$, $2°$ and $1°$ respectively).

2.4.2. Unconstrained compression of a BCC lattice

In this section, the response of a BCC lattice under unconstrained compression is simulated. The results of the generalized quasicontinuum method are compared to those of the DNS to assess its computational efficiency and accuracy.

The lattice consists of $6 \times 6 \times 6$ BCC unit cells, each of which is sized $2\mathrm{mm} \times 2\mathrm{mm} \times 2\mathrm{mm}$, and the imposed compression depth is $2\mathrm{mm}$. The bottom of the lattice is constrained in the normal direction and the prescribed displacement is imposed at the top of the lattice. Rigid body movement is eliminated.

Two interpolation schemes are investigated as shown in Fig. 2.12. In Fig. 2.12a, half of the lattice is fully resolved (FRD), and the other half of the lattice is coarse-grained (CGD) using six linear tetrahedral interpolation elements. The behavior of the lattice in the FRD and the CGD are monitored simultaneously. In Fig. 2.12b, the

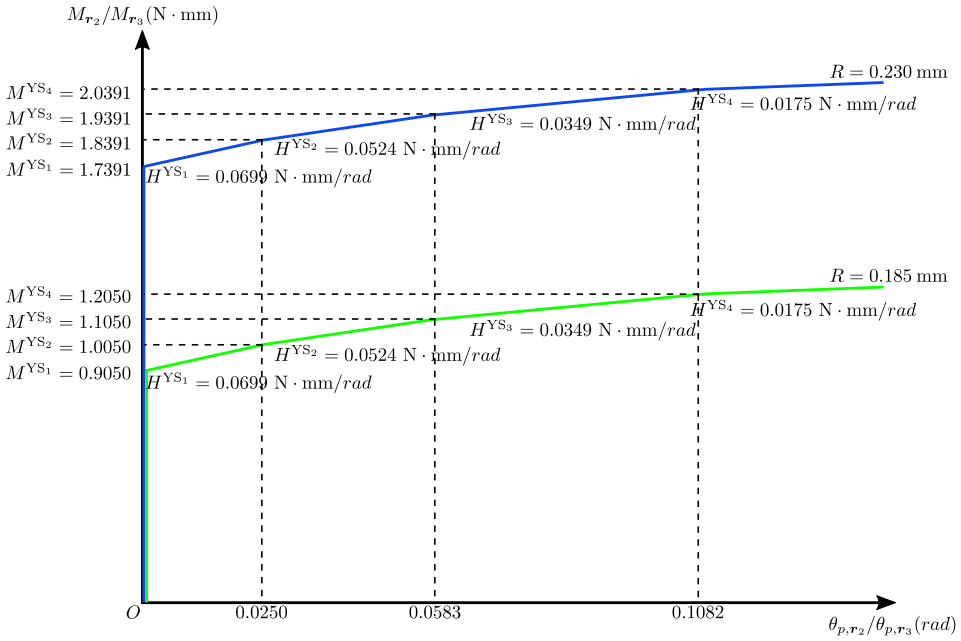

Figure 2.11: The piecewise linear rigid-plastic-strain-hardening curves of the plastic hinge for beams with diameter of 0.230 mm and 0.185 mm. M^{YS_i} and H^{YS_i} are the yield bending moment and hardening modulus of ith yield surface.

entire lattice is coarse-grained using six linear tetrahedral interpolation elements.

In each tetrahedral interpolation element, five Gauss quadrature points (GQPs) are used (a convergence analysis is performed in advance and it is found that five Gauss quadrature points is the minimum number of Gauss quadrature points that guarantees convergence). The locations of the sampling beams are presented in Figs. 2.12c and 2.12d. Purely elastic and elastoplastic computations are performed using the parameters set described above.

Table 2.3 compares the different simulations in terms of the number of DoFs and sampling beams, accuracy and computational time spent on relevant subprocedures. To measure the error induced by the coarse-graining, the external work is compared (based on the curves in Fig. 2.13 using the trapezoidal rule). The relative error in terms of the external work is 3.76% for the elastic analysis and 2.60% for the elastoplastic analysis.

The reaction force versus the downward displacement is plotted in Fig. 2.13. Fig. 2.14 shows the deformed shape obtained from the generalized quasicontinuum method. The following conclusions can be drawn from the results: The coarse-graining of the generalized quasicontinuum method can significantly reduce the size of the computer model and alleviate the computational demand.

When the entire lattice is coarse-grained, the number of DoFs is reduced by 98.17% and the number of sampling beams is reduced by 86.11%. The reduction

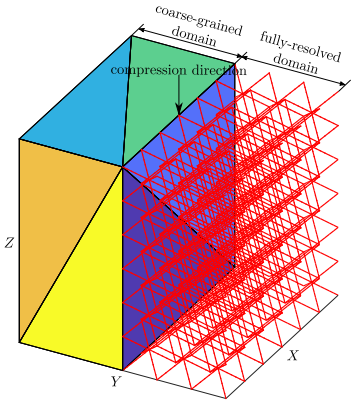

(a) first interpolation scheme

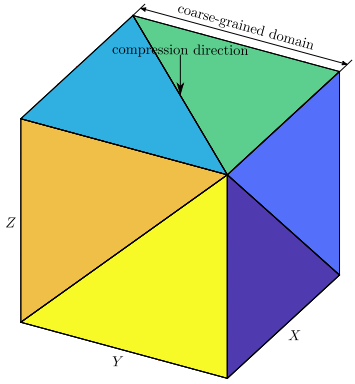

(b) second interpolation scheme

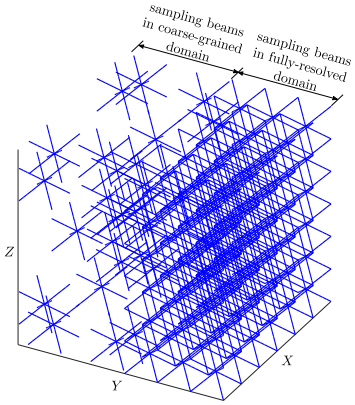

(c) Distribution of sampling beams of first interpolation scheme

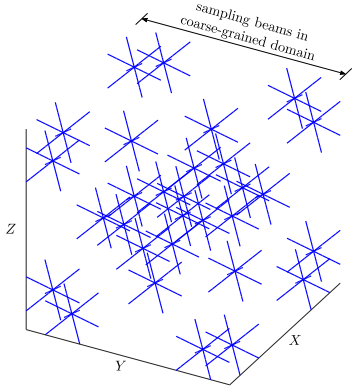

(d) Distribution of sampling beams of second interpolation scheme

Figure 2.12: Interpolation and summation schemes of the generalized quasicontinuum modeling for the unconstrained compression of the BCC lattice.

in the number of DoFs implies less efforts in solving the governing equations, as can be observed from the time for 'solving governing equations' in Table 2.3. The reduction in the number of sampling beams implies less efforts for the assembly of the 'stiffness matrix', the assembly of the 'internal force vector' and the update of the 'history variables' in Table 2.3. The time consumptions of 'assemble stiffness matrix' and 'assemble force vector' are comparable because the most time consuming operation of the 3D co-rotational beam formulation is the uncoupling of the rigid body movement and the deformation, which is performed in both the stiffness matrix and the internal force vector. For the elastic analysis, the required total computational time is reduced by 87.50% (an acceleration factor of 8) while for the elastoplastic analysis, it is reduced by 97.29% (an acceleration factor of 37). The observed symmetry between the left and the right half of the deformed lattice

Items	Elastic analysis			Elastoplastic analysis		
	DNS	$\frac{1}{2}$FRD+$\frac{1}{2}$CGD	CGD	DNS	$\frac{1}{2}$FRD+$\frac{1}{2}$CGD	CGD
Overall computational time	655,2	368,1	81,9	44 916,3	14 378,7	1 218,7
Configure interpolation & select sampling beams	/	3,1	0,8	/	3,3	0,8
Assemble stiffness matrix	320,5	193,7	42,3	24 430,1	7 821,2	660,9
Solve governing equations	6,2	3,2	0,3	471,3	125,5	4,1
Assemble force vector	257,6	155,4	33,7	19 926,7	6 408,3	547,5
Update history variables	4,3	2,6	0,6	4,2	3,1	0,6
Overhead	66,5	9,9	4,3	84,1	17,3	4,8
External work (N·mm)	994,5	1 016,0	1 031,9	445,8	453,4	457,4
Number of DoFs	55 194	28 458	1 008	55 194	28 458	1 008
Number of sampling beams	10 368	6 624	1 440	10 368	6 624	1 440

Table 2.3: Comparison of DNS and the generalized quasicontinuum simulations in terms of computation time, size and accuracy. Computational time is measured in seconds when running the MATLAB based in-house code with a DELL desktop equipped with Intel i7-7700 4.2GHz CPU. Overhead includes the time elapses in reading in model and allocating DoFs, generating output files etc.

in Fig. 2.14 also demonstrates the sufficient accuracy of the generalized quasicontinuum approximation for this example.

As expected, coarse-graining makes the structure stiffer. The stiffness of the lattice and the predicted reaction force are positively correlated with the size of the coarse-grained domain (Fig. 2.13) because the kinematic approximation in the coarse-grained domain is generally poorer than in the fully-refined domain.

Interesting is that the speed up factors for the elastic and elastoplastic simulations are completely different (8 vs.37), indicating that the method is more useful for elastoplastic than for elastic analyses. The convergence criterion we use is based on measuring the relative error of the out-of-balance force residual. The number of structural iterations (as shown in Fig. 2.15) is significantly higher because of the way plasticity is treated in the hinges, as a natural consequence of the use of the chosen formulation (i.e. the piecewise linear rigid-plastic-strain-hardening responses). The source of the larger number of iterations has been identified to be the passing from one linear segment to the other in the plastic hardening description, this happening simultaneously in a large number of hinges of the model. Therefore, the more hinges are incorporated, the more structural iterations are required to solve the equilibrium problem, leading to an additional advantage of the generalized quasicontinuum method with respect to the DNS. Therefore, the generalized quasicontinuum modeling achieves higher speed up factors for elastoplastic simulations as it requires less iterations per increment in the elastoplastic regime.

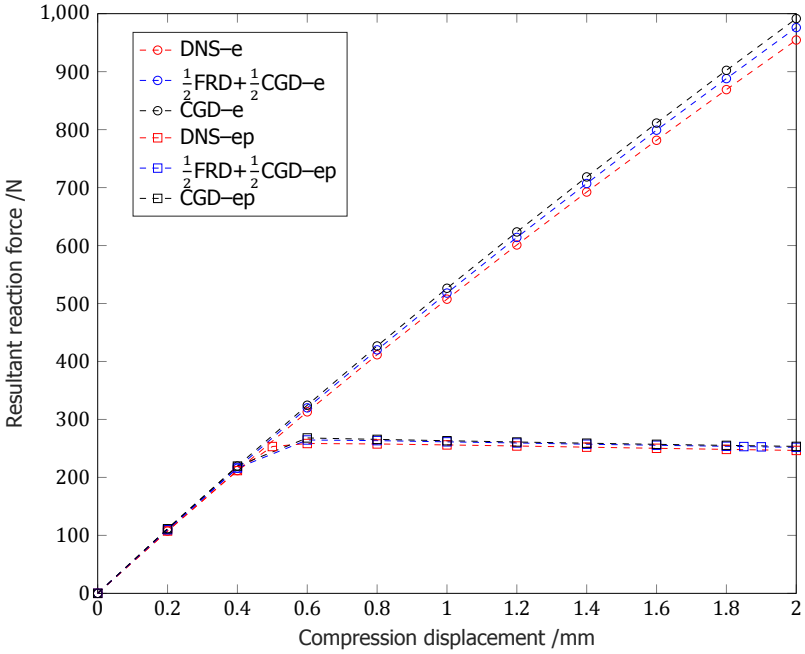

Figure 2.13: Reaction force versus top surface displacement for unconstrained compression of the BCC lattice, '-e' denotes the elastic analysis, '-ep' denotes the elastoplastic analysis.

2.4.3. Three point bending of a notched BCC lattice

In this section, the efficiency of the generalized quasicontinuum method with respect to the choice of the coarse-grained domain (CGD) is investigated for an example with more complex kinematics. The mechanical behavior of a notched BCC lattice under three point bending is simulated.

The lattice consists of $5 \times 62 \times 5$ BCC unit cells and a notch of size $5 \times 2 \times 2$ unit cells at the center of the lattice (Fig. 2.16). The lattice is simply supported at both ends and a prescribed displacement of 15 mm is introduced in the middle of the specimen on the opposite side of the notch (Fig. 2.16). Strain localization is expected close to the notch while a more homogeneous displacement field will develop close to the left and right extremities of the lattice.

There is no easy a priori method to identify the appropriate size of the domain that can be coarse-grained without a loss of accuracy [58]. therefore, five candidate interpolation schemes are investigated (Fig. 2.17). Each cube shaped coarse-grained domain is of size $5 \times 5 \times 5$ unit cells, divided into six macro-scale linear tetrahedral interpolation elements with five Gauss quadrature points. Table 2.4 lists the model size of the direct numerical simulation (DNS) and the five generalized quasicontinuum models.

Elastoplastic analyses are performed using the previous material and geomet-

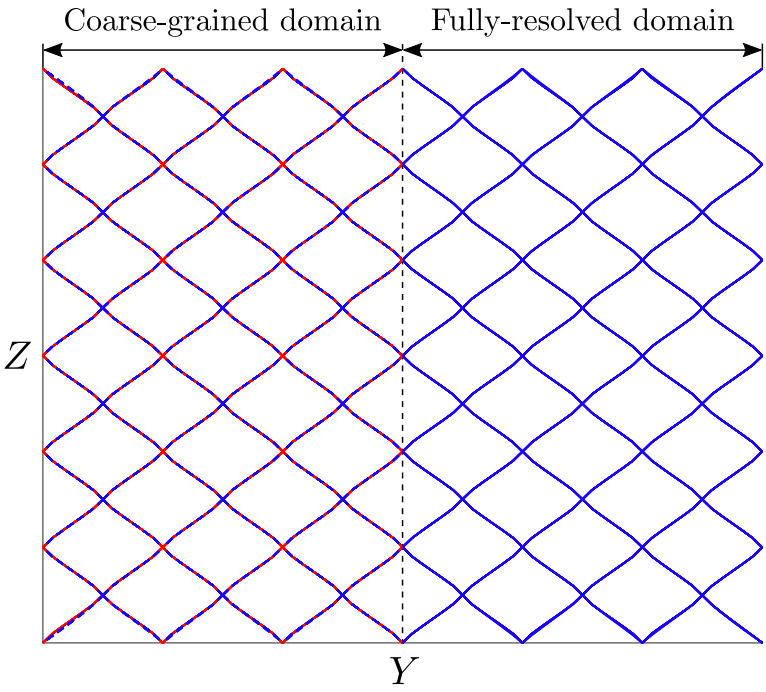

Figure 2.14: Deformed shape of the BCC lattice viewed from the X axis. The part of lattice in the fully-resolved domain (FRD) is rendered in blue and the other half of lattice in the coarse-grained domain (CGD) is rendered in red. To show the symmetry, the part of lattice in FRD is mirrored and superimposed onto CGD using dashed lines.

Model	Number of DoFs	Number of sampling beams	External work relative to DNS	Initial stiffness relative to DNS	Reaction force at maximum strain relative to DNS
DNS	389 916	73 440	100%	100%	100%
83.3% FRD	327 840	64 320	102.5%	106.7%	100.2%
66.7% FRD	265 188	55 200	104.4%	112.2%	100.3%
50.0% FRD	202 536	46 080	108.1%	123.9%	100.9%
33.3% FRD	139 884	36 960	114.0%	149.6%	101.4%
16.7% FRD	77 232	27 840	122.8%	211.5%	102.1%

Table 2.4: Comparison of DNS and generalized quasicontinuum simulations in terms of model size and accuracy as a function of the volumetric percentage of the fully-resolved domain (FRD).

rical parameters. The reaction force is presented as a function of the imposed displacement in Fig. 2.18. The error induced by the coarse-graining procedure

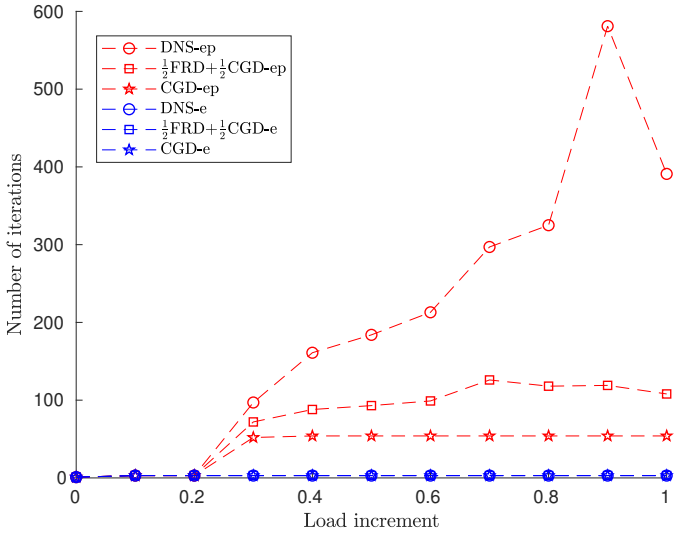

Figure 2.15: Number of iterations versus load increment.

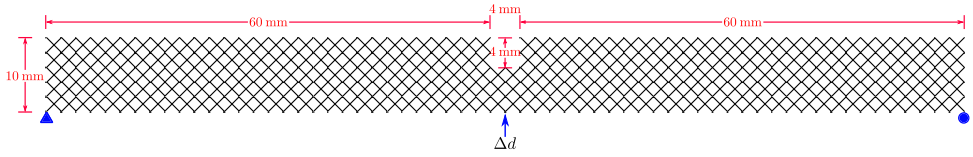

(a) Front view. ▲ and • denotes the simple support. Δd denotes the prescribed displacement. The boundary conditions are imposed throughout the thickness.

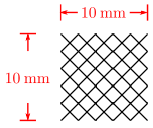

(b) Side view.

Figure 2.16: Dimensions of the notched BCC lattice and the boundary conditions of the three point bending test.

is quantified by the external work calculated from the force–displacement curves using the trapezoidal rule (Table 2.4). At the end of the loading procedure, the reaction force appears to reach a plateau, which results from the plastic bending of the beam elements in the proximity of the notch. Although the five interpolation schemes lead to varying initial stiffnesses, the predicted reaction forces at the end of the loading process are relatively consistent. When the final reaction force is considered, the 5th interpolation scheme can reduce the number of DoFs by 80.19%,

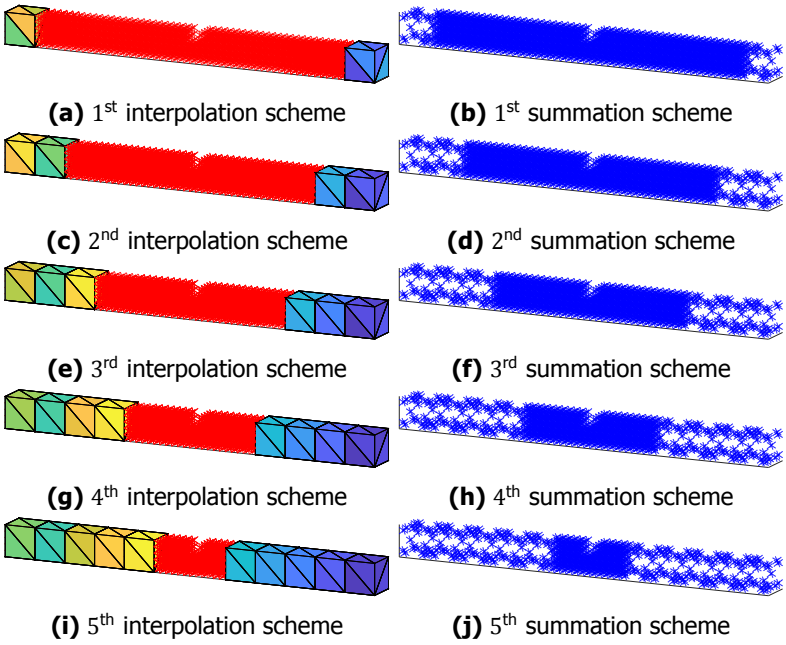

Figure 2.17: The five interpolation schemes for the generalized quasicontinuum modeling of the three point bending of the notched BCC lattice and distribution of sampling beams.

the number of sampling beams by 62.09% while introducing a relative error of only 2.12%. Coarse-graining stiffens the structure, which is the reason why the initial stiffnesses predicted by the interpolation schemes are different than that predicted by the DNS. The generalized quasicontinuum method provides a good approximation of the developed plastic response, but the elastic stiffness is sensitive to the CGD size in this example.

Since the required size of FRD and CGD are generally not known a priori, this leaves the determination of the appropriate sizes of FRD and CGD when applying the generalized quasicontinuum method an empirical job for the users. Adaptive coarse-graining strategies as those of [35, 58] will further enhance the generalized quasicontinuum method by eliminating the human factor, which we may consider in the future.

It is worth noting that both examples in Sections 2.4.2 and 2.4.3 confirm the stiffening effect of coarse-graining. This is because the coarse-graining procedure introduces the model error, which arises when the division of the fully-resolved domain and the coarse-grained domain as well as the prescribed interpolation pattern in the coarse-grained domain does not fully represent the actual deformation distribution in the model. The model error can be minimized if the following two conditions are satisfied: (1) the fully-resolved domain is large enough to embrace the localized deformation/failure while the fluctuation caused by the localized de-

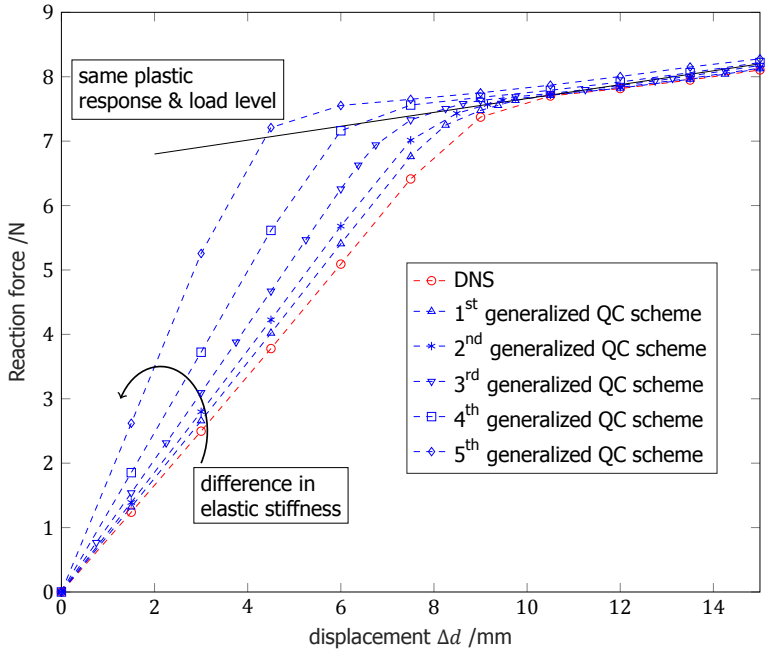

Figure 2.18: Reaction force versus imposed mid-span displacement for the three point bending of the notched BCC lattice.

formation/failure disappears at the borders of the fully-resolved domain and the coarse-grained domain; (2) the interpolation pattern (including the order of interpolation and the layout of the interpolation mesh) in the coarse-grained domain matches the actual deformation distribution in the coarse-grained domain. The larger the model error, the more severe the stiffening effect. For the example in Section 2.4.2, the beam nodes displace relatively uniformly and this can be well captured by the prescribed interpolation pattern. Therefore, the stiffening effect induced by coarse-graining is not a big concern (see Fig. 2.13) for that example.

For the example in Section 2.4.3 however, during the elastic loading stage, the notch inflicts a non-uniform elastic deformation field with a far-reaching fluctuation and this could not be adequately captured by all the five coarse-graining schemes. Therefore, the model error is large and reflects itself through the disparity of the predicted elastic stiffness. When advancing to the elastoplastic loading stage, the load bearing capacity essentially depends on the elastoplastic behavior in the proximity of the notch, which is fully resolved in all the five coarse-graining schemes with the coarse-grained domain progressively subjected to more and more uniform stress states; Hence, the predicted load levels are comparable. The authors will study the stiffening impact of coarse-graining, which in essence reflects the reduction of the model error, in a quantitative manner by resorting to adaptive coarse-graining strategies in the future work, whereas it is only described qualitatively in

the presented work.

2.4.4. Indentation of a BCC lattice

In the last example, we consider the indentation of a BCC lattice, corresponding to a localized full 3D loading of the structure. The failure of a metallic lattice structure under indentation is attributed to the buckling of the struts under the indenter (for small indentation depths). Elastoplasticity is considered and due to the high computational cost of the DNS, only the generalized quasicontinuum model is computed.

The buckling of the struts results in a local collapse of the lattice and does not propagate far from the loading zone.

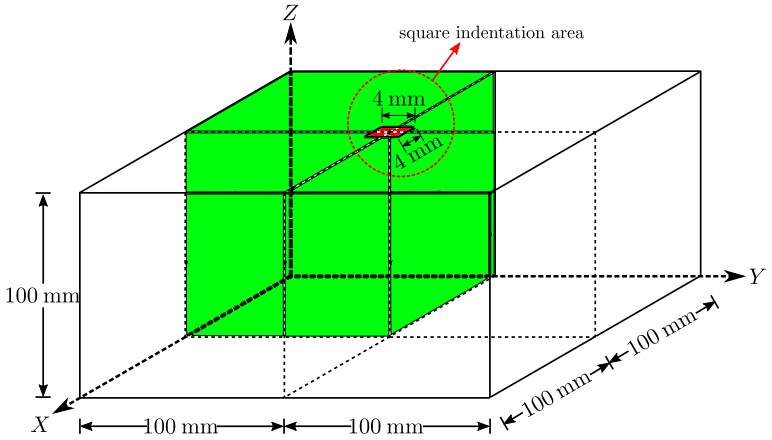

Figure 2.19: Dimensions of the BCC lattice for the simulation of indentation. The indentation is imposed on the red area. Due to symmetry, only a quarter of the lattice is simulated.

The BCC lattice simulated here consists of $50 \times 50 \times 50$ unit cells (Fig. 2.19). Modeling such a large lattice using direct numerical simulation would indeed require significant computational resources (i.e. around 6 millions beam elements and 31.5 millions DoFs). However, this structure can be simulated at a reasonable computational cost using the generalized quasicontinuum method.

A flat punch indentation is modeled by imposing the vertical displacement of a surface area of 2×2 unit cells (Fig. 2.19). A final indentation depth of 0.3 mm is imposed. All of the faces of the lattice except for the top face are constrained from displacement perpendicular to them. The material and geometrical parameters of the lattice are assumed to be the same as earlier. A small fully-resolved domain of $10 \times 10 \times 10$ unit cells is allocated in the proximity of the indenter. The remainder of the lattice is coarse-grained using linear tetrahedral interpolation elements with 5 GQPs (Fig. 2.20). The generalized quasicontinuum model contains 279 090 DoFs and 226 560 sampling beams, yielding a reduction of 99.12% and 96.22% relative to those of DNS.

The reaction force is presented as a function of the indentation depth in Fig. 2.21.

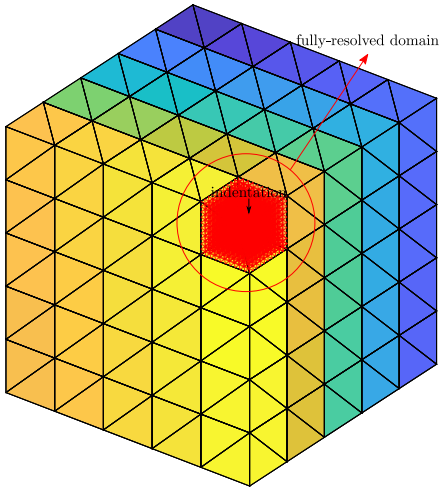

(a) Interpolation scheme: The fully-resolved domain is a cubic region in the vicinity of the indenter, the remaining part of the lattice is coarse-grained.

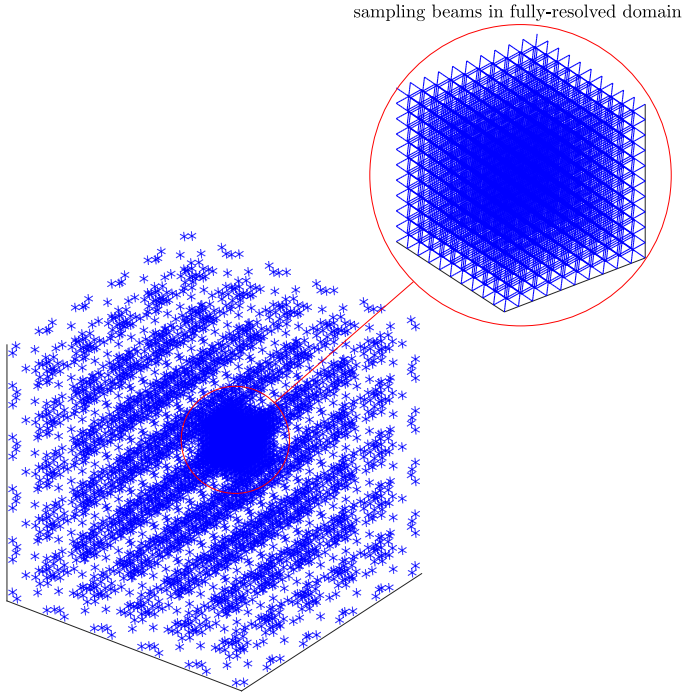

(b) Distribution of sampling beams.

Figure 2.20: The generalized quasicontinuum model of the indentation problem.

The reaction force reaches a peak before it decreases. Observing the deformed

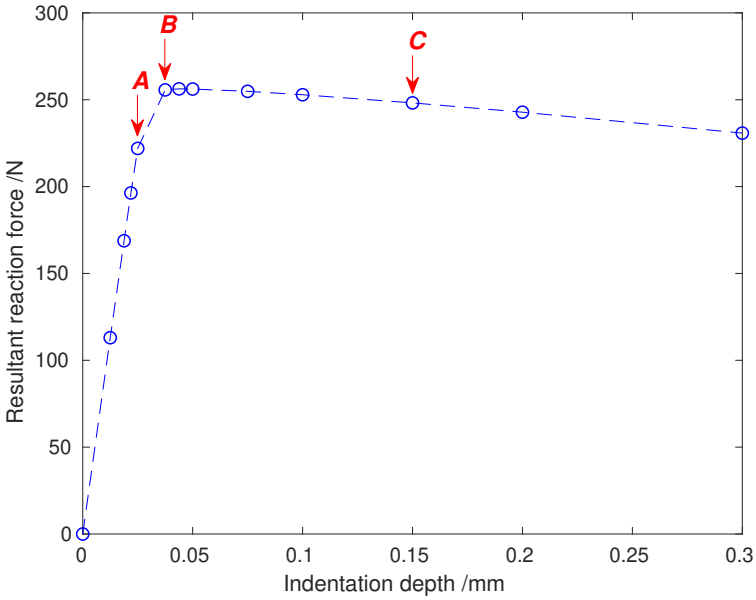

Figure 2.21: Reaction force versus indentation depth for the generalized quasicontinuum modeling of the indentation of the BCC lattice.

shape of the lattice in the vicinity of the indenter (before and after the peak force), the decrease of the reaction forces is caused by the buckling of the struts under the indenter. Three snapshots of the deformed shape of the $2 \times 2 \times 2$ unit cells in the vicinity of the indenter are presented in Fig. 2.22.

In agreement with experimental observations, the initial plasticity induced buckling of the struts would propagate towards adjacent struts, leading to the local collapse of the lattice [59, 60]. In addition to capturing the geometrical nonlinear behavior of the lattice [22], this contribution captures the cross section variability along the strut as well as the plastic behavior (both are observed in experiments [4, 14]).

The generalized quasicontinuum method can achieve significant model reduction and alleviate the computational demand (e.g. 99.12% and 96.22% reduction in the number of DoFs and sampling beams respectively) whilst it is able to capture localization (e.g. the buckling of individual struts and local collapse of the lattice).

2.5. Conclusions

This work presents a generalization of the multi-scale quasicontinuum method, which we have called the generalized quasicontinuum method. In contrast to conventional FE^2-approaches, the method avoids the requirement of scale-separation and is therefore convenient to use in a concurrent manner. It is also as straightforward to implement for higher-order macro-scale FEs as for linear FEs. The downside

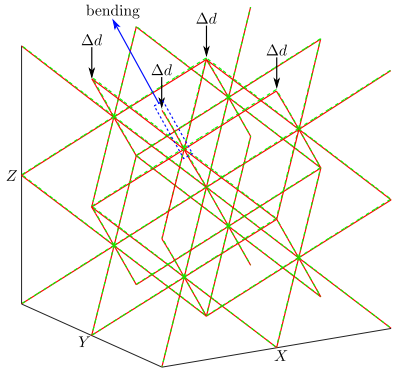

(a) Point A: Beams bend.

Figure 2.22: Local deformation of the lattice in the vicinity of the indenter. Δd denotes the nodes where indentation displacement is applied. The reference shape of the lattice is shown in green dashed line, the deformed shape of the lattice is shown in red solid line. The snapshots correspond to points A, B and C on the force-displacement curve in Fig. 2.21.

is that it is computationally somewhat more costly than computational homogenization approaches.

The method is applied to BCC metallic lattice structures as they can be produced by additive manufacturing. We have shown that the basic fine scale failure modes of the metallic lattice structures (the buckling and the plastic bending of individual struts) are well captured thanks to a 3D co-rotational beam finite element with embedded plastic hinges, which is also presented in this contribution.

If we stick to the quasicontinuum terminology, we have shown that the number of DoFs and the number of sampling beam elements can be drastically decreased using the generalized quasicontinuum method (compared to the direct numerical simulations), whilst maintaining a high accuracy. In case of unconstrained compression of rather small BCC lattice for instance, the generalized quasicontinuum method reduces the number of DoFs by 98.17% and the number of sampling beams by 86.11%. As a consequence, the computational time is reduced by 97.27% while the induced error is only 3.76%, demonstrating a favorable trade-off. We therefore conclude that the generalized quasicontinuum method is a promising framework to efficiently simulate the mechanical behavior of large lattice structures at a high accuracy.

As most nested, concurrent multi-scale approaches, the generalized quasicontinuum method requires smooth deformation fluctuations in the coarse-grained domains. Consequently, fully-resolved domains must be large enough to embrace localization (e.g. due to fracture). The approach is thus computationally most beneficial if the fully resolved domain is small compared to the coarse-grained domain (as is the case for conventional nested, concurrent approaches).

The following points require future work: Dividing metallic lattice structures into

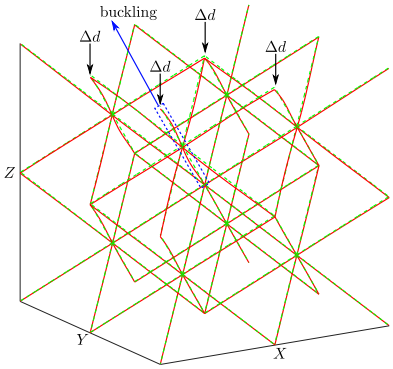

(b) Point B: Buckling appears below the indentation area.

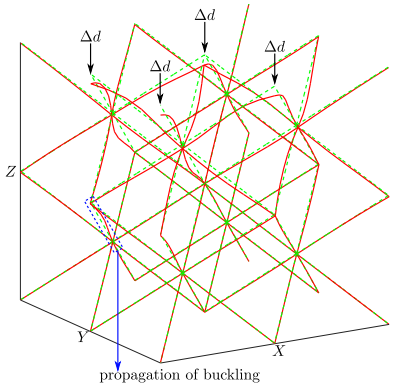

(c) Point C: Buckling propagates and local collapse occurs.

Figure 2.22: Local deformation of the lattice in the vicinity of the indenter. Δd denotes the nodes where indentation displacement is applied. The reference shape of the lattice is shown in green dashed line, the deformed shape of the lattice is shown in red solid line. The snapshots correspond to points A, B and C on the force-displacement curve in Fig. 2.21.

fully-resolved domains and coarse-grained domains at no observable reduction of the accuracy requires information about localization. This information is generally not known a priori. Thus, developing an adaptive coarse-graining strategy would be useful. Classifying the micro-structural nodes of a unit cell into different types needs to be elaborated. The influence of different classification schemes on the computational efficiency and accuracy needs to be investigated. Applying the proposed generalized quasicontinuum method to other types of unit cells can be an extension.

References

[1] L. Chen, L. A. Beex, P. Z. Berke, T. J. Massart, and S. P. Bordas, *Generalized quasicontinuum modeling of metallic lattices with geometrical and material nonlinearity and variability,* Computer Methods in Applied Mechanics and Engineering **366**, 112878 (2020).

[2] M. Rashed, M. Ashraf, R. Mines, and P. Hazell, *Metallic microlattice materials: A current state of the art on manufacturing, mechanical properties and applications,* Materials & Design **95**, 518 (2016).

[3] G. N. Labeas and M. M. Sunaric, *Investigation on the static response and failure process of metallic open lattice cellular structures,* Strain **46**, 195 (2010), https://onlinelibrary.wiley.com/doi/pdf/10.1111/j.1475-1305.2008.00498.x .

[4] H. D. Carlton, J. Lind, M. C. Messner, N. A. Volkoff-Shoemaker, H. S. Barnard, N. R. Barton, and M. Kumar, *Mapping local deformation behavior in single cell metal lattice structures,* Acta Materialia **129**, 239 (2017).

[5] A. K. Noor, M. S. Anderson, and W. H. Greene, *Continuum models for beam and platelike lattice structures,* AIAA Journal **16**, 1219 (1978).

[6] A. K. Noor, *Continuum modeling for repetitive lattice structures,* Applied Mechanics Reviews **41**, 285 (1988).

[7] K. Ushijima, W. J. Cantwell, R. A. W. Mines, S. Tsopanos, and M. Smith, *An investigation into the compressive properties of stainless steel microlattice structures,* Journal of Sandwich Structures & Materials **13**, 303 (2011), https://doi.org/10.1177/1099636210380997 .

[8] R. Gümrük and R. A. W. Mines, *Compressive behaviour of stainless steel micro-lattice structures,* International Journal of Mechanical Sciences **68**, 125 (2013).

[9] P. Li, Z. Wang, N. Petrinic, and C. R. Siviour, *Deformation behaviour of stainless steel microlattice structures by selective laser melting,* Materials Science and Engineering: A **614**, 116 (2014).

[10] P. Li, *Constitutive and failure behaviour in selective laser melted stainless steel for microlattice structures,* Materials Science and Engineering: A **622**, 114 (2015).

[11] H. Cho, Y. Cho, and H. N. Han, *Finite element analysis for mechanical response of Ti foams with regular structure obtained by selective laser melting,* Acta Materialia **97**, 199 (2015).

[12] M. R. Karamooz-Ravari and M. Kadkhodaei, *A computationally efficient modeling approach for predicting mechanical behavior of cellular lattice structures,* Journal of Materials Engineering and Performance **24**, 245 (2015).

[13] M. R. Karamooz-Ravari and M. Kadkhodaei, *Finite element modeling of the elastic modulus of T-6Al-4V scaffold fabricated by SLM,* in *Fifth Biot Conference on Poromechanics*, edited by C. Hellmich, B. Pichler, and D. Adam, Technische Universitat Wein (American Society of Civil Engineers, Reston, Virginia, U.S., 1993) pp. 1021–1028, https://ascelibrary.org/doi/pdf/10.1061/9780784412992.122 .

[14] L. Liu, P. Kamm, F. García-Moreno, J. Banhart, and D. Pasini, *Elastic and failure response of imperfect three-dimensional metallic lattices: the role of geometric defects induced by selective laser melting,* Journal of the Mechanics and Physics of Solids **107**, 160 (2017).

[15] G. Campoli, M. S. Borleffs, S. A. Yavari, R. Wauthle, H. Weinans, and A. A. Zadpoor, *Mechanical properties of open-cell metallic biomaterials manufactured using additive manufacturing,* Materials & Design **49**, 957 (2013).

[16] M. Smith, Z. Guan, and W. J. Cantwell, *Finite element modelling of the compressive response of lattice structures manufactured using the selective laser melting technique,* International Journal of Mechanical Sciences **67**, 28 (2013).

[17] L. A. A. Beex, P. Kerfriden, T. Rabczuk, and S. P. A. Bordas, *Quasicontinuum-based multiscale approaches for plate-like beam lattices experiencing in-plane and out-of-plane deformation,* Computer Methods in Applied Mechanics and Engineering **279**, 348 (2014).

[18] L. A. A. Beex, R. H. J. Peerlings, and M. G. D. Geers, *A multiscale quasicontinuum method for dissipative lattice models and discrete networks,* Journal of the Mechanics and Physics of Solids **64**, 154 (2014).

[19] L. A. A. Beex, R. H. J. Peerlings, and M. G. D. Geers, *Central summation in the quasicontinuum method,* Journal of the Mechanics and Physics of Solids **70**, 242 (2014).

[20] L. A. A. Beex, R. H. J. Peerlings, and M. G. D. Geers, *A multiscale quasicontinuum method for lattice models with bond failure and fiber sliding,* Computer Methods in Applied Mechanics and Engineering **269**, 108 (2014).

[21] D. M. Kochmann and J. S. Amelang, *The quasicontinuum method: Theory and applications,* in *Multiscale Materials Modeling for Nanomechanics*, Vol. 245, edited by C. R. Weinberger and G. J. Tucker (Springer International Publishing, Cham, Switzerland, 2016) Chap. 8, pp. 159–193.

[22] G. P. Phlipot and D. M. Kochmann, *A quasicontinuum theory for the nonlinear mechanical response of general periodic truss lattices,* Journal of the Mechanics and Physics of Solids **124**, 758 (2019).

[23] E. B. Tadmor, R. Phillips, and M. Ortiz, *Mixed atomistic and continuum models of deformation in solids,* Langmuir **12**, 4529 (1996), https://doi.org/10.1021/la9508912 .

[24] E. B. Tadmor, M. Ortiz, and R. Phillips, *Quasicontinuum analysis of defects in solids,* Philosophical Magazine A **73**, 1529 (1996), https://doi.org/10.1080/01418619608243000 .

[25] R. Miller, M. Ortiz, R. Phillips, V. Shenoy, and E. B. Tadmor, *Quasicontinuum models of fracture and plasticity,* Engineering Fracture Mechanics **61**, 427 (1998).

[26] J. Knap and M. Ortiz, *An analysis of the quasicontinuum method,* Journal of the Mechanics and Physics of Solids **49**, 1899 (2001), the JW Hutchinson and JR Rice 60th Anniversary Issue.

[27] M. Luskin, C. Ortner, and B. V. Koten, *Formulation and optimization of the energy-based blended quasicontinuum method,* Computer Methods in Applied Mechanics and Engineering **253**, 160 (2013).

[28] M. Luskin and C. Ortner, *Atomistic-to-continuum coupling,* Acta Numerica **22**, 397 (2013).

[29] M. Luskin and C. Ortner, *An analysis of node-based cluster summation rules in the quasicontinuum method,* SIAM Journal on Numerical Analysis **47**, 3070 (2009), https://doi.org/10.1137/080743391 .

[30] B. Van Koten, X. H. Li, M. Luskin, and C. Ortner, *A computational and theoretical investigation of the accuracy of quasicontinuum methods,* in *Numerical Analysis of Multiscale Problems*, edited by I. G. Graham, T. Y. Hou, O. Lakkis, R. Scheichl, I. G. Graham, T. Y. Hou, O. Lakkis, and R. Scheichl (Springer Berlin Heidelberg, Berlin, Heidelberg, 2012) pp. 67–96.

[31] L. A. A. Beex, R. H. J. Peerlings, K. van Os, and M. G. D. Geers, *The mechanical reliability of an electronic textile investigated using the virtual-power-based quasicontinuum method,* Mechanics of Materials **80**, 52 (2015).

[32] O. Rokoš, L. A. A. Beex, J. Zeman, and R. H. J. Peerlings, *A variational formulation of dissipative quasicontinuum methods,* International Journal of Solids and Structures **102-103**, 214 (2016).

[33] L. A. A. Beex, R. H. J. Peerlings, and M. G. D. Geers, *A quasicontinuum methodology for multiscale analyses of discrete microstructural models,* International Journal for Numerical Methods in Engineering **87**, 701 (2011), https://onlinelibrary.wiley.com/doi/pdf/10.1002/nme.3134 .

[34] L. A. A. Beex, O. Rokoš, J. Zeman, and S. P. A. Bordas, *Higher-order quasicontinuum methods for elastic and dissipative lattice models: uniaxial deformation and pure bending,* GAMM-Mitteilungen **38**, 344 (2015), https://onlinelibrary.wiley.com/doi/pdf/10.1002/gamm.201510018 .

[35] P. Kerfriden, P. Gosselet, S. Adhikari, and S. P. A. Bordas, *Bridging proper orthogonal decomposition methods and augmented newton–krylov algorithms:*

An adaptive model order reduction for highly nonlinear mechanical problems, Computer Methods in Applied Mechanics and Engineering **200**, 850 (2011).

[36] P. Kerfriden, P. Gosselet, S. Adhikari, S. P. A. Bordas, and J. C. Passieux, *POD-based model order reduction for the simulation of strong nonlinear evolutions in structures: Application to damage propagation,* IOP Conference Series: Materials Science and Engineering **10**, 012165 (2010).

[37] P. Kerfriden, K. M. Schmidt, T. Rabczuk, and S. P. A. Bordas, *Statistical extraction of process zones and representative subspaces in fracture of random composites,* International Journal for Multiscale Computational Engineering **11**, 253 (2013).

[38] J. Hale, E. Schenone, D. Baroli, L. A. A. Beex, and S. P. A. Bordas, *A hyper-reduction method using adaptivity to cut the assembly costs of reduced order models,* (2018), unpublished paper.

[39] P. Kerfriden, O. Goury, T. Rabczuk, and S. P. A. Bordas, *A partitioned model order reduction approach to rationalise computational expenses in nonlinear fracture mechanics,* Computer Methods in Applied Mechanics and Engineering **256**, 169 (2013).

[40] K. S. Sunder and R. A. Cookson, *Integration points for triangles and tetrahedrons obtained from the Gaussian quadrature points for a line,* Computers & Structures **21**, 881 (1985).

[41] J. M. Battini and C. Pacoste, *Plastic instability of beam structures using co-rotational elements,* Computer Methods in Applied Mechanics and Engineering **191**, 5811 (2002).

[42] P. F. Chen and G. H. Powell, *Generalized plastic hinge concepts for 3D beam-column elements,* NASA STI/Recon Technical Report N **84** (1982).

[43] C. C. Rankin and B. Nour-Omid, *The use of projectors to improve finite element performance,* in *Computational Structural Mechanics & Fluid Dynamics*, edited by A. K. Noor and D. L. Dwoyer (Pergamon, Oxford, 1988) pp. 257 – 267.

[44] B. Nour-Omid and C. C. Rankin, *Finite rotation analysis and consistent linearization using projectors,* Computer Methods in Applied Mechanics and Engineering **93**, 353 (1991).

[45] J. M. Battini and C. Pacoste, *Co-rotational beam elements with warping effects in instability problems,* Computer Methods in Applied Mechanics and Engineering **191**, 1755 (2002).

[46] H. P. Bui, S. Tomar, H. Courtecuisse, M. Audette, S. Cotin, and S. P. A. Bordas, *Controlling the error on target motion through real-time mesh adaptation: Applications to deep brain stimulation,* International Journal for Numerical Methods in Biomedical Engineering **34**, e2958 (2018), https://onlinelibrary.wiley.com/doi/pdf/10.1002/cnm.2958 .

[47] H. P. Bui, S. Tomar, and S. P. A. Bordas, *Corotational cut finite element method for real-time surgical simulation: Application to needle insertion simulation,* Computer Methods in Applied Mechanics and Engineering **345**, 183 (2019).

[48] G. H. Powell and P. F. Chen, *3D beam–column element with generalized plastic hinges,* Journal of Engineering Mechanics **112**, 627 (1986).

[49] J. M. Battini, *Co-rotational beam elements in instability problems*, Ph.D. thesis, KTH, Structural Engineering (2002).

[50] J. Argyris, *An excursion into large rotations,* Computer Methods in Applied Mechanics and Engineering **32**, 85 (1982).

[51] C. A. Felippa, *A systematic approach to the element-independent corotational dynamics of finite elements*, Report (Center for Aerospace Structures, College of Engineering & Applied Science University of Colorado Boulder Search, 2000).

[52] S. Ahmadi, G. Campoli, S. Amin Yavari, B. Sajadi, R. Wauthle, J. Schrooten, H. Weinans, and A. Zadpoor, *Mechanical behavior of regular open-cell porous biomaterials made of diamond lattice unit cells,* Journal of the Mechanical Behavior of Biomedical Materials **34**, 106 (2014).

[53] Z. Mróz, *On the description of anisotropic workhardening,* Journal of the Mechanics and Physics of Solids **15**, 163 (1967).

[54] Y. Jiang and H. Sehitoglu, *Comments on the Mroz multiple surface type plasticity models,* International Journal of Solids and Structures **33**, 1053 (1996).

[55] M. A. Meggiolaro, J. T. P. Castro, and H. Wu, *On the applicability of multisurface, two-surface and non-linear kinematic hardening models in multiaxial fatigue,* Frattura ed Integrità Strutturale **9**, 357 (2015).

[56] F. J. Montáns and M. A. Caminero, *On the consistency of nested surfaces models and their kinematic hardening rules,* International Journal of Solids and Structures **44**, 5027 (2007).

[57] R. Gümrük, R. A. W. Mines, and S. Karadeniz, *Static mechanical behaviours of stainless steel micro-lattice structures under different loading conditions,* Materials Science and Engineering: A **586**, 392 (2013).

[58] P. R. Budarapu, R. Gracie, S. P. A. Bordas, and T. Rabczuk, *An adaptive multiscale method for quasi-static crack growth,* Computational Mechanics **53**, 1129 (2014).

[59] Y. Shi, F. Zhang, K. Nan, X. Wang, J. Wang, Y. Zhang, Y. Zhang, H. Luan, K. Hwang, Y. Huang, J. A. Rogers, and Y. Zhang, *Plasticity-induced origami for assembly of three dimensional metallic structures guided by compressive buckling,* Extreme Mechanics Letters **11**, 105 (2017).

[60] G. J. McShane, S. M. Pingle, V. S. Deshpande, and N. A. Fleck, *Dynamic buckling of an inclined strut,* International Journal of Solids and Structures **49**, 2830 (2012), proceedings of International Union of Theoretical and Applied Mechanics Symposium.

3

A refinement indicator for adaptive computations of conventional and generalized quasicontinuum frameworks*

The quasicontinuum method is a concurrent multi-scale approach in which lattice models are fully resolved in small regions of interest and coarse-grained elsewhere. Since the method was originally proposed to accelerate atomistic lattice simulations, its refinement criteria – that drive refining coarse-grained regions and/or increasing fully resolved regions–are generally associated with quantities relevant to the atomistic scale. In this contribution, a new and general refinement indicator is presented, based on the energies of dedicated unit cells at coarse-grained domain surfaces. This indicator is incorporated in an adaptive scheme of a generalization of the quasicontinuum method able to consider periodic representative volume elements, like the ones employed in most computational homogenization approaches. However, this indicator can also be used for conventional quasicontinuum frameworks. Illustrative numerical examples of elastic indentation and scratch of different lattices demonstrate the capabilities of the refinement indicator and its impact on adaptive quasicontinuum simulations.

* Submitted to International Journal for Numerical Methods in Engineering on May 12, 2020.

3.1. Introduction

The quasicontinuum (QC) method is a concurrent multi-scale approach that aims to decrease the computational costs of meso-structural, micro-structural or nano-structural lattice models. The approach fully resolves the lattice model in small regions of interest (fully-resolved domains: FRDs), whereas in the remainder of the domain the degrees of freedom (DoFs) of the lattice model are interpolated (coarse-grained domains: CGDs). The CGDs are subdivided into non-overlapping interpolation elements (IPEs), inside each of which the shape functions of finite elements are used to interpolate the DoFs. As the interpolation decreases the number of DoFs, the efforts to *solve* the governing equations are significantly reduced. A second reduction step, often called summation or sampling, is necessary to decrease the efforts to *construct* the governing equations. Summation in QC terminology means that only a few lattice interactions are sampled to approximate the contributions of all lattice interactions in the CGDs to the governing equations.

The QC method was originally proposed to decrease the computational expenses of atomistic lattices simulation – characterized by conservative interactions [1–11]. Later, it was reformulated by Beex et al. [12–14] using a virtual-power-statement to incorporate dissipative phenomena. Rokoš et al. [15–17] have subsequently demonstrated that dissipation can also be incorporated using variational statements. These reformulations have widened the method's applicability to lattice models of discrete and fibrous materials in which each yarn, fiber or strut is represented using a series of consecutive springs or beams.

Another enhancement was recently proposed by Mikeš et al.[18–21], who have made the approach applicable to geometrically irregular lattices – albeit the mechanical behaviour of each interaction is the same. A disadvantage of this approach is that summation cannot truly be exploited to decrease the construction of the governing equations because each interaction is evaluated to get a homogenized material tensor. The approach was recently used by Ghareeb and Elbanna [22] to investigate networks of polymer chains.

Traditionally, the interpolation in the CGDs is performed indiscriminately: the DoFs of all lattice nodes are interpolated in the same manner – without regarding the connectivity pattern of the lattice. Consequently, the QC method is traditionally only exploited for regular lattices, where each lattice node is connected to its neighbouring lattice nodes in the same manner.

Recently however, Chen et al. [23] and Phlipot and Kochmann [24] have proposed generalization in which a more complex connectivity of the lattice is considered. As a result, the method can also be applied to more complex lattice models, in which each lattice node inside a periodic unit cell is connected to its neighboring nodes in different patterns – using interactions of which the mechanical response can vary. Consequently, this particular QC framework can be used for any type of micro-structural model, as long as its micro-structural arrangement is periodic.

The generalization are based on interpolating the DoFs of each lattice node in a periodic unit cell (i.e. the repeating geometrically similar units in a periodic lattice) individually. Thus, a disadvantage of the generalization is that many more DoFs remain – relative to the macro-models of computational homogenization (FE^2) ap-

proaches [25–28]. Another disadvantage is that more unit cells must be sampled inside each IPE. Advantages over nested approaches based on computational homogenization are that: (i) macro-to-micro and micro-to-macro relations are avoided, (ii) no micro-structural boundary conditions are necessary, and (iii) scale-separation does not need to hold.

It is worth explaining the necessity of incorporating adaptivity to QC for metallic periodic lattices. The deformation of metallic lattices features, among others, buckling and plastic hinge appearance (in case of ductile material). These occur locally on the strut level before propagating wider into the lattice. Therefore, computational savings are improved if the initial FRD can evolve in order to encapsulate the local deformation which changes location during a simulation. A measure for localized behavior is a high local deformation gradient. The fundamental idea of the refinement indicator presented in this work is to monitor the discrepancy of the strain energy at newly introduced 'signaling unit cells' placed at interfaces of interest. If it exceeds a user-defined threshold, either the local interpolation elements are refined, or they are fully resolved to increase the local kinematic richness. Evolving FRDs will then be able to reproduce strut buckling and the formation of plastic hinges at different locations in the model domain. Therefore, the main goal of the presented work is to develop an adaptive scheme that avoids unnecessary refinement due to rigid body deformations and assess its performance. Because of this focus, only elastic co-rotational beam FEs are employed in this chapter.

Adaptivity of QC approaches is mainly investigated in the context of atomistic lattices for metals [3, 18, 29–31]. For this reason, most of the refinement indicators are based on quantities that are relevant for regular atomistic lattices and metals [3, 18, 30, 31]. For instance, Phlipot and Kochmann [24] have used a refinement indicator based on the (continuum derived) J_2 invariant of the deformation, even though their meso-structural lattice represents a discrete multi-lattice [32]. A disadvantage of this indicator is that refinement may also be triggered for homogeneous deformations and rigid body rotations.

To the best of the authors' knowledge, only three studies have presented truly different refinement indicators for QC methods. First, Memarnahavandi et al. [29] have presented a goal-oriented adaptive QC approach in which not only the triangulation of IPEs (triangular shapes and corresponding finite element shape functions are used to interpolate the DoFs) was adapted, but also the size of the clusters of summation/sampling interactions. The disadvantage of this approach is that the cluster QC method is known to be relatively inaccurate [12–14, 17, 33, 33–36], even if many sampling interactions are used.

Second, Rokoš et al. [16, 17] have presented adaptive QC formulations for damageable lattices, where the evolution of FRDs and CGDs was triggered by the development of damage in the lattice interactions. This indicator thus is only applicable to damageable lattices, and such a approach thus only triggers refinement in regions where damage occurs, whereas refinement in other regions may also improve the accuracy for complex stress distributions – regardless of the occurrence of damage.

Third, Mikeš et al. [18] have formulated adaptivity based on the Zienkiewicz-

Zhu indicator. The resulting adaptive scheme appears to be generally applicable and does not suffer from any of the drawbacks. A disadvantage for its use in the generalized variant of the QC method, which effectively superimposes as many finite element shape functions as classes of lattice nodes present in the lattice, is that no macroscopic deformation gradient can be recognized. One possibility would therefore be to combine the Zienkiewicz-Zhu indicator of Mikeš et al. [18] with the approach of Phlipot and Kochmann [24] in which as many macro-scale deformation gradient tensors are distinguished as classes of lattice nodes are present.

Instead, the present contribution proposes a completely different, yet entirely general refinement indicator that can be applied to both conventional QC methods as well as to its generalized variant (although we only demonstrate its use for the generalized variant here). The need for refinement is indicated by placing a 'signaling' unit cell on each communicating IPE surface, and by determining two stored energies for each signaling unit cell: first by governing the signaling unit cell deformation according to the first IPE, and second by governing the signaling unit cell deformation according to the second IPE (i.e. the neighboring IPE that shares the same external surface). If the difference between the signaling unit cell energies reaches a user-defined threshold, both IPEs are refined. At the periphery of the FRDs, some additional technicalities must be incorporated, but the approach effectively remains the same.

If the volume of a newly created IPE reaches a user-defined minimum, it will be replaced by an FRD. This automatically increases the size of FRDs, but also enables FRDs to be created independently out of a cluster of IPEs (as the illustration results will reveal).

As mentioned before, the resulting adaptive scheme is demonstrated here for the generalized QC method, but because conventional QC methods are a subset of the generalized QC framework, the refinement indicator is also applicable for conventional QC approaches. The indicator's capabilities are demonstrated for 3D structures consisting of body-centered-cubic (BCC) and Kelvin unit cells of elastic, geometrically non-linear co-rotational beams. Within the unit cell, each strut is discretized with several beam elements, which are given independent geometrical and material parameters.

The remainder of this work is organized as follows. Section 3.2 outlines the generalized QC method. Section 3.3 presents the adaptive scheme including the detailed implementation of the refinement indicator. Section 3.4 illustrates the adaptive generalized QC method using numerical examples. Section 3.5 concludes the presented work.

3.2. Generalized QC method

For demonstration purposes, we explain the generalized QC method for the periodic unit cell in Fig. 3.1. However, it is emphasized that the approach is applicable to any type of unit cell, as long as it is periodic.

For the sake of a simple illustration let us consider the structural lattice of Fig. 3.2, which consists of an X shaped 2D unit cell of Fig. 3.1. The unit cell of Fig. 3.1 consists of four diagonal struts. Each strut is represented by a series of

three beam elements. Each central beam element is given different geometrical and material parameters than the outer ones – as presented by the cyan and green colors. Beam finite elements [37] are used as structural models in the computation.

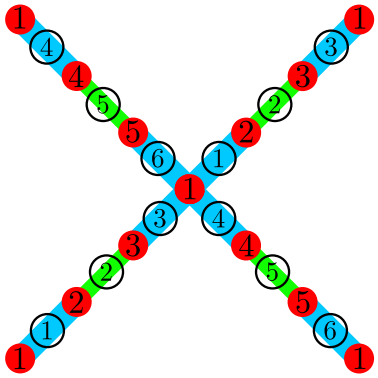

Figure 3.1: Beam representation of an X shaped 2D unit cell. All cyan beams are given the same geometrical and material parameters and the green beams are given their own geometrical and material parameters. Beam node (•) types are indicated as $1-5$. Beam types are indicated as ① – ⑥.

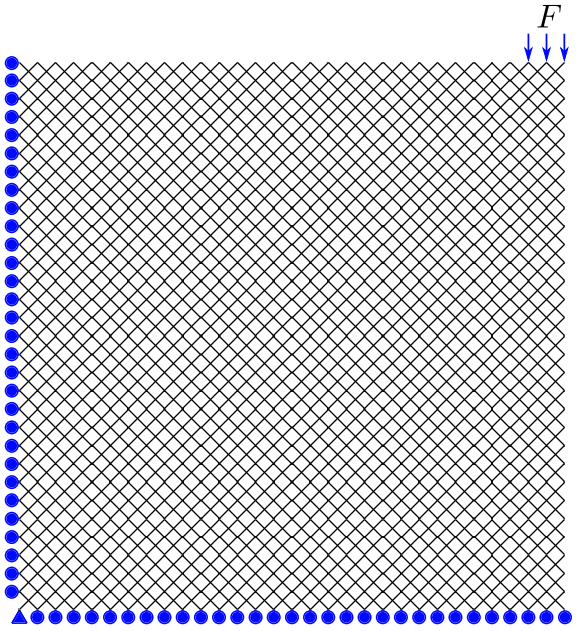

Figure 3.2: Two dimensional sketch of a large system of X-shaped unit cells.

We are interested in systems of large numbers of unit cells, because those

typically appear in engineering applications. However, they are computationally demanding because of the large number of DoFs.

As we restrict ourselves to (non-linear) elastic systems, the system can be *solved* by minimizing a total potential energy according to:

$$\mathbf{u}^* = \underset{\mathbf{u}}{\operatorname{argmin}} \left(-\mathbf{f}_{\text{ext}}^T \mathbf{u} + \sum_{i=1}^{m} \mathbf{E}_i(\mathbf{u}) \right). \tag{3.1}$$

In Eq. (3.1), $\mathbf{u}$ and $\mathbf{f}_{\text{ext}}$ denote the column matrices of the beam nodes *DoFs* and *external forces* (including moments), respectively. $\mathbf{E}_i(\mathbf{u})$ denotes the elastic strain energy of beam i and m denotes the total number of beam elements. Eq. (3.1) is referred to as the direct numerical simulation (DNS).

QC methods were proposed in order to decrease the computational costs of DNS, while keeping a reasonable accuracy. The method incorporates two model reduction steps: *interpolation* and *summation*.

3.2.1. Interpolation in the generalized QC method

The *interpolation* step of the generalized QC method divides the system into non-overlapping fully resolved domains (FRDs) and coarse-grained domains (CGDs).

In the FRDs, the micro-structural beam representation is preserved. This implies that high fluctuations of the DoFs can be described in FRDs at a high computational cost. Therefore, FRDs are typically restricted to small sub-domains in which localized responses occur (e.g. strain localization and beam failures).

On the other hand, CGDs are employed in the remainder of the model domain in which the deformation fluctuations are substantially less local. The CGDs are further divided into interpolation elements (IPEs) to apply an interpolation of kinematics within each IPE. (although any type of interpolation technique may of course be used, see e.g. [38]). The DoFs of all beam nodes in the IPEs are interpolated using FE shape functions and the representative DoFs defined at the nodes of the IPEs (same number and nature of DoFs as for a single beam node for each beam type convoluted in an IPE nodal vector). When the FRD-CGD interface cuts through the lattice, there are beams that are sectioned by the interface (or one beam end lies exactly on the interface). As for beams with one of the beam ends in the CGD and the other end in the FRD, the DoFs of the beam end in the FRD are preserved while the DoFs of the beam end in the CGD are interpolated.

Fig. 3.3 illustrates a possible interpolation scheme for the system of Fig. 3.2. Since deformation localization will appear near the concentrated force, the region near the location of the external force is fully resolved. The remainder of the system which may be exempt from deformation localization (i.e. smooth strain gradients) is designated as coarse grained domains (CGDs). In Fig. 3.3 triangular patches are used to create the IPEs and linear triangular finite element shape functions are used to interpolate the DoFs of the underlying beam nodes.

As a result of *interpolation*, only the DoFs of the beam nodes in the FRDs and of the *nodes of the IPEs* are preserved in the governing equations. This leads to a reduced set of DoFs (denoted as $\mathbf{u}_r$) and decreases the number of governing

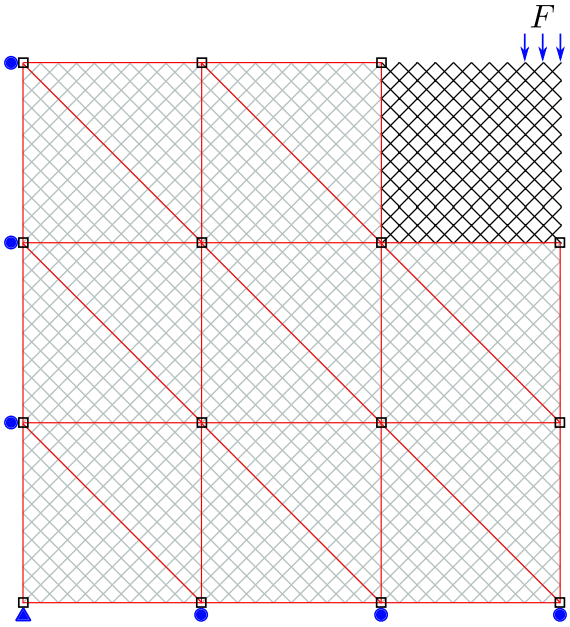

Figure 3.3: Illustration of interpolation in QC methods. □ denote the nodes of the IPEs.

equations and hence, the number of DoFs to solve for. $\mathbf{u}_\mathrm{r}$ is related to the DoFs of all beam nodes, $\mathbf{u}$, using condensation matrix $\mathbf{N}$, i.e.

$$\mathbf{u} = \mathbf{N}\mathbf{u}_\mathrm{r}. \tag{3.2}$$

In the condensation matrix $\mathbf{N}$, each row is associated with the DoF of a beam node in the DNS model and, each column is associated with the DoFs of either the beam nodes in the FRDs or the nodes of the IPEs in the interpolated model. The sub-blocks of $\mathbf{N}$ that are associated with the DoFs of the beam nodes in the FRDs are identity matrices. The sub-blocks of $\mathbf{N}$ that are associated with the DoFs of the nodes of the IPEs contain the finite element shape function evaluations.

Consequently, the minimization problem of Eq. (3.1) is revised as

$$\mathbf{u}_\mathrm{r}^* = \underset{\mathbf{u}_\mathrm{r}}{\operatorname{argmin}} \left(-\mathbf{f}_\mathrm{ext}^T \mathbf{N}\mathbf{u}_\mathrm{r} + \sum_{i=1}^{m} \mathbf{E}_i(\mathbf{N}\mathbf{u}_\mathrm{r}) \right). \tag{3.3}$$

Essential to realize is that the beam nodes in the unit cell of Fig. 3.1 are connected to their neighboring beam nodes in different ways. As a distinctive character, the *generalized* QC method [23] classifies the beam nodes of a unit cell into different types – based on their connectivity. The DoFs of each type of beam node are interpolated independently. To facilitate this, the nodes of the IPEs store multiple

sets of DoFs – one set per type of beam node. These are used to independently interpolate the DoFs of the corresponding type of beam nodes.

For the unit cell of Fig. 3.1 for instance, a total of 13 beam nodes and 12 beam elements are present. After incorporating the orientations of the struts and the type of beam element ('cyan' or 'green') along each strut, 5 different types of beam nodes are classified. Moreover, differentiated by the beam node types of both ends, the 12 beam elements are subdivided in 6 types. The beam type classification will play a role in the adaptivity scheme of Section 3.3.

Interpolation decreases the number of governing equations to solve for. Consequently, interpolation decreases the computational efforts to *solve* the governing equations. However, the computational costs to *construct* the governing equations remains unaffected by interpolation: still all m beams of the system need to be visited (cf. Eq. (3.1) and (3.3)). Even worse is that if the (interpolated) minimization problem of Eq. (3.3) is solved using Newton's method, the condition number of the stiffness matrix of the interpolated system is worse than the condition number of the stiffness matrix of the DNS [39]. Hence, interpolation alone may actually increase the computational time.

3.2.2. Summation in the generalized QC method

The *summation* step of the QC methods aims to reduce the cost of the *construction* of the governing equations, by approximating the governing equations using much less beam elements. The few beam finite elements that remain in the system are used to sample the contributions of all beams to the governing equations. For this reason we refer to the remaining beams as *sampling beams*. Each sampling beam is associated with a weight factor, which measures the number of beams it represents.

After *summation*, the minimization problem of Eq. (3.3) is revised as

$$\mathbf{u}_\mathrm{r}^* = \underset{\mathbf{u}_\mathrm{r}}{\operatorname{argmin}} \left(-\mathbf{f}_\mathrm{ext}^T \mathbf{N}\mathbf{u}_\mathrm{r} + \sum_{i \in S} \omega_i \mathbf{E}_i(\mathbf{N}\mathbf{u}_\mathrm{r}) \right) \tag{3.4}$$

where S denotes the set of sampling beams and ω_i denotes the weight factor of sampling beam i.

The selection of the sampling beams (including the determination of the weight factors) is governed by a *summation rule*. The summation rule proposed by Chen et al.[23] is used here and can be summarized as follows.

First, all beam elements that are either partially or completely inside FRDs are selected as *sampling beams*. Their weight factors are set to 1, since they only represent themselves. Since it is possible that the FRD-CGD interface cuts through the lattice, there are beams that are sectioned and these beams are by definition sampling beams of FRDs.

Second, in CGDs, a sufficient number of Gauss quadrature points (GQPs) are selected inside each IPE. A unit cell is centered at each GQP (which entails that the center of the unit cell does not necessarily match a center of a unit cell of the

underlying system). The beam elements of these unit cells are also selected as sampling beams. The weight factors of these sampling beams are determined as

$$\omega = \mathrm{W}_{\mathrm{GQP}}^{j} \cdot \frac{V_{\mathrm{IPE}}}{V_{\mathrm{UC}}}, \qquad \text{with} \sum_{j=1}^{n_{\mathrm{GQP}}} \mathrm{W}_{\mathrm{GQP}}^{j} = 1, \tag{3.5}$$

where V_{IPE} and V_{UC} denote the volume of the IPE and the volume of a single unit cell, respectively. $\mathrm{W}_{\mathrm{GQP}}^{j}$ denotes the normalized weight of Gauss quadrature point (GQP) j and n_{GQP} denotes the number of GQPs.

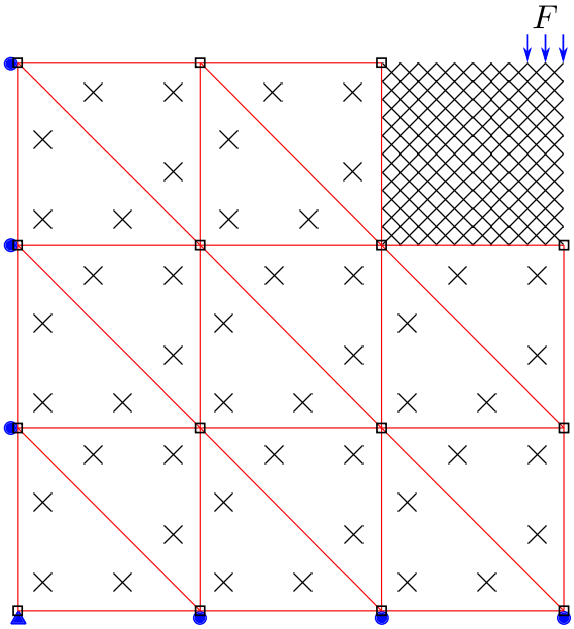

Figure 3.4: Illustration of summation in the generalized QC method. □ denote the nodes of the IPEs.

An illustration of *summation* is presented in Fig. 3.4, where three GQPs are used per IPE. Note that the sufficient number of GQPs refers to the minimum number of GQPs to guarantee convergence.

3.3. Adaptive scheme

This section presents the novel adaptive scheme, including the proposed refinement indicator. The adaptive scheme can be used for both conventional as well as generalized QC frameworks.

The adaptive scheme is proposed in this contribution to achieve *refinement*, coarsening being part of future work. Refinement involves both the refinement of IPEs into smaller IPEs and the transformation of IPEs into FRDs. Consequently, it

hinges on the following: (1) the discretization of IPEs is automatically adjusted, (2) the size of FRDs is automatically increased, and (3) FRDs are automatically created.

3.3.1. Refinement indicator

In this section, a new refinement indicator is proposed. The indicator quantifies energy discrepancies at the surfaces of IPEs (IPE edges in 2D) and it is specified for two situations. In the first situation, the *energy discrepancy* is measured for the interface between two adjacent IPEs. Such an interface is termed as an *IPE-IPE interface*. In the second situation, the *energy discrepancy* is measured for the interface between an IPE and a neighboring FRD. This type of interface is termed as an *IPE-FRD interface*.

At each IPE-IPE interface, a unit cell is placed at the center of the interface (see Fig. 3.5a for 2D illustration), referred to as signaling unit cell. This unit cell does not contribute to the governing equations (i.e. its beams are not sampling beams), it is merely used to decide whether the two IPEs need to be refined or not.

The DoFs of the beams in a signaling unit cell are first assumed to be completely governed by the first IPE (this involves interpolation as well as extrapolation because part of the signaling unit cell is inevitably outside the governing IPE (see Fig. 3.5a)) and its stored energy, E_1, is determined. Second, the DoFs of the beam nodes in the signaling unit cell are interpolated/extrapolated according to the second IPE. Its stored energy, E_2, is again quantified and the following measure for energy discrepancy is then computed:

$$\kappa = \frac{|E_1 - E_2|}{\frac{1}{2}(E_1 + E_2)}. \tag{3.6}$$

In the ideal theoretical case there would be no energy discrepancy.

For each IPE-FRD interface, a signaling unit cell is also centered at the interface (see Fig. 3.5b). The DoFs of the signaling unit cell's beam nodes are now only governed by a single IPE. Accordingly, the energy stored in each beam of the unit cell is computed. Meanwhile, due to the summation rule (Section 3.2.2), there are numerous *sampling beams of FRD*, which intersect the IPE-FRD interface and/or touch the IPE-FRD interface (i.e. their beam nodes are located on the interface).

Of each FRD beam intersecting (and touching) the IPE-FRD interface, the beam type is determined according to the beam type classification. Then, the average stored energy of each beam type is calculated according to Table 3.1. Let $\bar{E}_{\text{uc}}$ and $\bar{E}_{\text{int}}$ be the average beam energy for a certain type of beam. $\bar{E}_{\text{uc}}$ is obtained by averaging the energies of the corresponding type of beams in the signaling unit cell. $\bar{E}_{\text{int}}$ is obtained by averaging the energies of the corresponding type of beams among the aforementioned sampling beams of FRD. The energy discrepancy is first evaluated according to Eq. (3.6) for each type of beam element that exists among the *intersecting/touching sampling beams of FRDs*. Subsequently, all energy discrepancies (κ^i in Table 3.1) are averaged. This averaged energy discrepancy is used to indicate whether or not refinement is required.

In summary, refinement takes place:

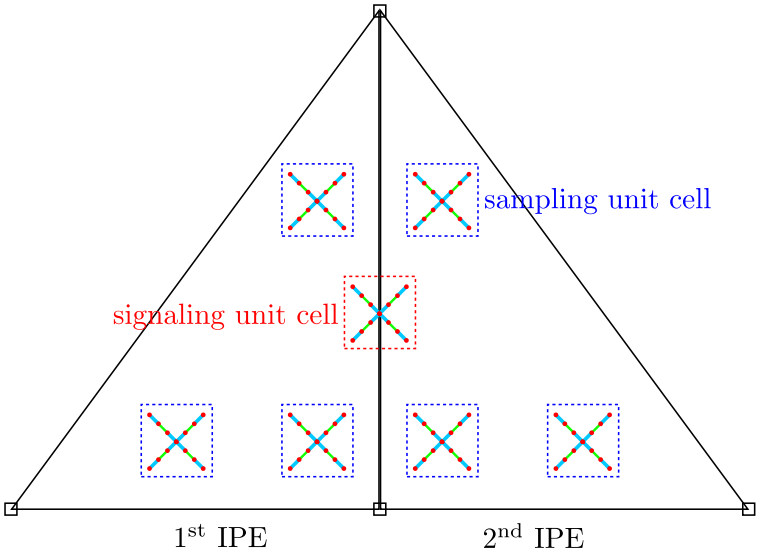

(a) IPE-IPE interface.

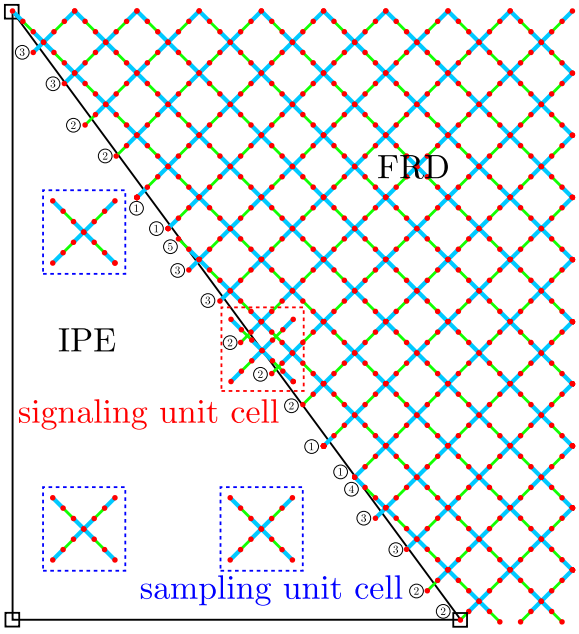

(b) IPE-FRD interface.

Figure 3.5: The scenarios in which the energy discrepancy is measured to drive IPE refinement. □ denote the nodes of the CGDs.

Beam type	Averaged beam strain energy		Energy discrepancy
	From the unit cell that is centered on IPE-FRD interface	From the sampling beams with $\omega = 1$ that cross IPE-FRD interface	
1	$\bar{E}^1_{\text{uc}} = \frac{1}{n^1_{\text{uc}}} \sum_{j=1}^{n^1_{\text{uc}}} E^1_j$	$\bar{E}^1_{\text{int}} = \frac{1}{n^1_{\text{int}}} \sum_{j=1}^{n^1_{\text{int}}} E^1_j$	$\kappa^1 = \frac{\lvert \bar{E}^1_{\text{uc}} - \bar{E}^1_{\text{int}} \rvert}{\frac{1}{2}(\bar{E}^1_{\text{uc}} + \bar{E}^1_{\text{int}})}$
2	$\bar{E}^2_{\text{uc}} = \frac{1}{n^2_{\text{uc}}} \sum_{j=1}^{n^2_{\text{uc}}} E^2_j$	$\bar{E}^2_{\text{int}} = \frac{1}{n^2_{\text{int}}} \sum_{j=1}^{n^2_{\text{int}}} E^1_j$	$\kappa^2 = \frac{\lvert \bar{E}^2_{\text{uc}} - \bar{E}^2_{\text{int}} \rvert}{\frac{1}{2}(\bar{E}^2_{\text{uc}} + \bar{E}^2_{\text{int}})}$
…	…	…	…
i	$\bar{E}^i_{\text{uc}} = \frac{1}{n^i_{\text{uc}}} \sum_{j=1}^{n^i_{\text{uc}}} E^i_j$	$\bar{E}^i_{\text{int}} = \frac{1}{n^i_{\text{int}}} \sum_{j=1}^{n^i_{\text{int}}} E^i_j$	$\kappa^i = \frac{\lvert \bar{E}^i_{\text{uc}} - \bar{E}^i_{\text{int}} \rvert}{\frac{1}{2}(\bar{E}^i_{\text{uc}} + \bar{E}^i_{\text{int}})}$
…	…	…	…
Average	–	–	$\kappa = \frac{1}{b} \sum_{i=1}^{b} \kappa^i$

Table 3.1: Determination of energy discrepancy for a IPE-FRD interface. E^i denotes the strain energy of a type i beam element. n^i_{uc} and n^i_{int} denote the numbers of type i beam elements in the signaling unit cell and among the intersecting (and touching) FRD sampling beams, respectively. b denotes the number of different beam types.

- If $\kappa > \kappa_{\text{tol}}$ for a IPE-IPE interface, both IPEs are refined. If the volume of a newly created IPE is below the threshold V_{tol}, the newly created IPE is transformed into an FRD.
- If $\kappa > \kappa_{\text{tol}}$ for a IPE-FRD interface, the relevant IPE is fully resolved.

3.3.2. Refinement of the spatial discretization

Once the refinement criterion identifies which IPEs need refinement, a refinement algorithm governs *how* the IPEs will be refined or transformed into FRDs. It must be noted that we want to avoid 'hanging' IPE nodes (see Fig. 3.6). Usually with a conforming discretization the IPE nodes are shared with their other neighboring IPEs, but the central IPE node does not belong to the bottom IPE. We call this IPE node a hanging IPE node.

The refinement algorithm obviously depends on the type of IPE kinematics and the used finite element shape functions. Different IPE orders are employed in QC frameworks: first and higher order triangular finite element shape functions in 2D [17, 18, 29, 30, 34–36] and linear tetrahedral and hexahedral shape functions in 3D [17, 23, 24]. A *linear tetrahedral interpolation* is used in this work for the 3D IPEs and the refinement algorithm is an extension of the one proposed by Suárez et al. [40]. The additional originality compared to [40] is that if the volume of a newly created IPE is below V_{tol}, the newly created IPE becomes an FRD. The pseudo code

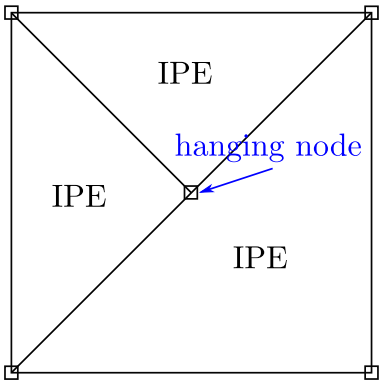

Figure 3.6: Illustration of hanging IPE node. □ denote the nodes of the IPEs.

of the refinement algorithm is detailed in Alg. 1.

Algorithm 1: Refinement algorithm

Input: τ – Tet(tetrahedral) IPEs before refinement
Input: τ_r – Tet IPE(s) to be refined
Output: τ – Tet IPEs after refinement

```
for each tet t ∈ τ_r do
    Divide t into two tets from the midpoint of the longest edge of t;
    Update τ;
Identify hanging IPE nodes in τ and collect them in set L;
while L ≠ ∅ do
    Let p be a hanging node in set L;
    Let e be the edge on which p is located;
    Let M be the set of tets that share edge e (excluding the tets that have
      resulted in the creation of p);
    for each tet t ∈ M do
        Divide t into two tets from the midpoint of the longest edge of t;
        Update τ;
    Identify hanging nodes in τ and collect them in set L;
for each tet t ∈ τ do
    Let V_t be the volume of t;
    if V_t < V_tol then
        Transform t into FRD;
```

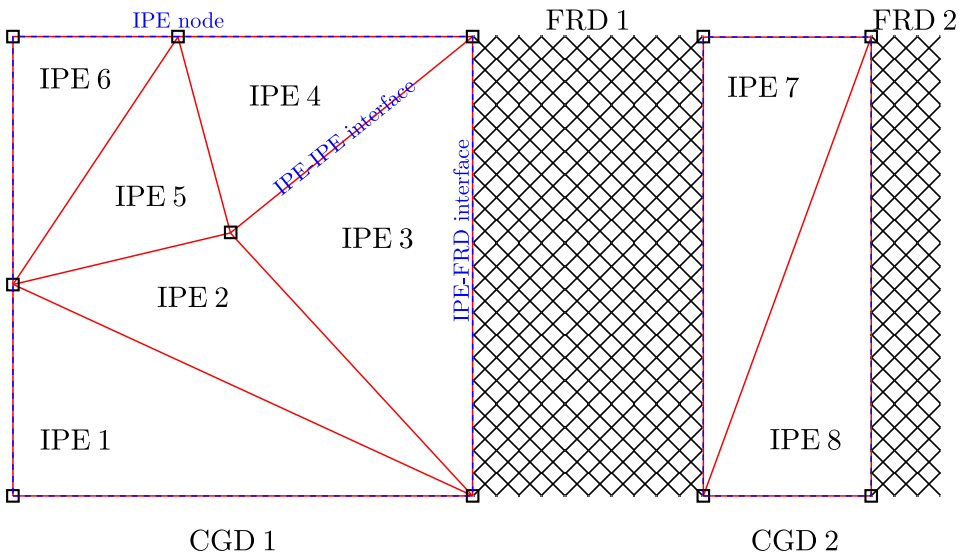

Figure 3.7: Illustration of key concepts of the adaptive QC method. Inside each IPE, kinematic interpolation using FE shape functions is performed.

Symbol	Description
t_k	The kth time step in a Newton scheme.
Ω_k^{FRD}	The FRDs at t_k.
$\partial\Omega_k^{FRD}$	The boundary of the FRDs at t_k.
Ω_k^{CGD}	The CGDs at t_k.
$\partial\Omega_k^{CGD}$	The boundary of the CGDs at t_k.
τ_k	The IPE & FRD configuration at t_k.
$\mathbf{S}^k$	The set of sampling beams at t_k.
$\mathbf{u}_r^k$	The reduced DoFs after *interpolation* at t_k.
$\mathbf{f}_{int}^k$	The internal force vector corresponding to $\mathbf{u}_r^k$.
Φ_k^{k-1}	The interpolation matrix relating $\mathbf{u}_r^k$ to $\mathbf{u}_r^{k-1}$.
κ_{tol}	The threshold of the energy discrepancy.
V_{tol}	The minimally acceptable area/volume of a IPE.

Table 3.2: Glossary of the notations.

3.3.3. Adaptive scheme

This section presents the proposed adaptive scheme. Table 3.2 lists a glossary of symbols that are used in the pseudo code of the adaptive scheme of Alg. 2. Also for

better illustration, the concepts of FRDs, CGDs, IPEs, IPE nodes, IPE-IPE interface and IPE-FRD interface are illustrated in Fig. 3.7.

Algorithm 2: Adaptive scheme.

Initialization: configure Ω_0^{FRD}, Ω_0^{CGD}, τ_0, S^0, set $\mathbf{u}_{\mathrm{r}}^0 = \mathbf{0}$, $\mathbf{f}_{\mathrm{int}}^0 = \mathbf{0}$.
for *k = 1,2,...,n* **do**
  Inherit configurations of previous time step, i.e. $\Omega_{\mathrm{k}}^{\mathrm{FRD}} = \Omega_{\mathrm{k-1}}^{\mathrm{FRD}}$, $\Omega_{\mathrm{k}}^{\mathrm{CGD}} = \Omega_{\mathrm{k-1}}^{\mathrm{CGD}}$, $\tau_{\mathrm{k}} = \tau_{\mathrm{k-1}}$, $S^{\mathrm{k}} = S^{\mathrm{k-1}}$, $\mathbf{u}_{\mathrm{r}}^{\mathrm{k}} = \mathbf{u}_{\mathrm{r}}^{\mathrm{k-1}}$, $\mathbf{f}_{\mathrm{int}}^{\mathrm{k}} = \mathbf{f}_{\mathrm{int}}^{\mathrm{k-1}}$.
  Apply boundary conditions of t_{k} to $\partial\Omega_{\mathrm{k}}^{\mathrm{FRD}}$ and $\partial\Omega_{\mathrm{k}}^{\mathrm{CGD}}$.
  Equilibrate the unbalanced system by solving Eq. (3.4).
  Evaluate energy discrepancy κ for IPE-IPE interfaces in τ_{k}, identify the IPEs with $\kappa > \kappa_{\mathrm{tol}}$ and collect them in set τ_{refine}.
  while $\tau_{refine} \neq \emptyset$ **do**
    Apply Alg. 1.
    Update $\Omega_{\mathrm{k}}^{\mathrm{FRD}}$, $\Omega_{\mathrm{k}}^{\mathrm{CGD}}$, τ_{k}, S^{k}.
    Compute interpolation matrix $\Phi_{\mathrm{k}}^{\mathrm{k-1}}$, reset initial guess as $\mathbf{u}_{\mathrm{r}}^{\mathrm{k}} = \Phi_{\mathrm{k}}^{\mathrm{k-1}}\mathbf{u}_{\mathrm{r}}^{\mathrm{k-1}}$, update $\mathbf{f}_{\mathrm{int}}^{\mathrm{k}}$ accordingly.
    Equilibrate the unbalanced system by solving Eq. (3.4).
    Evaluate energy discrepancy κ for IPE-IPE interfaces in τ_{k}, identify the IPEs with $\kappa > \kappa_{\mathrm{tol}}$ and collect them in set τ_{refine}.
  Evaluate energy discrepancy κ for IPE-FRD interfaces in τ_{k}, identify the IPEs with $\kappa > \kappa_{\mathrm{tol}}$ and collect them in set τ_{resolve}.
  while $\tau_{resolve} \neq \emptyset$ **do**
    Transform the IPEs in τ_{resolve} into FRDs.
    Update $\Omega_{\mathrm{k}}^{\mathrm{FRD}}$, $\Omega_{\mathrm{k}}^{\mathrm{CGD}}$, τ_{k}, S^{k}.
    Compute interpolation matrix $\Phi_{\mathrm{k}}^{\mathrm{k-1}}$, reset initial guess $\mathbf{u}_{\mathrm{r}}^{k} = \Phi_{\mathrm{k}}^{\mathrm{k-1}}\mathbf{u}_{\mathrm{r}}^{\mathrm{k-1}}$, update $\mathbf{f}_{\mathrm{int}}^{\mathrm{k}}$ accordingly.
    Equilibrate the unbalanced system by solving Eq. (3.4).
    Evaluate energy discrepancy κ for IPE-FRD interfaces in τ_{k}, identify the IPEs with $\kappa > \kappa_{\mathrm{tol}}$ and collect them in set τ_{resolve}.
  Store output data of current time step: $\Omega_{\mathrm{k}}^{\mathrm{FRD}}$, $\Omega_{\mathrm{k}}^{\mathrm{CGD}}$, τ_{k}, S^{k}, $\mathbf{u}_{\mathrm{r}}^{\mathrm{k}}$, $\mathbf{f}_{\mathrm{int}}^{\mathrm{k}}$.

Two issues in Alg. 2 are are clarified here. First, the interpolation matrix $\Phi_{\mathrm{k}}^{\mathrm{k-1}}$ denotes the matrix necessary to give an appropriate initial guess to a new (i.e. refined) IPEs & FRD configuration in order to solve the current time step (t_{k}) in a

Newton algorithm. This is accomplished by projecting the converged solution at t_{k-1}, $\mathbf{u}_r^{k-1}$, as initial guess for time step t_k with the new IPE & FRD configuration, $\mathbf{u}_r^k$. In other words, the only goal of Φ_k^{k-1} is to equip newly created nodes (i.e. new beam nodes in FRDs and new IPE nodes) with an initial guess that is in accordance with the converged solution at t_{k-1} for the previous IPE & FRD configuration.

A second issue that needs clarification is that the energy discrepancy is first measured for IPE-IPE interfaces (lines 6–12 in Alg. 2) and subsequently for IPE-FRD interfaces (lines 13–19). The reason to split the measuring of the energy discrepancy in two stages is that IPE refinement only results in a few more DoFs and sampling beams, whereas transforming IPEs into FRDs yields considerably more DoFs and sampling beams. It is therefore computationally more beneficial to prioritize the refinement of the IPEs.

3.3.4. Choice of the adaptivity parameters

The appropriate values for the threshold of the energy discrepancy, κ_{tol}, and the volume threshold to fully resolve an IPE, V_{tol}, are case specific.

Different shapes of unit cells, beam discretization of unit cells and sizes of lattices were observed to require different $[\kappa_{tol}, V_{tol}]$ sets. The choice of κ_{tol} and V_{tol} actually depends on the trade-off between the accuracy of the results and the computational saving. In this section some recommendations for tuning the adaptivity parameters are given.

Generally, a small κ_{tol} promotes the accuracy of the simulation because the energy discrepancy across the IPE-IPE and IPE-FRD interfaces is reduced. However, excessively small κ_{tol} risks over refinement for the AGQC (i.e. tendency for large FRD and small IPEs) and thus compromises the computational saving.

In a similar fashion V_{tol} should not be too large, because this would result in the direct transformation of large IPEs into FRD (promoting a DNS like simulation). On the other hand, V_{tol} should not be too small, because a too low value can result in IPEs having more sampling beams than the underlying number of lattice beams in the IPE volume, i.e. the computational effort would be larger for the IPE than considering the same volume as FRD. To avoid this, one possible solution could be to track the actual number of lattice beams inside an IPE on the fly to decide whether or not fully resolving it. This can however be a computationally expensive practice and may be considered in future work. A second, simpler option used in this work, is to set the lower bound of V_{tol} as the product between the volume of one unit cell and the number of Gauss quadrature points in an IPE. A higher V_{tol} than this lower bound is used in the simulations. It is noteworthy that in the simulations choosing a V_{tol} close to its lower bound was observed to yield more accurate results when compared to DNS. This can be explained by a small V_{tol} resulting in small IPEs around the FRDs creating a kinematically rich (but computationally efficient) zone near the region of main interest, as well as a sound transition from FRDs to large IPEs through IPEs with gradually increasing size further from this region.

The optimal values of κ_{tol} and V_{tol} were chosen in this work by trial-running a few increments in the AGQC simulation using several options of κ_{tol} and V_{tol} and observing the resulting range and intensity of the refinement. The improvement

of the computational saving and the difference in accuracy can then be accessed by comparing the overall response of different AGQC simulations (as explained in Section 3.4.2) to choose the most promising $[\kappa_{\text{tol}}, V_{\text{tol}}]$ set.

3.4. Application of adaptive GQC

In this section, five numerical examples are presented. The example of Section 3.4.1 demonstrates that the proposed refinement indicator is insensitive to uniform deformation and rigid body rotation. The example of Section 3.4.1 illustrates the capabilities of the adaptive generalized QC method by indenting a BCC lattice, and a procedure for choosing $[\kappa_{\text{tol}}, V_{\text{tol}}]$ is proposed. The examples of Section 3.4.3 and 3.4.4 show that the adaptive scheme is also able to treat on the fly progressive refinement during the simulation of a BBC and a Kelvin lattice scratched by a rigid sphere. The example of Section 3.4.5 showcases the ability of AGQC to simulate the scratch of a large Kelvin lattice, which is computationally too demanding for DNS.

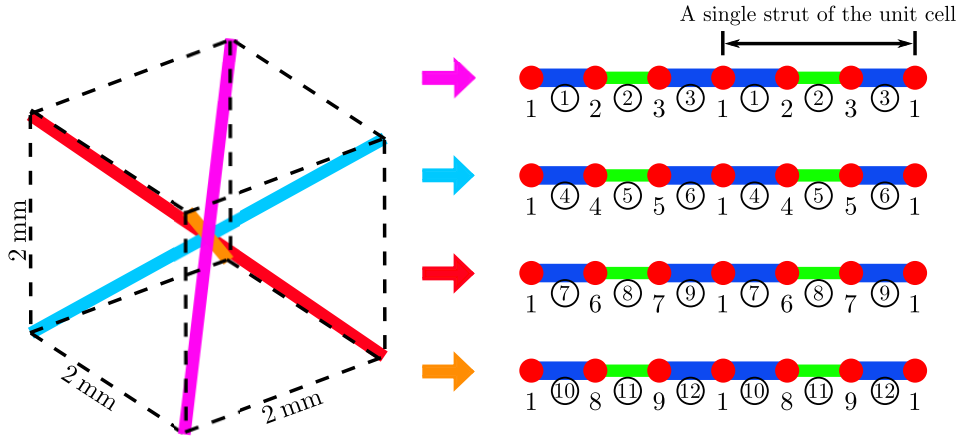

Figure 3.8: Beam representation of a BCC unit cell. All blue beams are given the same geometrical and material parameters and the green beams are given their own geometrical and material parameters. Beam node (•) types are indicated as $1-9$. Beam types are indicated as ①–⑫.

The beam representation of the BCC unit cell we adopt is shown in Fig. 3.8. All beams have circular cross sections. However, the diameter of the blue beams is 0.230 mm, whereas that of the green beams is 0.185 mm. The beams are formulated as elastic, geometrically non-linear co-rotational beams, with a Young's modulus of 140 GPa and a Poisson's ratio of 0.3. These geometrical and material parameters are the same as used in [41].

The beam representation of the Kelvin unit cell we consider is shown in Fig. 3.9. Each of the 36 struts, which are of equal length, is represented using one beam finite element. Each beam is assumed to have a circular cross section with a diameter of

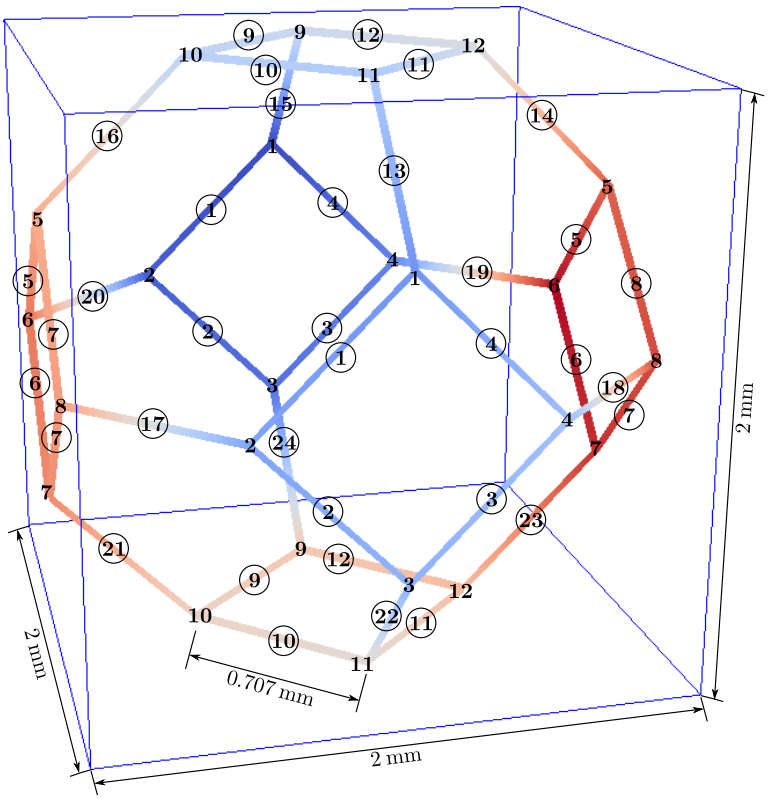

Figure 3.9: Beam representation of the Kelvin unit cell. Beam node types are indicated as 1 – 12. Beam element types are indicated as ① – ㉔.

0.230 mm, a Young's modulus of 140 GPa and a Poisson's ratio of 0.3.

In order to apply *the interpolation* of the generalized QC method, the beam nodes of a unit cell are classified into different types in the light of the periodicity. Differentiated by the beam node type of both ends, the beam elements in a unit cell are also categorized into several types. The classification of beam nodes and beam elements are indicated in Fig. 3.8 for the BCC unit cell and Fig. 3.9 for the Kelvin unit cell.

It is also worth noting that the lattice is obtained by repeating the unit cell in X, Y, Z directions. For BCC unit cell, the stacking will not lead to overlapping struts. But for the Kelvin unit cell, there will be overlapping struts (i.e. the beams of types ① – ⑫). When we use this unit cell as the sampling unit cell at the Gauss quadrature points in IPEs, the overlapping beams are assigned with half of the area and the inertia of the beam. When a Kelvin unit cell is used as the signaling unit cell, these overlapping beams are considered with their actual diameter for the measurement of the elastic strain energy.

Linear tetrahedral IPEs are used in all simulations. Five GQPs per IPE are used to

generate sampling beams, because this was observed to be the minimum number that guarantees convergence [23].

3.4.1. Uniaxial compression of a BCC lattice

This section aims to show that the new refinement indicator does not trigger refinement if homogeneous deformation and/or rigid body rotation occur.

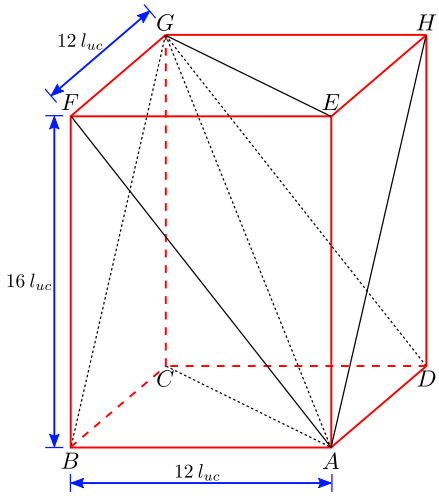

(a) Sketch of Scheme 1.

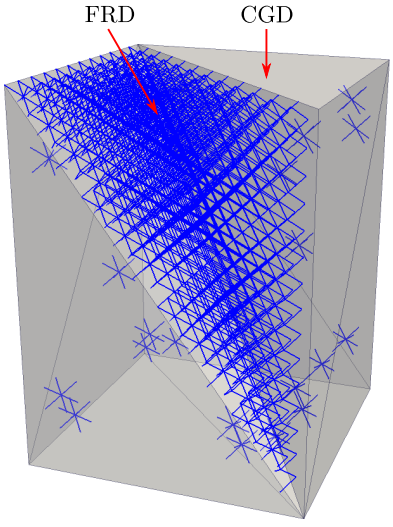

(b) Render of Scheme 1.

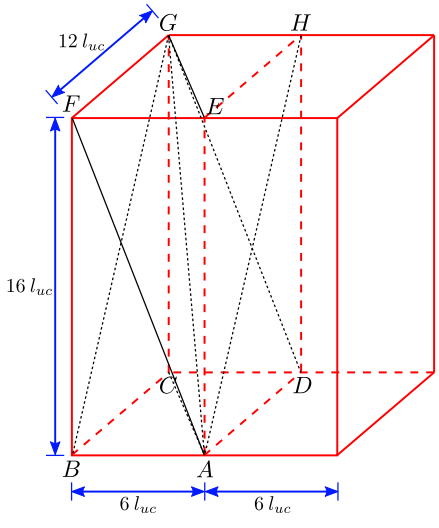

(c) Sketch of Scheme 2.

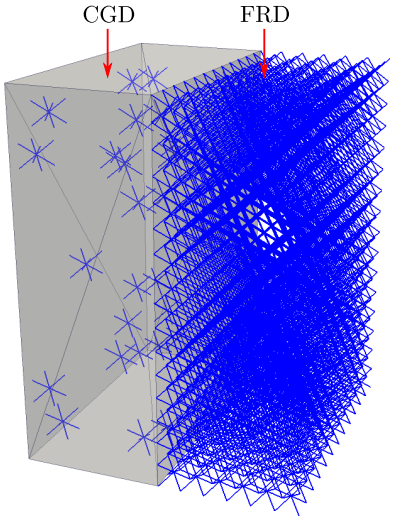

(d) Render of Scheme 2.

Figure 3.10: The interpolation schemes for the lattice under uniaxial compression. l_{uc} denotes the length of one unit cell, which equals 2 mm.

Particularly, we study uniform compression. The studied BCC lattice is illustrated in Fig. 3.10, together with the FRD and IPEs. Two IPE-FRD interfaces and four IPE-IPE interfaces interfaces can be distinguished for the model of Fig. 3.10a, 3.10b. Two IPE-FRD interfaces and six IPE-IPE interfaces are present in the model of Fig. 3.10c, 3.10d. During the simulation the energy discrepancies at all these interfaces are monitored.

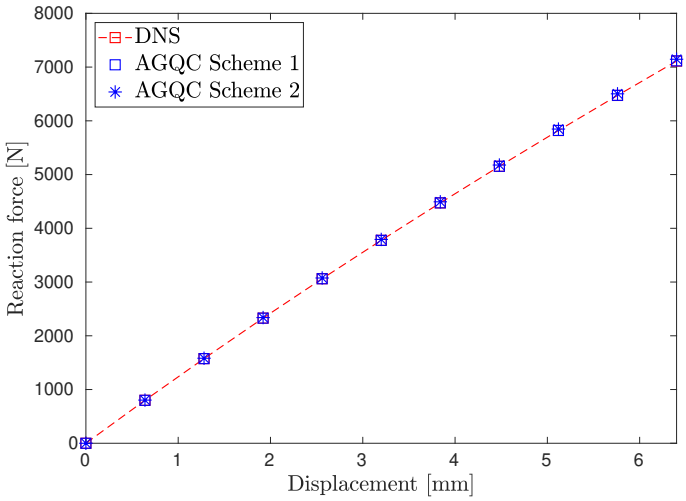

Figure 3.11: Force-displacement response of the lattice under uniaxial compression.

The DNS (i.e. full FRD representation of the model) and the adaptive generalized QC method results are compared. Fig. 3.11 shows that both force-displacement curves practically match.

Fig. 3.11 presents the evolution of the energy discrepancy at the different interfaces. The energy discrepancies at the IPE-IPE interfaces remain zero throughout the loading process. The energy discrepancies of the IPE-FRD interfaces are non-zero, yet they are relatively small. The reason is a (small) error induced by the summation rule, i.e. the ways of constructing the governing equations in the CGDs and the FRDs are different.

It is emphasized that because this error is inherent to the method, the energy discrepancy remains practically the same during loading. Hence, no refinement is triggered in case of homogeneous deformation of arbitrary magnitude (assuming κ_{tol} is set high enough). $\kappa_{\text{tol}} = 0.2$ gives satisfactory result for the considered BCC lattice in the simulations performed in this work.

It is also worth noting that the refinement indicator is insensitive to rigid body translations and rotations because of using 3D co-rotational beam finite elements to represent the lattice structure, capable of handling large displacements and finite rotations [37, 42].

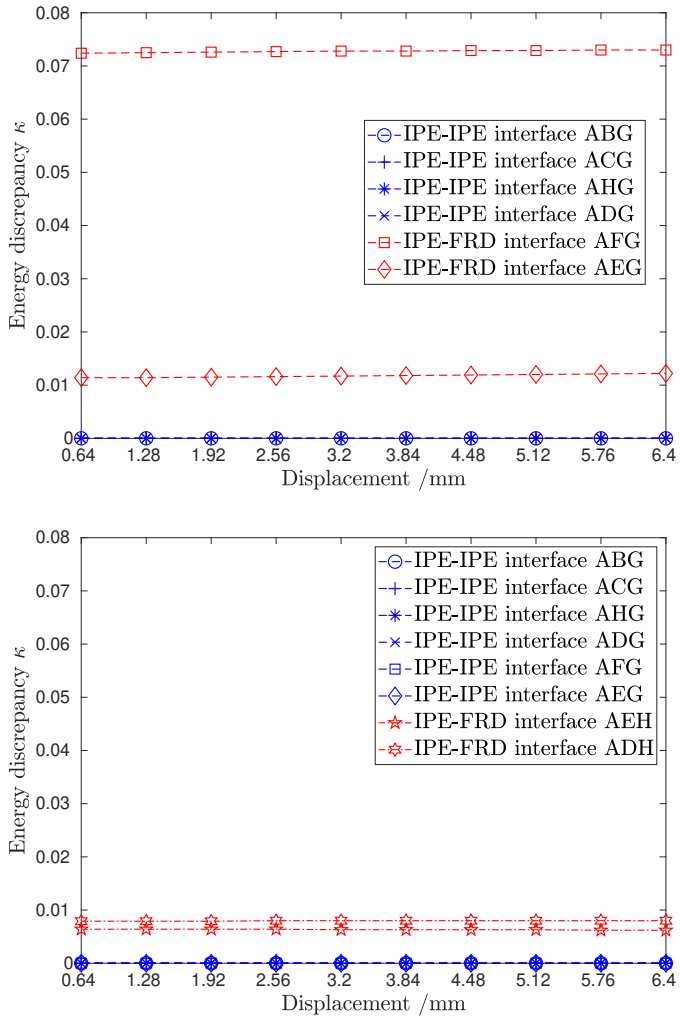

Figure 3.12: Energy discrepancies for different interfaces. Top: scheme 1 (Fig. 3.10a, 3.10b), bottom: scheme 2 (Fig. 3.10c, 3.10d).

3.4.2. Spherical indentation of a BCC lattice

In this section, the adaptive generalized QC method is applied to simulate the indentation of a BCC lattice with a rigid sphere. The model consists of $36 \times 36 \times 36$ BCC unit cells (see Fig. 3.13). The radius of the rigid sphere (r_{sp}) is 10 mm, which is 5 times the length of one unit cell (l_{uc}). As indentation occurs in the center of the model, both the lattice itself and the boundary conditions are symmetric, only a quarter of the model was considered thanks to symmetrical boundary conditions. As is indicated in Fig. 3.13, the beam nodes on the bottom are constrained from

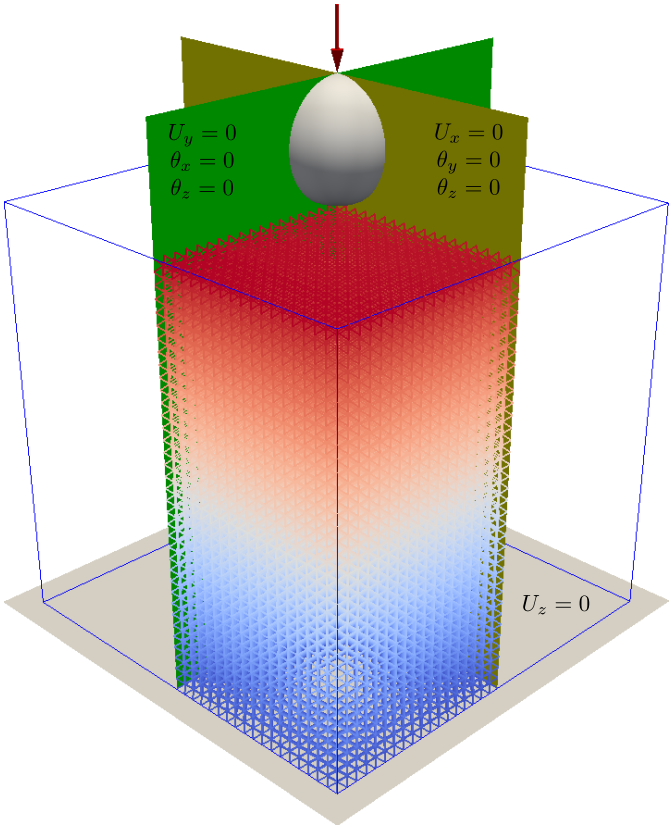

Figure 3.13: Quarter model for the indentation of a BCC lattice.

moving in the normal direction (i.e. $U_z = 0$). For the two symmetrical faces (i.e. the yellow and green faces in Fig. 3.13), beam nodes are constrained from normal displacement and out-of-plane rotations (i.e. $U_y = \theta_x = \theta_z = 0$ for the green face, $U_x = \theta_y = \theta_z = 0$ for the yellow face). All the other DoFs of the beam nodes are free. The final indentation depth is set to 2 mm, which equals the unit cell length. The indentation is achieved in 100 increments.

Contact between the lattice and the rigid sphere is modeled using a node-to-segment scheme. The penalty approach is used to incorporate the unilateral frictionless contact conditions [43–47]. The penalty parameter is set to 10^3 N/mm in all simulations in this contribution and not updated during the simulation.

Two non-adaptive QC simulations are considered in order to obtain more reference results than only those of the DNS. In the first non-adaptive QC simulation, an FRD of $6 \times 6 \times 6$ unit cells is incorporated below the rigid sphere (Fig. 3.14a). In the second non-adaptive QC simulation, the FRD is enlarged to $12 \times 12 \times 12$ unit cells (Fig. 3.14b).

For the adaptive generalized QC simulations, the scheme of Fig. 3.14a is chosen

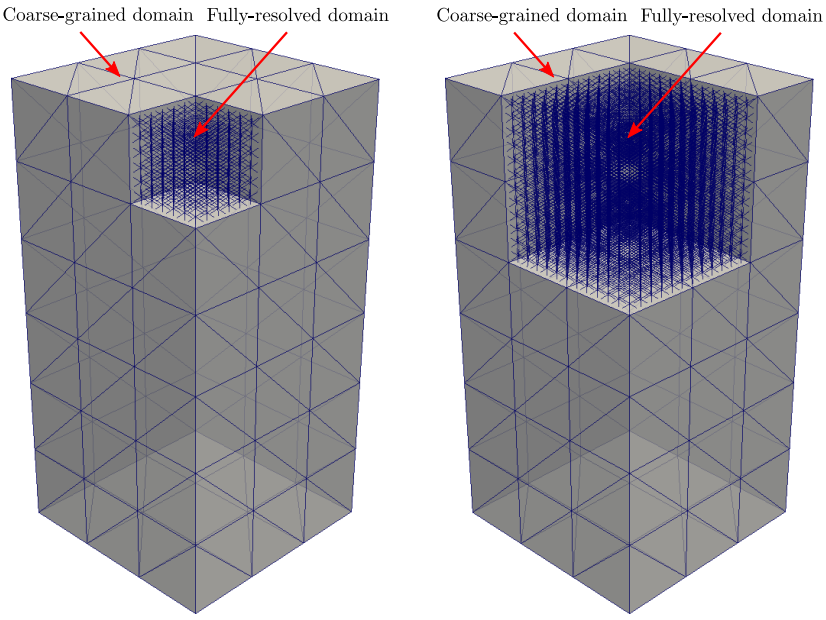

(a) FRD $6\ l_{uc} \times 6\ l_{uc} \times 6\ l_{uc}$ **(b)** FRD $12\ l_{uc} \times 12\ l_{uc} \times 12\ l_{uc}$

Figure 3.14: Interpolation schemes of the lattice under indentation. l_{uc} denotes the length of one unit cell.

as the initial configuration. The control parameters of the adaptivity are set as follows. To study the influence of κ_{tol}, we fix V_{tol} to be five times the volume of a unit cell (i.e. $5\ l_{uc}^3$) and set κ_{tol} to be 0.8, 0.6, 0.4, 0.2 in different simulations. To study the influence of V_{tol}, we fix κ_{tol} to be 0.2, 0.4 and set V_{tol} to be $5\ l_{uc}^3$, $10\ l_{uc}^3$, $15\ l_{uc}^3$ in successive simulations.

Fig. 3.15 plots the curves of the normal contact force versus the indentation depth under constant V_{tol} (Fig. 3.15a) and κ_{tol} (Fig. 3.15b and 3.15c) respectively. As can be seen, the force – displacement curves include several kinks that are attributed to the progressive establishment of contacts during the indentation. In other words, the deeper we indent the rigid sphere, the more beam nodes come in contact with the rigid sphere. In Fig. 3.15a, there are two apparent kinks: kink 1 happens because the number of contact points between the rigid sphere and the lattice jumps from 1 to 3; kink 2 happens because the number of contact points jumps from 4 to 6.

To illustrate the difference between the models, the initial contact stiffness was calculated up to 0.02 mm indentation depth (Fig. 3.18). The initial stiffness is notably different and it can be used to decide on κ_{tol} in a first few increments: $\kappa_{\text{tol}} = 0.4$ and $\kappa_{\text{tol}} = 0.2$ yield close results (hence $\kappa_{\text{tol}} = 0.4$ could be chosen for a complete simulation).

The value of κ_{tol} has a more significant impact on the accuracy in the considered

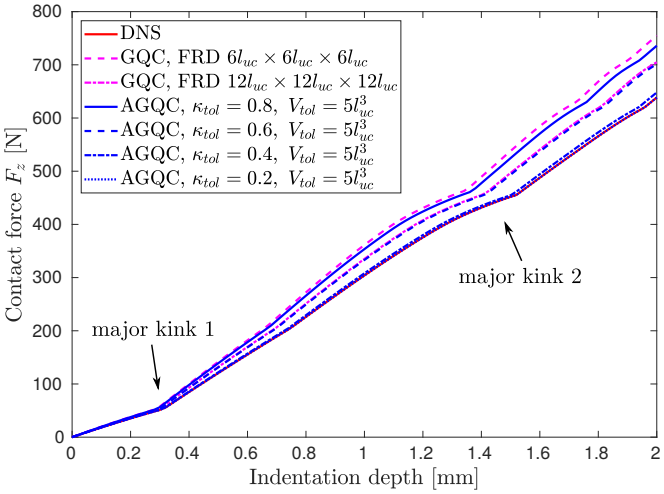

(a) $V_{\text{tol}} = 5\ l_{uc}^3$

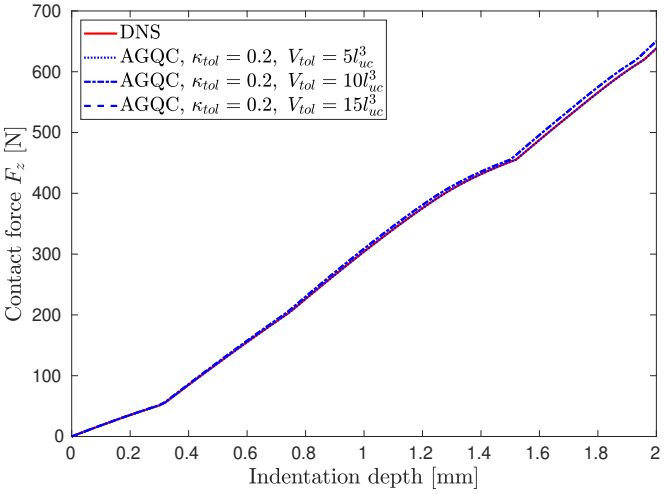

(b) $\kappa_{\text{tol}} = 0.2$

Figure 3.15: The normal contact force versus the indentation depth. l_{uc} denotes the length of one unit cell.

range compared to V_{tol}. The smaller the values of κ_{tol} and V_{tol} are (within the bounds defined in Section 3.3.4), the more accurate the result is.

To visualize the refinement procedure throughout the AGQC simulations, Fig. 3.16 and Fig. 3.17 monitor three quantities denoted as KV%, SB% and V_{CGD}%. KV% denotes the ratio between the number of DoFs (kinematic variables) in the QC model

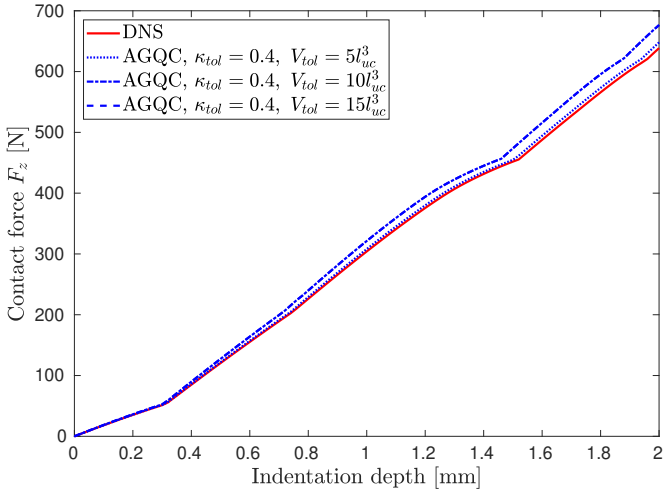

(c) $\kappa_{\text{tol}} = 0.4$

Figure 3.15: The normal contact force versus the indentation depth. l_{uc} denotes the length of one unit cell.

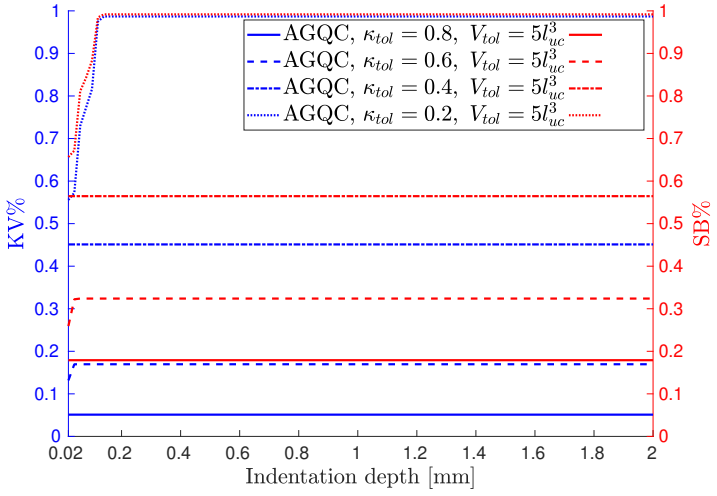

(a) $V_{\text{tol}} = 5\ l_{uc}^3$

Figure 3.16: The evolution of KV% and SB% during the indentation of the BCC lattice. l_{uc} denotes the length of one unit cell.

and the number of DoFs in the DNS. SB% denotes the ratio between the number

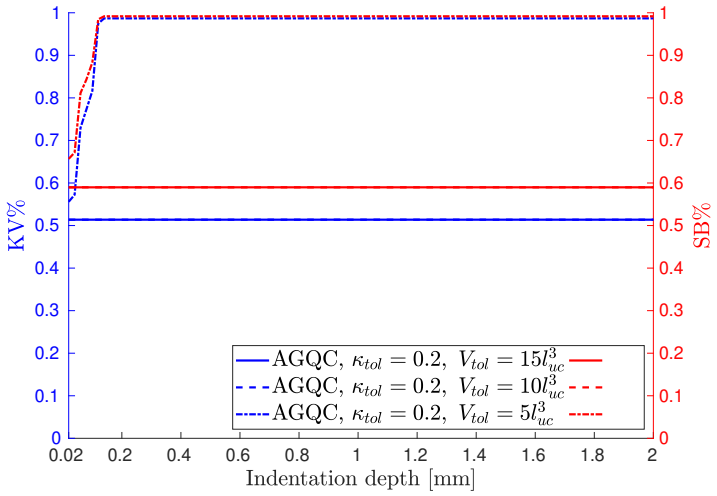

(b) $\kappa_{\text{tol}} = 0.2$

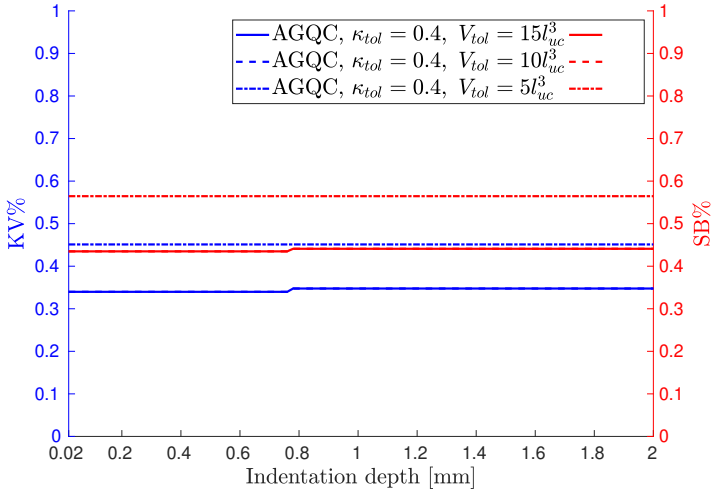

(c) $\kappa_{\text{tol}} = 0.4$

Figure 3.16: The evolution of KV% and SB% during the indentation of the BCC lattice. l_{uc} denotes the length of one unit cell.

of sampling beams in the QC model and the number of beams in the DNS. $V_{\text{CGD}}\%$ denotes the volumetric fraction of CGD.

Table 3.3 provides a detailed comparison among the different modeling schemes in terms of the model scales, the error and the required computational time. The required computational time is the walltime of running the in-house MATLAB codes

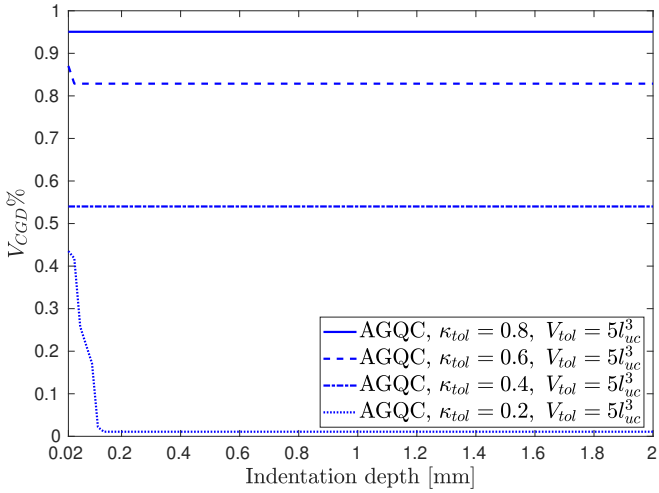

(a) $V_{\text{tol}} = 5\ l_{uc}^3$

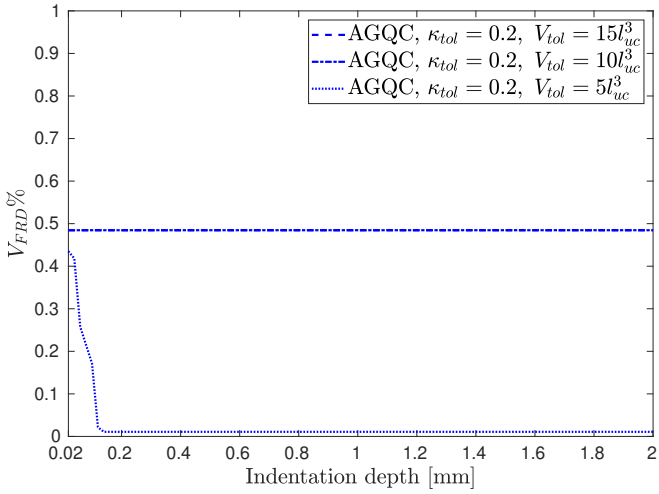

(b) $\kappa_{\text{tol}} = 0.2$. The results of $V_{\text{tol}} = 10l_{uc}^3$ and $V_{\text{tol}} = 15l_{uc}^3$ are consistent.

Figure 3.17: The evolution of $V_{\text{FRD}}\%$ during the indentation of the BCC lattice. l_{uc} denotes the length of one unit cell.

on the HPC Hydra (`https://hpc.ulb.be/`). The codes of both AGQC and DNS are parallelized and are running using 12 cores. In Table 3.3, the DNS result serves as the reference solution. The discrepancy between the results of the different QC models and the DNS solution is quantified as the difference of external work, which is computed from the force-displacement curves in Fig. 3.15 using the trape-

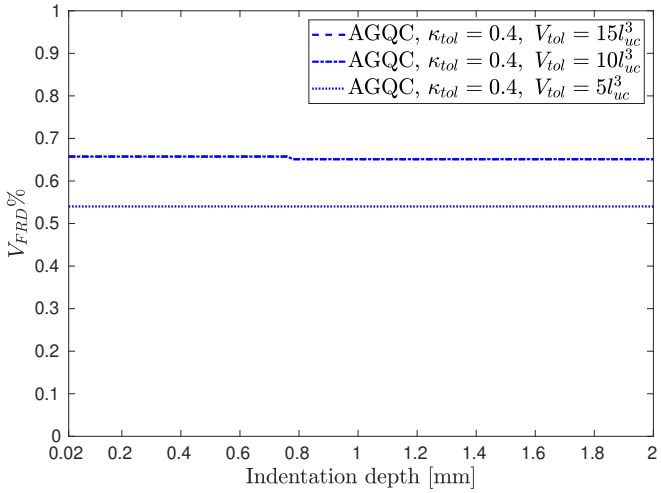

(c) $\kappa_{\text{tol}} = 0.4$. The results of $V_{\text{tol}} = 10l_{uc}^3$ and $V_{\text{tol}} = 15l_{uc}^3$ are consistent.

Figure 3.17: The evolution of $V_{\text{FRD}}\%$ during the indentation of the BCC lattice. l_{uc} denotes the length of one unit cell.

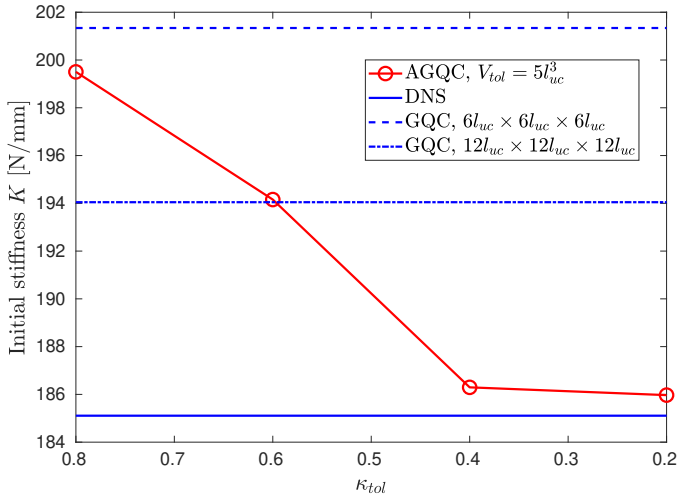

Figure 3.18: Comparison of initial stiffness of the variant model schemes.

zoidal rule. Also, because progressive refinement can be observed in Fig. 3.16 and Fig. 3.17, the average number of DoFs, the average number of sampling beams and the average volume fraction of CGDs are shown in Table 3.3. They are obtained by computing the mean value of the corresponding items out of the 100 increments.

We choose to calculate the average values because the number of DoFs, the number of sampling beams and the volume fraction of CGDs can vary from increment to increment during the progressive refinement. Note that in Table 3.3, not only the absolute values of different items are provided, but also the percentage difference between the absolute values and the value of DNS are listed. The refined configurations of the IPEs and FRDs at the end of the loading are shown in Fig. 3.19. Fig. 3.20 plots the contour of displacement components for the DNS lattice at the end of the loading.

The following conclusions can be derived from the above results. When a fixed value is chosen for V_{tol}, reducing the value of κ_{tol} can improve the accuracy. When a fixed value is chosen for κ_{tol}, reducing the value of V_{tol} also benefits the accuracy in the studied range of V_{tol}. However, this does not mean that a pair of as small as possible values for κ_{tol} and V_{tol} gives the optimal results. As can be seen from Table 3.3, when κ_{tol} and V_{tol} are set to 0.2 and $5\ l_{uc}^3$ respectively, excessive refinement is obtained. As a result, almost the whole lattice is fully resolved and because of the refinement procedure (Alg. 2), more computational time is required than that of DNS. The values for κ_{tol} and V_{tol} should be chosen after analyzing their effects on the accuracy and on the computational savings.

The observed trend that smaller V_{tol} benefits the accuracy is against the intuition that larger V_{tol} makes it easier for CGDs to be fully resolved and improve the accuracy (because of the positive correlation between accuracy and the size of FRDs). In this example as shown from Fig. 3.19g to Fig. 3.19r, it turns out to be that larger V_{tol} results in less transformation from CGDs to FRDs. More tests are needed to confirm whether it is a general trend and if so the underlying reason for that. This shows that the effect of V_{tol} on the adjustment of CGD/FRD ratio and therefore on the accuracy of AGQC is more complicated than expected.

For the current example, V_{tol} was fixed first to the lower bound (i.e. $V_{\text{tol}} = 5\ l_{uc}^3$) and one increment was run using different values for κ_{tol}. Observing the initial stiffness (see Fig. 3.18) allowed choosing $\kappa_{\text{tol}} \leq 0.4$. Then for a fixed κ_{tol}, V_{tol} was increased to $10\ l_{uc}^3$ and $15\ l_{uc}^3$ and the first increment recomputed. Based on the obtained initial stiffness and the intensity of the refinement (e.g. the reduction of the number of DoFs and the number of sampling beams) the refinement parameter set $[\kappa_{\text{tol}}, V_{\text{tol}}]$ can be chosen. In the current example, $[\kappa_{\text{tol}} = 0.4, V_{\text{tol}} = 10/15\ l_{uc}^3]$ and $[\kappa_{\text{tol}} = 0.2, V_{\text{tol}} = 10/15\ l_{uc}^3]$ both achieve a satisfactory balance between the accuracy and the magnitude of model reduction. In Fig. 3.16, KV% and SB% are below 1 which should be the upper bound of KV% and SB% since it indicates the reduction of model scale after applying QC (this shows that V_{tol} lower bound was chosen appropriately).

When κ_{tol} is 0.2, tweaking the value of V_{tol} from $5\ l_{uc}^3$ to $10\ l_{uc}^3$ presents a significant improvement for the required computational time while the result is still quite accurate. On the contrary, when κ_{tol} is 0.4, tweaking the value of V_{tol} from $5\ l_{uc}^3$ to $10\ l_{uc}^3$ presents a mild improvement for the required computational time but a mild deterioration to the accuracy. In this case, the loss may not outweigh the gain. Also, when κ_{tol} is 0.2/0.4, setting V_{tol} to be $10\ l_{uc}^3$ and $15\ l_{uc}^3$ gave identical results. The above shows the complex interplay between the refinement parameters.

Modeling scheme	External work (N · mm)	Average number of DoFs	Average number of (sampling) beams	Average volume fraction of CGDs (%)	Computational time (hour)
DNS	595.66	1 269 870	279 936	0	8.4
GQC (FRD $6 \times 6 \times 6$)	698.75 (+17.31%)	29 322 (-97.69%)	43 344 (-84.52%)	98.15	1.1 (-86.90%)
GQC (FRD $12 \times 12 \times 12$)	652.09 (+9.47%)	192 240 (-84.86%)	74 592 (-73.35%)	85.19	2.0 (-76.19%)
AGQC $\kappa_{\text{tol}} = 0.8$ $V_{\text{tol}} = 5\ luc^3$	683.86 (+14.81%)	64 574 (-94.91%)	50 063 (-82.11%)	95.09	1.4 (-83.33%)
AGQC $\kappa_{\text{tol}} = 0.6$ $V_{\text{tol}} = 5\ luc^3$	648.32 (+8.84%)	213 014 (-83.23%)	90 026 (-67.84%)	83.06	3.9 (-53.57%)
AGQC $\kappa_{\text{tol}} = 0.4$ $V_{\text{tol}} = 5\ luc^3$	602.70 (+1.18%)	567 522 (-55.31%)	156 905 (-43.95%)	54.44	4.9 (-41.67%)
AGQC $\kappa_{\text{tol}} = 0.4$ $V_{\text{tol}} = 10\ luc^3$	626.19 (+5.13%)	433 552 (-65.86%)	122 004 (-56.42%)	65.68	3.5 (-58.33%)
AGQC $\kappa_{\text{tol}} = 0.4$ $V_{\text{tol}} = 15\ luc^3$	626.19 (+5.13%)	433 552 (-65.86%)	122 004 (-56.42%)	65.68	3.6 (-57.14%)
AGQC $\kappa_{\text{tol}} = 0.2$ $V_{\text{tol}} = 5\ luc^3$	595.53 (-0.02%)	1 222 217 (-3.57%)	272 259 (-2.74%)	3.48	11.2 (+33.33%)
AGQC $\kappa_{\text{tol}} = 0.2$ $V_{\text{tol}} = 10\ luc^3$	604.31 (+1.45%)	646 259 (-49.10%)	163 903 (-41.45%)	48.95	4.9 (-41.67%)
AGQC $\kappa_{\text{tol}} = 0.2$ $V_{\text{tol}} = 15\ luc^3$	604.31 (+1.45%)	646 259 (-49.10%)	163 903 (-41.45%)	48.95	5.1 (-39.29%)

Table 3.3: Comparison of model scale, accuracy and required computational time among the different modeling schemes.

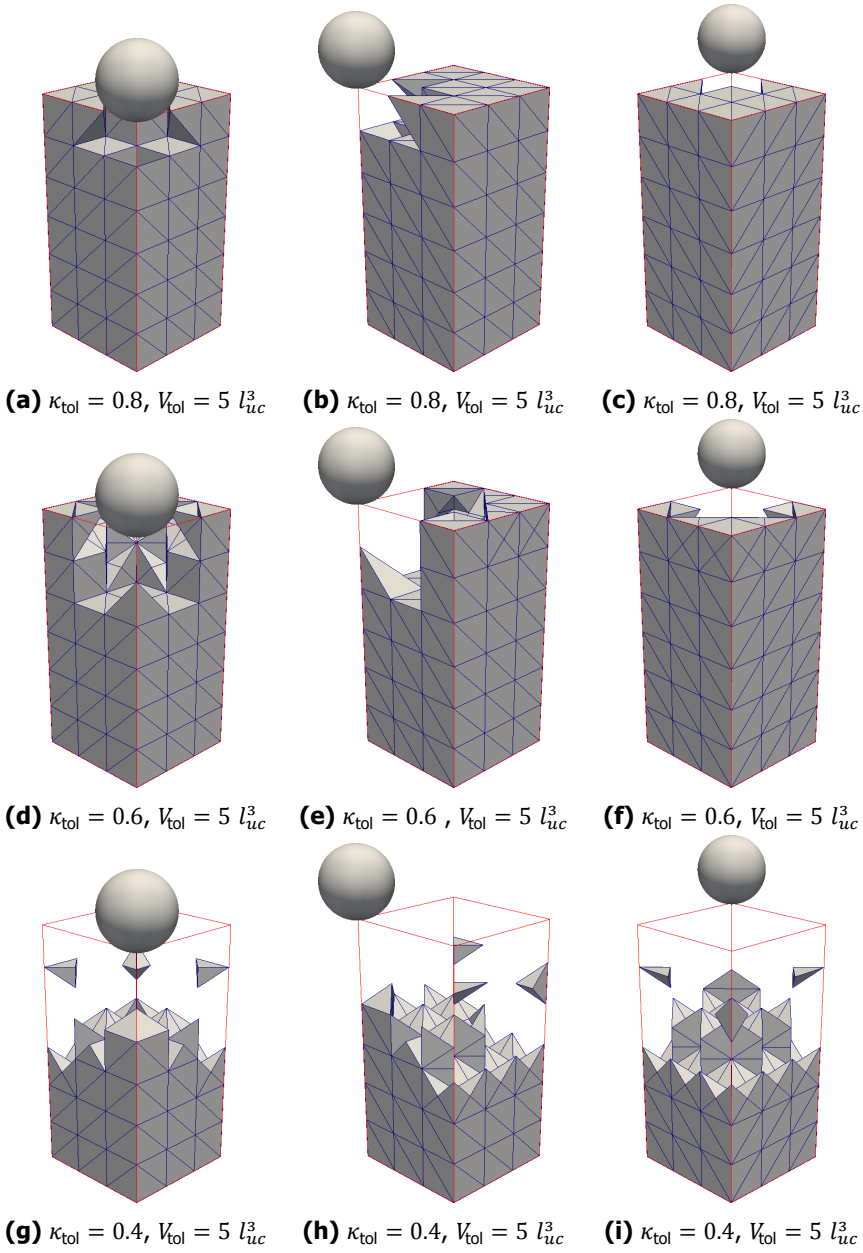

(a) $\kappa_{\text{tol}} = 0.8$, $V_{\text{tol}} = 5\ l_{uc}^3$ **(b)** $\kappa_{\text{tol}} = 0.8$, $V_{\text{tol}} = 5\ l_{uc}^3$ **(c)** $\kappa_{\text{tol}} = 0.8$, $V_{\text{tol}} = 5\ l_{uc}^3$

(d) $\kappa_{\text{tol}} = 0.6$, $V_{\text{tol}} = 5\ l_{uc}^3$ **(e)** $\kappa_{\text{tol}} = 0.6$, $V_{\text{tol}} = 5\ l_{uc}^3$ **(f)** $\kappa_{\text{tol}} = 0.6$, $V_{\text{tol}} = 5\ l_{uc}^3$

(g) $\kappa_{\text{tol}} = 0.4$, $V_{\text{tol}} = 5\ l_{uc}^3$ **(h)** $\kappa_{\text{tol}} = 0.4$, $V_{\text{tol}} = 5\ l_{uc}^3$ **(i)** $\kappa_{\text{tol}} = 0.4$, $V_{\text{tol}} = 5\ l_{uc}^3$

Figure 3.19: Refined IPEs & FRDs for the indentation example at the last increment. Only the the tetrahedral IPEs in the CGDs are visible, together with red lines outlining the model domain. The void in the model domain represents the FRDs. The left column lists the front views, the middle column lists the side views, the right column lists the back views.

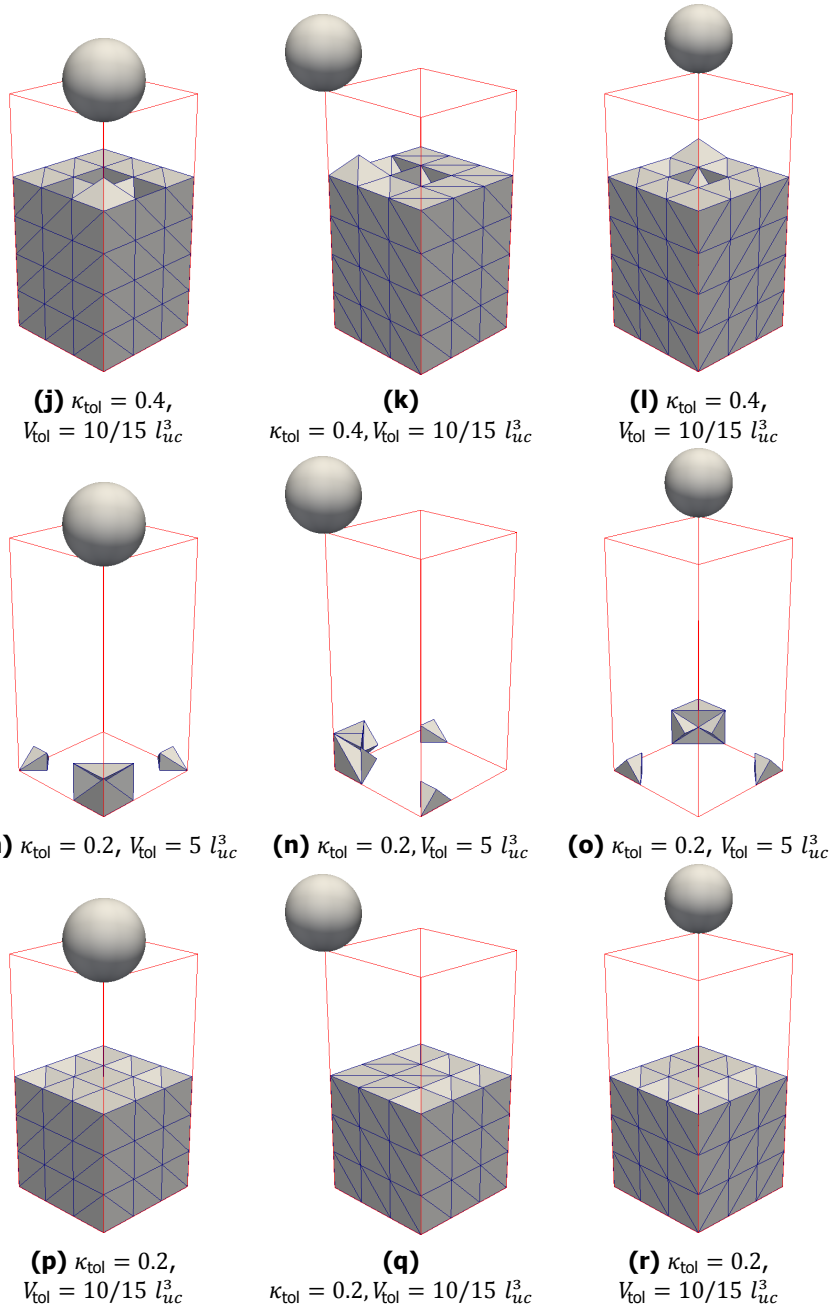

(j) $\kappa_{\text{tol}} = 0.4$, $V_{\text{tol}} = 10/15\ l_{uc}^3$ **(k)** $\kappa_{\text{tol}} = 0.4, V_{\text{tol}} = 10/15\ l_{uc}^3$ **(l)** $\kappa_{\text{tol}} = 0.4$, $V_{\text{tol}} = 10/15\ l_{uc}^3$

(m) $\kappa_{\text{tol}} = 0.2$, $V_{\text{tol}} = 5\ l_{uc}^3$ **(n)** $\kappa_{\text{tol}} = 0.2, V_{\text{tol}} = 5\ l_{uc}^3$ **(o)** $\kappa_{\text{tol}} = 0.2$, $V_{\text{tol}} = 5\ l_{uc}^3$

(p) $\kappa_{\text{tol}} = 0.2$, $V_{\text{tol}} = 10/15\ l_{uc}^3$ **(q)** $\kappa_{\text{tol}} = 0.2, V_{\text{tol}} = 10/15\ l_{uc}^3$ **(r)** $\kappa_{\text{tol}} = 0.2$, $V_{\text{tol}} = 10/15\ l_{uc}^3$

Figure 3.19: Refined IPEs & FRDs for the indentation example at the last increment. Only the the tetrahedral IPEs in the CGDs are visible, together with red lines outlining the model domain. The void in the model domain represents the FRDs. The left column lists the front views, the middle column lists the side views, the right column lists the back views.

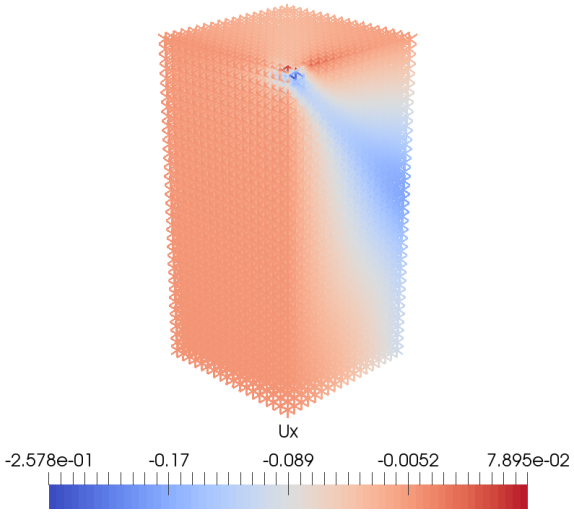

(a) U_x

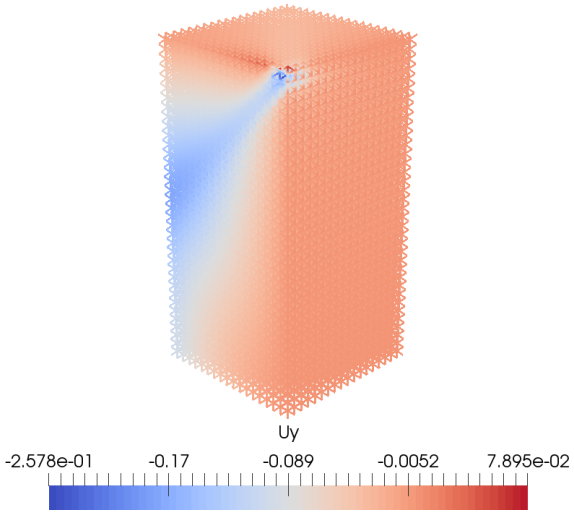

(b) U_y

Figure 3.20: Contour of displacement components [mm] for the BCC lattice from DNS. The maximum of U_z is not exactly 2 mm because of the penalty treatment of the contact condition.

As for this example, no significant progressive refinement was observed. The majority of the refinement is accomplished in the first few increments (see Fig. 3.16 and 3.17). This was beneficial because running a few increments for a given pair of κ_{tol} and V_{tol} could be used as a trustworthy indicator for their optimal choice. In simulations where progressive refinement is significant (Section 3.4.4 & 3.4.5), trial-

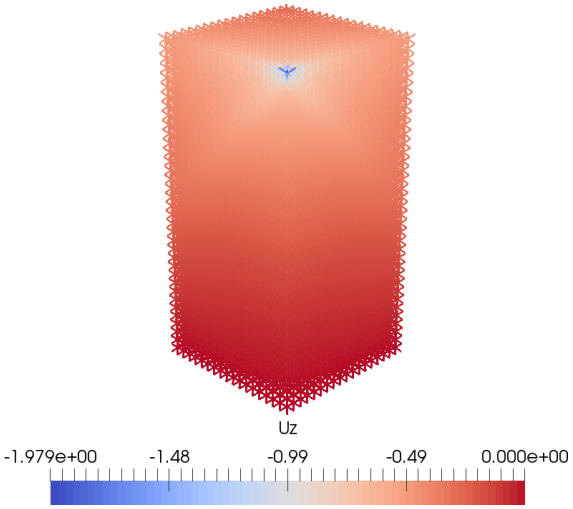

(c) U_z

Figure 3.20: Contour of displacement components [mm] for the BCC lattice from DNS. The maximum of U_z is not exactly 2 mm because of the penalty treatment of the contact condition.

running the first few increments was still observed to be able to indicate optimal adaptivity parameters. The rapid and extensive refinement can be explained by BCC lattices that exhibit strongly non-local deformation modes (see Fig. 3.20, where the indentation prompts far-reaching strain fluctuation). This can be attributed to the orientations of struts in the BCC unit cell as the diagonal struts propagate the load along preferential direction.

Note that although the contours of U_x (Fig. 3.20a) and U_y (Fig. 3.20b) are more heterogeneous than the contour of U_z (Fig. 3.20c), the magnitudes of U_x and U_y are much smaller. Therefore, it is the distribution of U_z that can be looked upon as relevant for the refinement of QC modeling. In Fig. 3.20c, the induced fluctuation of U_z is concentrated in the upper part of the lattice with the lower part of the lattice less significantly impacted. This is the reason why the QC models with $[\kappa_{\text{tol}} = 0.4, V_{\text{tol}} = 5\ l_{uc}^3]$ (Figs 3.19g, 3.19h, 3.19i), $[\kappa_{\text{tol}} = 0.4, V_{\text{tol}} = 10/15\ l_{uc}^3]$ (Figs 3.19j, 3.19k, 3.19l) and $[\kappa_{\text{tol}} = 0.2, V_{\text{tol}} = 10/15\ l_{uc}^3]$ (Figs 3.19p, 3.19q, 3.19r) give relatively accurate results (with the percentage error of external work below 5.13%) by only resolving the upper part of the lattice.

3.4.3. Scratching a BCC lattice with a rigid sphere

In this section, the adaptive generalized QC method is applied to simulate the scratching of an elastic BCC lattice using a rigid sphere. Fig. 3.21 presents some geometrical aspects of the simulation. A difference with the previous example is that the model consists of $5 \times 150 \times 20$ BCC unit cells. The radius of the rigid sphere

is set be 100 mm, which is 50 times the length of a unit cell.

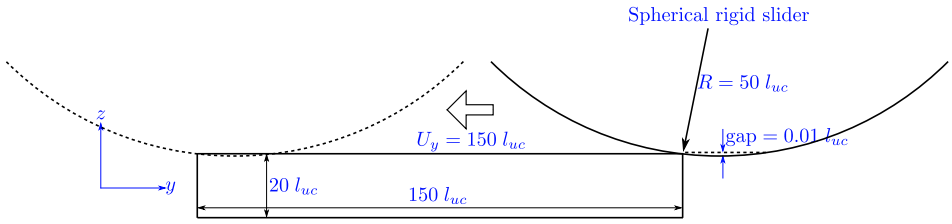

(a) Geometry of the scratch simulation, 2D view. The rigid sphere is moved along the sample surface by $U_y = 150\ l_{uc}$.

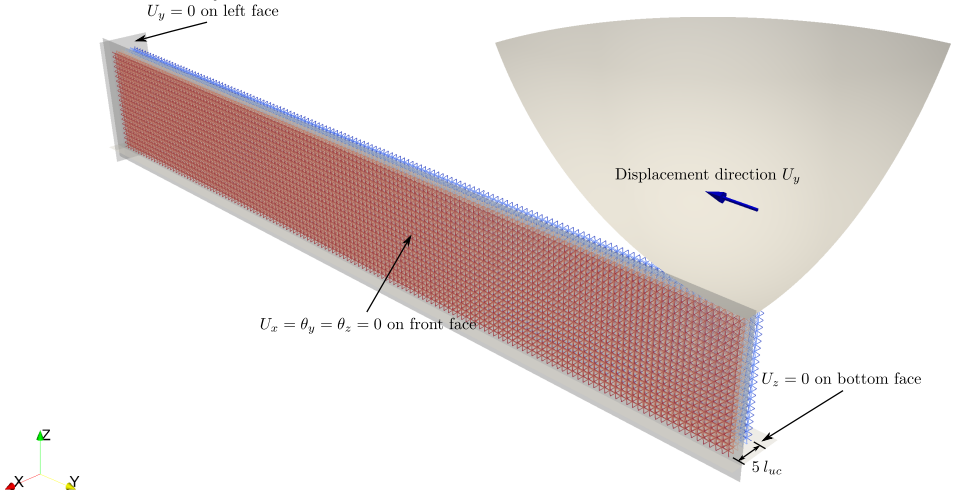

(b) 3D view.

Figure 3.21: Problem setup for the elastic BCC lattice scratching with a rigid sphere.

The rigid sphere is placed so that its lowest point is 0.02 mm ($0.01\ l_{uc}$) below the top face of the lattice. Symmetry boundary conditions are introduced in order to only consider half of the lattice (Fig. 3.21). The penalty approach is used to incorporate the frictionless contact conditions between the lattice and the sphere. The boundary conditions are also indicated in Fig. 3.21b.

In the adaptive QC simulation, V_{tol} is set to five times the volume of a unit cell and κ_{tol} is set to 0.7 (V_{tol} and κ_{tol} are chosen after studying their marginal improvement like the one in Section 3.4.2). Fig. 3.22 depicts the initial configuration of the adaptive generalized QC simulation, where an FRD of $5\ l_{uc} \times 5\ l_{uc} \times 5\ l_{uc}$ is initially used close to the rigid sphere to allow smooth contact establishment. In all the simulations, 100 increments are adopted.

Fig. 3.23 shows the curves of the vertical contact force versus the horizontal displacement of the rigid sphere. Oscillations can be observed because the lattice is inherently discrete. They correspond to the establishment and loss of contact

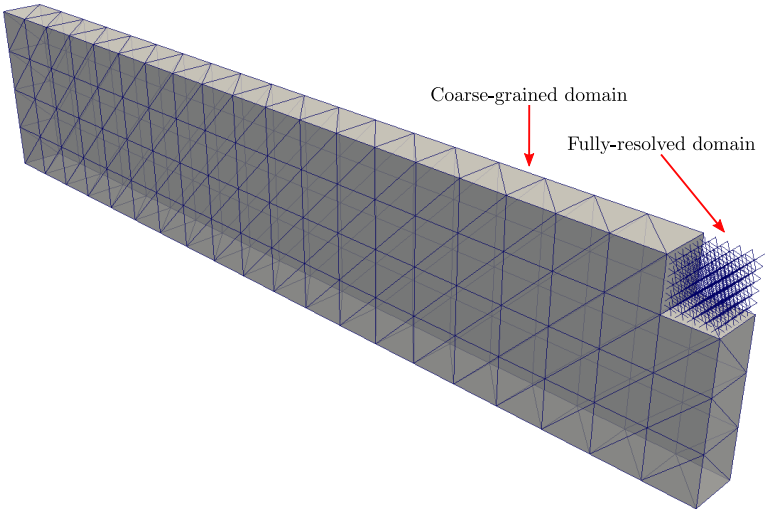

Figure 3.22: Initial discretization for the QC simulation.

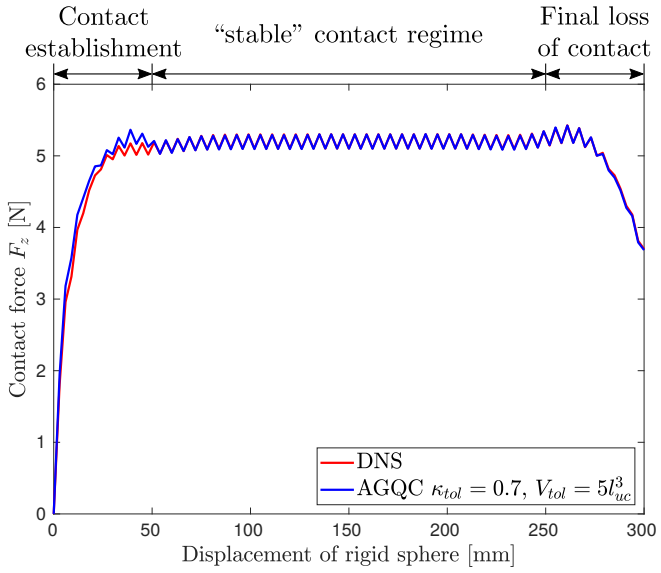

Figure 3.23: The contact force versus the displacement of the rigid sphere for DNS and AGQC approaches of the BCC lattice.

beam-by-beam in the FRD. Also, the force – displacement curve can be divided into three stages, i.e. the stage of contact establishment ($U_y \leq 50$ mm), the stage of "stable" contact regime (50 mm $\leq U_y \leq 250$ mm) and the stage of final loss of contact ($U_y \geq 250$ mm). Contact establishment and final loss of contact span a

displacement range of 50 mm corresponding to the radius of the rigid sphere. The consistency between the DNS result and AGQC results is better for the stage of final loss of contact compared to the stage of contact establishment because almost the whole AGQC model is fully resolved at this stage.

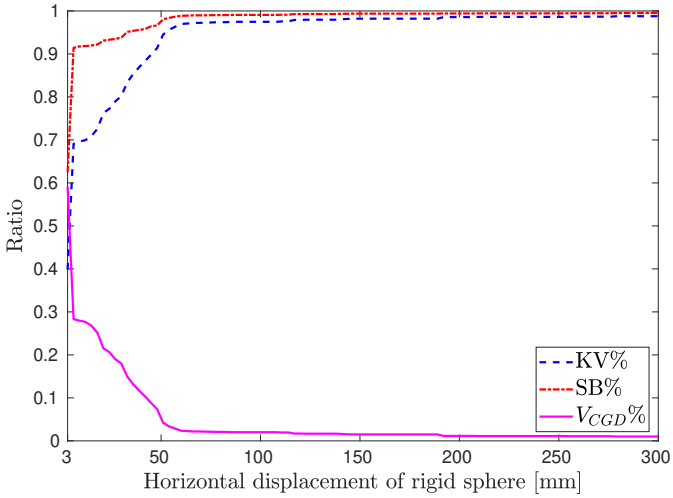

Figure 3.24: Details of the refinement with $\kappa_{\text{tol}} = 0.7$ and $V_{\text{tol}} = 5\ l_{uc}^3$ for the BCC lattice.

Fig. 3.24 illustrates how KV%, SB% and V_{CGD}% evolve as the simulation progresses. As can be seen from Fig. 3.24, during the stage of contact establishment, the portion of the model that is fully resolved leaps to around 90%. This shows that the establishment of contact has far-reaching influence compared to the physical size of the model. BCC unit cells indeed exhibit nonlocal response because of the layout of diagonal struts that provide far-reaching normal force transmission along the diagonal directions. The displacement contours (Figs. 3.25c, 3.25f, 3.25i) illustrate the non-local deformation response of the BCC lattice.

Fig. 3.25 reveals more details of the refinement. As can be seen, the proposed adaptive generalized QC method can successfully adapt the spatial representation of FRDs & IPEs progressively during the simulation.

Because of the non-local deformation response of of the BCC lattice and the relative small size of the lattice (so that DNS can be affordable), a large portion of the lattice is fully resolved and the computational saving is not particularly impressive. Naturally, with larger model sizes, more significant computational savings can be expected and AGQC can allow simulating model sizes that are out of reach for DNS. The example also highlights the importance of *coarsening* in the wake of *refinement*, which is part of future work.

3.4.4. Scratching a Kelvin lattice with a rigid sphere

In this section, the scratching test of Section 3.4.3 is performed (same lattice size & boundary conditions) for a lattice comprised of Kelvin unit cells to illustrate that

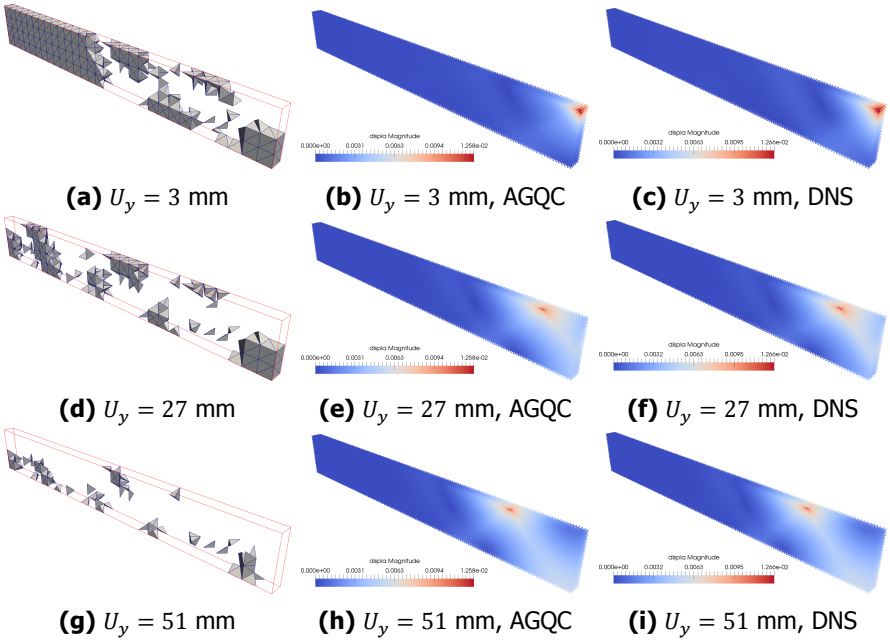

(a) $U_y = 3$ mm **(b)** $U_y = 3$ mm, AGQC **(c)** $U_y = 3$ mm, DNS

(d) $U_y = 27$ mm **(e)** $U_y = 27$ mm, AGQC **(f)** $U_y = 27$ mm, DNS

(g) $U_y = 51$ mm **(h)** $U_y = 51$ mm, AGQC **(i)** $U_y = 51$ mm, DNS

Figure 3.25: Results of the BCC lattice. Left column: the CGDs and the FRDs (void within the red outline) as a function of the displacement (U_y) of the rigid sphere. Middle column: contour of displacement magnitude (i.e. $\sqrt{U_x^2 + U_y^2 + U_z^2}$) of the lattice from adaptive QC simulation. Right column: contour of displacement magnitude of the lattice from the DNS.

the proposed adaptive generalized QC method is applicable to any shape of unit cell as long as it is periodic. We also intend to demonstrate that for different types of lattices, the deformation can be substantially more local and that the QC framework therefore will result in different computational savings depending on the shape and therefore the stress transformation of the unit cell.

All the parameters of Section 3.4.3, except for κ_{tol} and V_{tol}, were preserved in the adaptive QC simulation. κ_{tol} is set to 1.3 and V_{tol} is set to $10\ l_{uc}^3$ (tuned in a preliminary step). Fig. 3.26 plots the curves of the normal contact force versus the tangential displacement of the rigid sphere. Similar to Fig. 3.23, the force – displacement curve of Fig. 3.26 can be divided into three stages, i.e. the stage of contact establishment, the stage of "stable" contact regime and the stage of final loss of contact. A big difference between Fig. 3.23 and Fig. 3.26 is that for BCC unit cell, the transition between the stage of contact establishment and the stage of "stable" contact regime (also between the stage of "stable" contact regime and the stage of final loss of contact) is characterized by a drop (leap) of the contact force. For the Kelvin unit cell, the transition is relatively smooth. This can be explained by the more local response of Kelvin lattice attributed to the different

layout of struts in the Kelvin unit cell. Kelvin unit cells have more diversified strut orientations compared to the BCC unit cell and Kelvin lattice lacks long continuous diagonal strut.

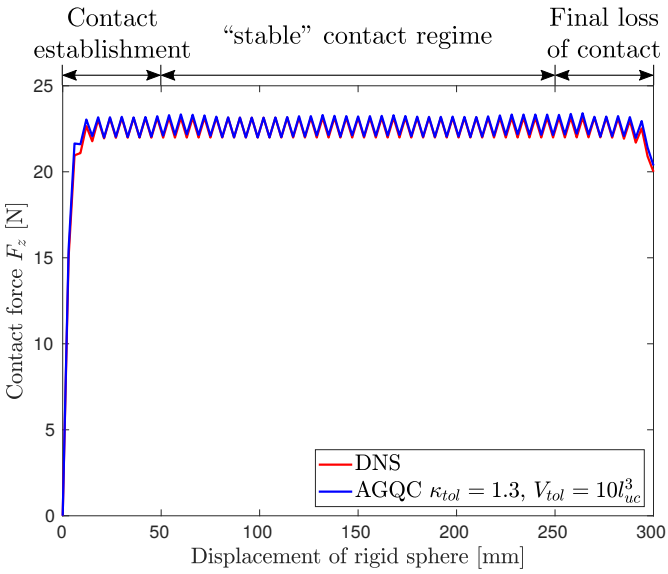

Figure 3.26: The contact force versus the displacement of the rigid sphere for DNS and AGQC approaches of the Kelvin lattice.

The maximum contact force of the Kelvin unit cell is almost five times higher than that of the BCC unit cell and the magnitude of oscillation of the contact force of the Kelvin unit cell is also larger than that of the BCC unit cell. This can be explained by the effective density of the Kelvin unit cell being 2.08 times that of the BCC unit cell (computing the overall volume of all struts in a unit cell corresponding to the different unit cell topology).

Fig. 3.27 shows how KV%, SB% and V_{CGD}% change during the simulation for the Kelvin lattice. Compared to the BCC unit cell in Fig. 3.24, the refinement for the Kelvin unit cell is much more progressive. This can be explained by that the response of the Kelvin unit cell response being much more local compared to the BCC unit cell. This also means more efficient model reduction for unit cells that exhibit localized responses.

Fig. 3.28 plots the discretization of IPE & FRD and the displacement contours as a function of the location of the rigid sphere. Again, the proposed adaptive generalized QC method can successfully adapt the configuration of CGDs and FRDs during the simulation. The displacement contour also verifies the local deformation response of Kelvin unit cell.

Table 3.4 provides a detailed comparison between the model scale, the accuracy and the required computational time for the scratch tests of BCC lattice and Kelvin lattice. For both scratch tests, the AGQC simulations take longer time to fin-

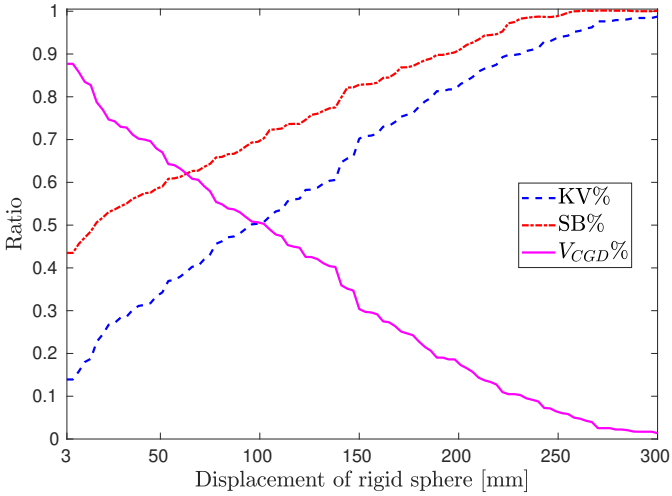

Figure 3.27: Details of the refinement with $\kappa_{\text{tol}} = 1.3$ and $V_{\text{tol}} = 10\ l_{uc}^3$ for the Kelvin lattice.

Unit cell shape	Model scheme	External work (N · mm)	Average number of DoFs	Average number of (sampling) beams	Average volume fraction of CGDs (%)	Computational time (hour)
BCC	DNS	1497.5	1 644 156	360 000	0	8.4
BCC	AGQC	1503.3 (+0.39%)	1 541 864 (-6.22%)	350 581 (-2.61%)	5.63	81.3 (+867.86%)
Kelvin	DNS	6690.8	1 172 400	375 400	0	30.2
Kelvin	AGQC	6728.5 (+0.56%)	756 510 (-35.47%)	296 670 (-20.97%)	35.55	77.2 (+155.63%)

Table 3.4: Comparison of model scale, accuracy and required computational time between the scratch tests of BCC lattice and Kelvin lattice.

ish compared to the DNS because of the iterations of refinement. It is noteworthy to point out that the simulation domains were chosen small enough to allow direct comparison with DNS, corresponding to model sizes disadvantageous for showing the performance gain of AGQC. As the Kelvin lattice yields a more localized response than the BCC lattice, the Kelvin lattice is progressively refined and resolved throughout the simulation and therefore results in a more significant reduction of model scale (Fig. 3.24 and Fig. 3.27). It is also worth noting in Table 3.4 that the DNS simulations of the BCC lattice and the Kelvin lattice need quite different computational times. This is partially because each increment of the BCC lattice takes around three iterations to converge while each increment of the Kelvin lattice takes

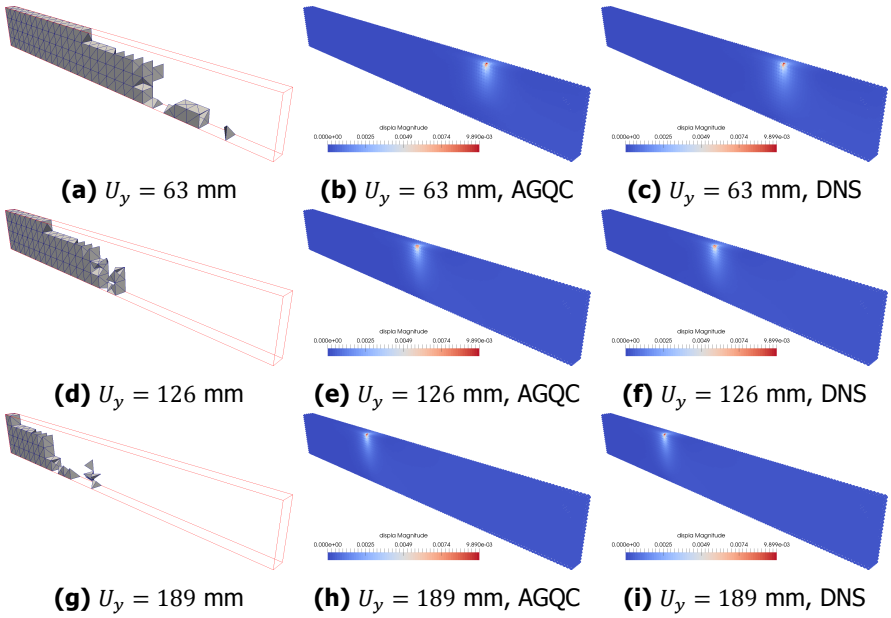

(a) $U_y = 63$ mm **(b)** $U_y = 63$ mm, AGQC **(c)** $U_y = 63$ mm, DNS

(d) $U_y = 126$ mm **(e)** $U_y = 126$ mm, AGQC **(f)** $U_y = 126$ mm, DNS

(g) $U_y = 189$ mm **(h)** $U_y = 189$ mm, AGQC **(i)** $U_y = 189$ mm, DNS

Figure 3.28: Results of the Kelvin lattice. Left column: the IPEs and the FRDs (void within the red outline) as a function of the displacement (U_y) of the rigid sphere. Middle column: contour of displacement magnitude (i.e. $\sqrt{U_x^2 + U_y^2 + U_z^2}$) of the lattice from adaptive QC simulation. Right column: contour of displacement magnitude of the lattice from the DNS.

around five iterations to converge.

3.4.5. Scratching a large Kelvin lattice with a rigid sphere

In this section, the scratching test of Section 3.4.4 is performed for a relatively large elastic Kelvin lattice. The lattice consists of $20 \times 150 \times 80$ Kelvin unit cells along the thickness, length and depth, respectively, resulting in a DNS model with 17 678 400 DoFs and 5 826 400 beam FEs. Such a simulation is no longer feasible by DNS in the current implementation because of the resulting system size but also because of the computational effort of the stiffness matrix assembly. This computational model size makes AGQC preferable to DNS. The boundary conditions were the same as in the previous scratch examples, to allow comparing results to Section 3.4.4, only the lattice size was increased. In the model of Section 3.4.4 the contact zone was already fully enveloped in the FRD. This, together with the local Kelvin lattice response, implies that a similar scratch response is expected for the larger lattice of this section.

The initial discretization of IPEs & FRD of the AGQC simulation is shown in Fig. 3.29. V_{tol} was set to $30\ l_{uc}^3$ and κ_{tol} to 1.5 (tuned in a preliminary step). Note

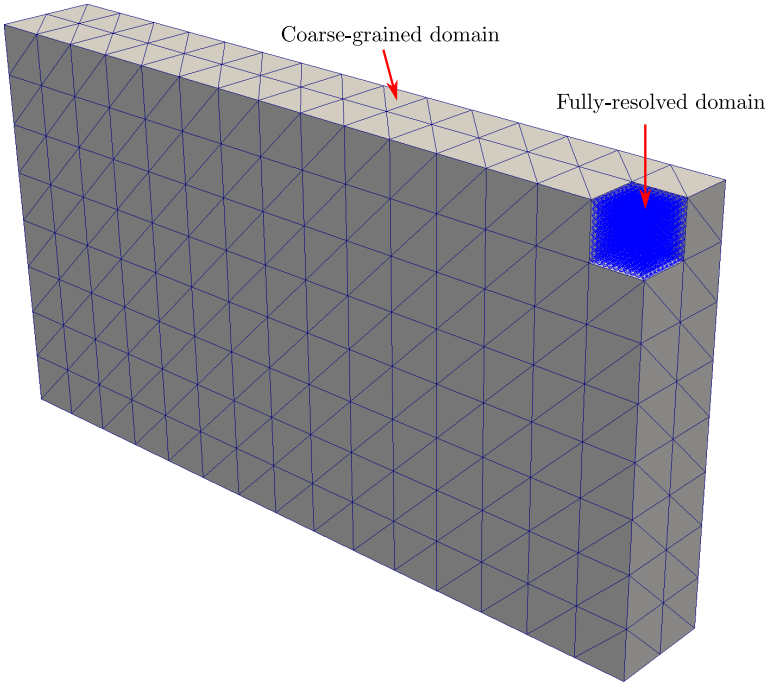

Figure 3.29: Initial discretization for the QC simulation of the Kelvin lattice. The refinement happens in all three spatial directions in comparison to Fig. 3.22.

that the parameters used in Section 3.4.4 [$\kappa_{\text{tol}} = 1.3$, $V_{\text{tol}} = 10\ l_{uc}^3$] were found to cause over-refining for this large Kelvin lattice while the force–displacement curves of the initial few increments remained almost identical with both sets.

Fig. 3.30 plots the curve of the normal contact force versus the tangential displacement of the rigid sphere from AGQC simulation. Note that the force–displacement curve of DNS in Section 3.4.4 is also incorporated in Fig. 3.30 for comparison, sharing a good match, as expected.

Fig. 3.31 illustrates the evolution of KV%, SB% and V_{CGD}% throughout the simulation. In comparison with Fig. 3.27, more significant model reduction is achieved, as expected, since this simulation operates in a model size domain in which QC type of approaches are intended and proved to be useful. Fig. 3.32 plots the discretization of IPEs & FRD as well as the corresponding displacement contour as a function of the location of the rigid sphere. Again, successful adaptation of the IPEs & FRD can be observed and, as opposed to the smaller example of Section 3.4.4, this large model could also be used to tackle deeper scratch simulations with automatic adaptivity for a model size that would be prohibitive for DNS. It is pointed out that in Fig. 3.32 not the whole depth of the lattice is fully resolved compared to that of Fig. 3.28.

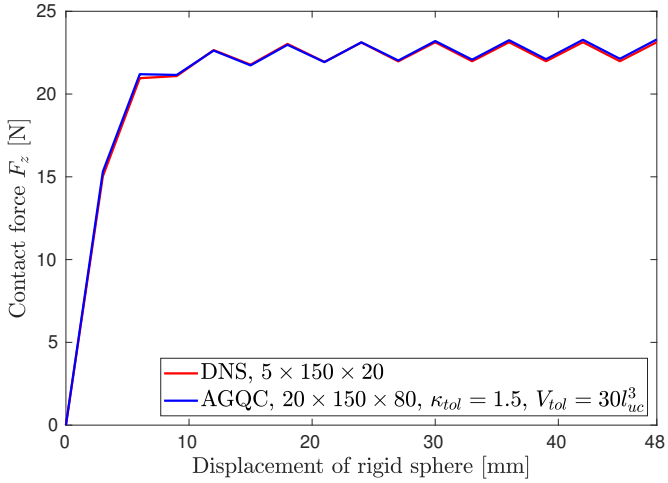

Figure 3.30: The normal contact force versus the tangential displacement of the rigid sphere for the large Kelvin lattice. Only a displacement of up to 48 mm is shown as the trend is apparent.

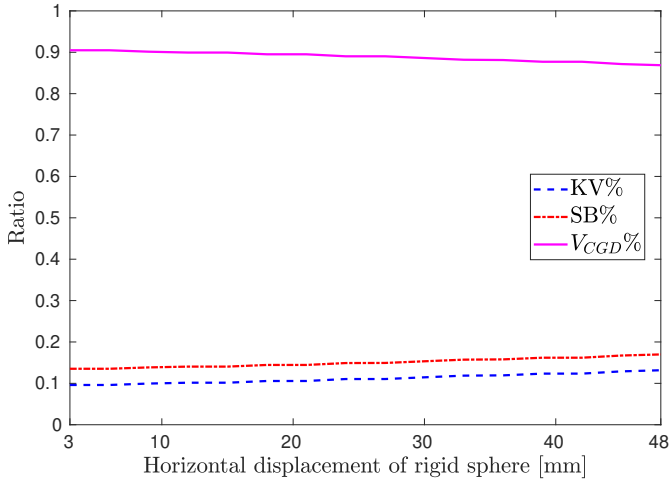

Figure 3.31: Details of the refinement with $\kappa_{\text{tol}} = 1.5$ and $V_{\text{tol}} = 30\ l_{uc}^3$ for the large Kelvin lattice. Only a displacement of up to 48 mm is shown as the trend is apparent.

3.5. Conclusions

This work presented a refinement indicator for adaptive simulations of conventional and generalized quasicontinuum (QC) methods. The refinement indicator is gen-

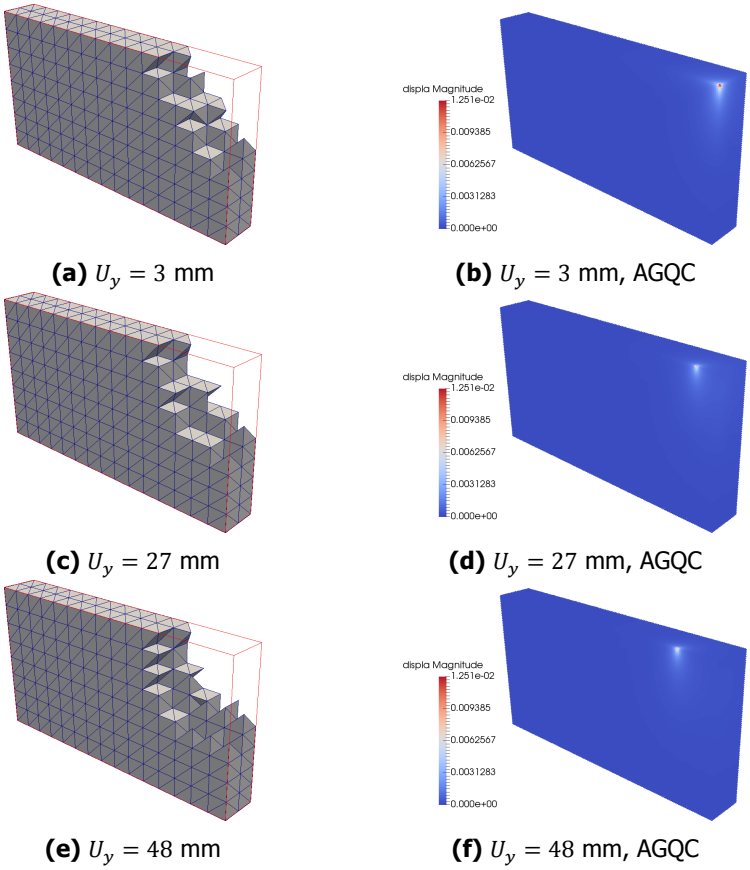

(a) $U_y = 3$ mm **(b)** $U_y = 3$ mm, AGQC

(c) $U_y = 27$ mm **(d)** $U_y = 27$ mm, AGQC

(e) $U_y = 48$ mm **(f)** $U_y = 48$ mm, AGQC

Figure 3.32: Results of the large Kelvin lattice. Left column: the IPEs and the FRDs (void within the red outline) as a function of the displacement (U_y) of the rigid sphere. Middle column: contour of displacement magnitude (i.e. $\sqrt{U_x^2 + U_y^2 + U_z^2}$) of the lattice from adaptive QC simulation.

eral, because it is applicable to all types of lattices without making any assumption about the lattice – albeit dissipation is yet to be accounted for. Our results show that the indicator does not trigger refinement in case of homogeneous deformations, rigid body translations and rigid body rotations (the latter being the result of the co-rotational beam formulation employed in the structural simulations).

The novel refinement indicator measures the discrepancy of the energy of signaling unit cells at interpolation element (IPE) surfaces (or edges in 2D). IPE refinement is triggered when the difference between the energies of a signaling unit cell reaches a user defined threshold, κ_{tol}. If the volume of a newly created IPE falls below a user defined minimum, V_{tol}, the IPE is transformed into a fully resolved domain (FRD). This prompts FRDs to both evolve and be created where necessary.

The examples revealed that the user defined threshold for $[\kappa_{\text{tol}}, V_{\text{tol}}]$ have a fundamental impact on the performance of the adaptive generalized QC method (AGQC) and a procedure for choosing them was proposed.

The proposed AGQC was applied to study BCC lattice and Kelvin lattices. The former showed a more non-local response while the latter exhibited a relatively local structured response. The difference was attributed to the distinct layouts and orientations of the struts in the unit cells. It was also shown that the local response of unit cells favors more significant model reduction when applying AGQC. By simulating two Kelvin lattices of different sizes, it was shown that AGQC is capable of tackling model sizes out of reach of DNS, keeping a satisfactory accuracy by employing an automatic adaptation of the spatial discretization (IPEs in CGDs and FRDs are updated on the fly). It was also demonstrated that the adaptivity parameters $[\kappa_{\text{tol}}, V_{\text{tol}}]$ are case specific and depend on the shape of the unit cell, the beam discretization of the unit cell and the size of the lattice.

Future work will focus on generalizing the indicator to incorporate dissipation (e.g. elastoplastic behavior). Since coarsening can further reduce the computational costs, a new coarsening indicator may also be formulated in the future.

References

[1] J. Knap and M. Ortiz, *An analysis of the quasicontinuum method,* Journal of the Mechanics and Physics of Solids **49**, 1899 (2001), the JW Hutchinson and JR Rice 60th Anniversary Issue.

[2] R. Miller, M. Ortiz, R. Phillips, V. Shenoy, and E. B. Tadmor, *Quasicontinuum models of fracture and plasticity,* Engineering Fracture Mechanics **61**, 427 (1998).

[3] R. E. Miller and E. B. Tadmor, *The quasicontinuum method: Overview, applications and current directions,* Journal of Computer-Aided Materials Design **9**, 203 (2002).

[4] E. B. Tadmor, M. Ortiz, and R. Phillips, *Quasicontinuum analysis of defects in solids,* Philosophical Magazine A **73**, 1529 (1996), https://doi.org/10.1080/01418619608243000 .

[5] E. B. Tadmor, R. Phillips, and M. Ortiz, *Mixed atomistic and continuum models of deformation in solids,* Langmuir **12**, 4529 (1996), https://doi.org/10.1021/la9508912 .

[6] M. Arndt, V. Sorkin, and E. Tadmor, *Efficient algorithms for discrete lattice calculations,* Journal of Computational Physics **228**, 4858 (2009).

[7] D. M. Kochmann and J. S. Amelang, *The quasicontinuum method: Theory and applications,* in *Multiscale Materials Modeling for Nanomechanics*, Vol. 245, edited by C. R. Weinberger and G. J. Tucker (Springer International Publishing, Cham, Switzerland, 2016) Chap. 8, pp. 159–193.

[8] M. Luskin and C. Ortner, *An analysis of node-based cluster summation rules in the quasicontinuum method,* SIAM Journal on Numerical Analysis **47**, 3070 (2009), https://doi.org/10.1137/080743391 .

[9] M. Luskin, C. Ortner, and B. V. Koten, *Formulation and optimization of the energy-based blended quasicontinuum method,* Computer Methods in Applied Mechanics and Engineering **253**, 160 (2013).

[10] B. Van Koten, X. H. Li, M. Luskin, and C. Ortner, *A computational and theoretical investigation of the accuracy of quasicontinuum methods,* in *Numerical Analysis of Multiscale Problems*, edited by I. G. Graham, T. Y. Hou, O. Lakkis, R. Scheichl, I. G. Graham, T. Y. Hou, O. Lakkis, and R. Scheichl (Springer Berlin Heidelberg, Berlin, Heidelberg, 2012) pp. 67–96.

[11] Y. Zhang and M. Gunzburger, *Quadrature-rule type approximations to the quasicontinuum method for long-range interatomic interactions,* Computer Methods in Applied Mechanics and Engineering **199**, 648 (2010).

[12] L. A. A. Beex, R. H. J. Peerlings, and M. G. D. Geers, *A multiscale quasicontinuum method for dissipative lattice models and discrete networks,* Journal of the Mechanics and Physics of Solids **64**, 154 (2014).

[13] L. A. A. Beex, R. H. J. Peerlings, K. van Os, and M. G. D. Geers, *The mechanical reliability of an electronic textile investigated using the virtual-power-based quasicontinuum method,* Mechanics of Materials **80**, 52 (2015).

[14] L. A. A. Beex, R. H. J. Peerlings, and M. G. D. Geers, *A multiscale quasicontinuum method for lattice models with bond failure and fiber sliding,* Computer Methods in Applied Mechanics and Engineering **269**, 108 (2014).

[15] O. Rokoš, L. A. A. Beex, J. Zeman, and R. H. J. Peerlings, *A variational formulation of dissipative quasicontinuum methods,* International Journal of Solids and Structures **102-103**, 214 (2016).

[16] O. Rokoš, R. H. J. Peerlings, and J. Zeman, *eXtended variational quasicontinuum methodology for lattice networks with damage and crack propagation,* Computer Methods in Applied Mechanics and Engineering **320**, 769 (2017).

[17] O. Rokoš, R. H. J. Peerlings, J. Zeman, and L. A. A. Beex, *An adaptive variational quasicontinuum methodology for lattice networks with localized damage,* International Journal for Numerical Methods in Engineering **112**, 174 (2017), https://onlinelibrary.wiley.com/doi/pdf/10.1002/nme.5518 .

[18] K. Mikeš, O. Rokoš, and R. H. J. Peerlings, *Molecular statics simulation of nanoindentation using adaptive quasicontinuum method,* in *Acta Polytechnica CTU Proceedings*, Vol. 15 (Czech Technical University in Prague, 2018).

[19] K. Mikeš and M. Jirásek, *Quasicontinuum simulation of nanotextile based on the microplane model,* in *Proceedings of the 17th Conference on the Rehabilitation and Reconstruction of Buildings (CRRB 2015)*, Key Engineering Materials, Vol. 714 (Trans Tech Publications Ltd, 2016) pp. 143–147.

[20] K. Mikeš and M. Jirásek, *Quasicontinuum method combined with anisotropic microplane model,* in *Modern Methods of Experimental and Computational Investigations in Area of Construction II*, Advanced Materials Research, Vol. 1144 (Trans Tech Publications Ltd, 2017) pp. 142–147.

[21] K. Mikeš and M. Jirásek, *Quasicontinuum method extended to irregular lattices,* Computers & Structures **192**, 50 (2017).

[22] A. Ghareeb and A. Elbanna, *An adaptive quasicontinuum approach for modeling fracture in networked materials: Application to modeling of polymer networks,* Journal of the Mechanics and Physics of Solids **137**, 103819 (2020).

[23] L. Chen, L. A. Beex, P. Z. Berke, T. J. Massart, and S. P. Bordas, *Generalized quasicontinuum modeling of metallic lattices with geometrical and material nonlinearity and variability,* Computer Methods in Applied Mechanics and Engineering **366**, 112878 (2020).

[24] G. P. Phlipot and D. M. Kochmann, *A quasicontinuum theory for the nonlinear mechanical response of general periodic truss lattices,* Journal of the Mechanics and Physics of Solids **124**, 758 (2019).

[25] P. Z. Berke, R. H. J. Peerlings, T. J. Massart, and M. G. D. Geers, *A homogenization-based quasi-discrete method for the fracture of heterogeneous materials,* Computational Mechanics **53**, 909 (2014).

[26] M. G. D. Geers, V. G. Kouznetsova, and W. A. M. Brekelmans, *Multi-scale computational homogenization: Trends and challenges,* Journal of Computational and Applied Mathematics **234**, 2175 (2010), fourth International Conference on Advanced COmputational Methods in ENgineering (ACOMEN 2008).

[27] T. J. Massart, R. H. J. Peerlings, and M. G. D. Geers, *Structural damage analysis of masonry walls using computational homogenization,* International Journal of Damage Mechanics **16**, 199 (2007), https://doi.org/10.1177/1056789506064943 .

[28] P. Kerfriden, J. J. Ródenas, and S. P. A. Bordas, *Certification of projection-based reduced order modelling in computational homogenisation by the constitutive relation error,* International Journal for Numerical Methods in Engineering **97**, 395 (2014), https://onlinelibrary.wiley.com/doi/pdf/10.1002/nme.4588 .

[29] A. Memarnahavandi, F. Larsson, and K. Runesson, *A goal-oriented adaptive procedure for the quasi-continuum method with cluster approximation,* Computational Mechanics **55**, 617 (2015).

[30] I. Tembhekar, J. S. Amelang, L. Munk, and D. M. Kochmann, *Automatic adaptivity in the fully nonlocal quasicontinuum method for coarse-grained atomistic simulations,* International Journal for Numerical Methods in Engineering **110**, 878 (2017), https://onlinelibrary.wiley.com/doi/pdf/10.1002/nme.5438 .

[31] S. Kwon, Y. Lee, J. Y. Park, D. Sohn, J. H. Lim, and S. Im, *An efficient three-dimensional adaptive quasicontinuum method using variable-node elements,* Journal of Computational Physics **228**, 4789 (2009).

[32] M. Dobson, R. S. Elliott, M. Luskin, and E. B. Tadmor, *A multilattice quasicontinuum for phase transforming materials: Cascading cauchy born kinematics,* Journal of Computer-Aided Materials Design **14**, 219 (2007).

[33] L. A. A. Beex, R. H. J. Peerlings, and M. G. D. Geers, *Central summation in the quasicontinuum method,* Journal of the Mechanics and Physics of Solids **70**, 242 (2014).

[34] L. A. A. Beex, P. Kerfriden, T. Rabczuk, and S. P. A. Bordas, *Quasicontinuum-based multiscale approaches for plate-like beam lattices experiencing in-plane and out-of-plane deformation,* Computer Methods in Applied Mechanics and Engineering **279**, 348 (2014).

[35] L. A. A. Beex, R. H. J. Peerlings, and M. G. D. Geers, *A quasicontinuum methodology for multiscale analyses of discrete microstructural models,* International Journal for Numerical Methods in Engineering **87**, 701 (2011), https://onlinelibrary.wiley.com/doi/pdf/10.1002/nme.3134 .

[36] L. A. A. Beex, O. Rokoš, J. Zeman, and S. P. A. Bordas, *Higher-order quasicontinuum methods for elastic and dissipative lattice models: uniaxial deformation and pure bending,* GAMM-Mitteilungen **38**, 344 (2015), https://onlinelibrary.wiley.com/doi/pdf/10.1002/gamm.201510018 .

[37] J. M. Battini and C. Pacoste, *Co-rotational beam elements with warping effects in instability problems,* Computer Methods in Applied Mechanics and Engineering **191**, 1755 (2002).

[38] D. M. Kochmann and G. N. Venturini, *A meshless quasicontinuum method based on local maximum-entropy interpolation,* Modelling and Simulation in Materials Science and Engineering **22**, 034007 (2014).

[39] P. Kerfriden, O. Goury, T. Rabczuk, and S. P. A. Bordas, *A partitioned model order reduction approach to rationalise computational expenses in nonlinear fracture mechanics,* Computer Methods in Applied Mechanics and Engineering **256**, 169 (2013).

[40] J. P. Suárez, P. Abad, A. Plaza, and M. A. Padrón, *Computational aspects of the refinement of 3d tetrahedral meshes,* Journal of Computational Methods in Sciences and Engineering **5**, 215 (2005).

[41] M. Smith, Z. Guan, and W. J. Cantwell, *Finite element modelling of the compressive response of lattice structures manufactured using the selective laser melting technique,* International Journal of Mechanical Sciences **67**, 28 (2013).

[42] J. M. Battini and C. Pacoste, *Plastic instability of beam structures using co-rotational elements,* Computer Methods in Applied Mechanics and Engineering **191**, 5811 (2002).

[43] D. Durville, *Simulation of the mechanical behaviour of woven fabrics at the scale of fibers,* International Journal of Material Forming **3**, 1241 (2010).

[44] A. Gay Neto, P. M. Pimenta, and P. Wriggers, *A master-surface to master-surface formulation for beam to beam contact. part i: frictionless interaction,* Computer Methods in Applied Mechanics and Engineering **303**, 400 (2016).

[45] J. Lengiewicz, J. Korelc, and S. Stupkiewicz, *Automation of finite element formulations for large deformation contact problems,* International Journal for Numerical Methods in Engineering **85**, n/a (2010).

[46] M. Magliulo, A. Zilian, and L. A. A. Beex, *Contact between shear-deformable beams with elliptical cross sections,* Acta Mechanica **231**, 273 (2020).

[47] P. Wriggers, *Computational Contact Mechanics* (Springer Berlin Heidelberg, Berlin, Heidelberg, 2006).

4

An adaptive multiscale quasicontinuum approach for mechanical simulations of elastoplastic periodic lattices*

In this chapter, an essential extension of the adaptive generalized quasicontinuum method (AGQC) of Chapter 3 for elastoplastic lattices is presented. The extension is based on restricting plasticity to the fully-resolved domains (FRDs) of the AGQC model. This extension is achieved by raising a plastic flag for an interpolation element (IPE) in the AGQC model if any sampling beam of the IPE experiences plastic deformation. Once a plastic flag is active, the corresponding IPE is directly transformed into a FRD. Illustrative numerical examples for a scratch test of an elastoplastic a Kelvin lattice demonstrate the capabilities of the resulting framework.

* In preparation for submission to Computational Mechanics.

4.1. Introduction

Metallic periodic lattices [1] have attracted more and more attention due to the progress in additive manufacturing and their outstanding mechanical properties (e.g. high strength-to-weight ratio, excellent energy absorption property). Topologically, a periodic lattice is organized by repeating a unit cell in three spatial directions. The unit cell consists of struts with a diameter that may desirably and/or undesirably vary in the struts' axial direction. Undesirable diameter variations for instance appear if selective laser melting is employed as the manufacturing process – in that case, the diameter is larger at the struts' extremities where the struts are connected to each other [2]. Experiments [3, 4] have attributed the failure of metallic periodic lattices to local nonlinear effects such as elastic and plastic buckling of individual struts, which progress in plasticity and ultimately in failure observable at the macroscale.

Finite element analysis (FEA) is widely applied for modeling/predicting the mechanical response of metallic periodic lattices. In FEA, the modeling work consists of discretizing the struts of lattices by finite elements (FEs) and employing the appropriate constitutive model for the problem at hand (e.g. elasticity, elastoplasticity and damage) [5–13]. Particularly useful for moderate to medium sized problems are beam FE models because of their computational efficiency, necessary for tackling multi millions strut problems. The main challenge of applying full FEA to model lattices (referred to as direct numerical simulation or DNS) remains the associated prohibitive computational cost for engineering scale problems. This drawback is obviously even more critical if a nonlinear structural response is considered, independently of the solution scheme, restricting the field of application of nonlinear DNS to small lattice volumes.

To simulate the nonlinear mechanical behavior of periodic lattices at the scale of products, model reduction is unavoidable. Thanks to the periodicity of lattices and the fact that localized straining/failure is most often observed, concurrent multiscale methods can be exploited. In particular, the quasicontinuum method (QC) is a promising solution because QC makes use of small fully-resolved domains (FRDs) to track localized deformation/failure, and coarse-grained domains (CGDs) in zones undergoing more homogeneous deformation for computational efficiency. The work of [14–17] extends classical QC (proposed for conservative atomic lattices) to simulate truss lattices (i.e. structural lattices) with dissipative mechanisms (e.g. elastoplasticity, damage). Until recently, the main bottleneck of this approach was that only a single FE (beam, spring) could be used to represent a strut. As a result, varying cross sections could not be represented. This limitation was mitigated in [18], which generalized QC (the resulting method is termed as GQC) with a multi-field interpolation feature. Consequently, each strut can currently be more realistically modeled using a string of beam FEs with varying diameters.

Adaptivity (i.e. adjustment of the spatial reduction of the QC method based on the deformation) is crucial if the (local) deformation spatially evolve during simulations. In Chapter 3, an adaptive version of GQC (termed as AGQC), which exploits a novel refinement indicator to refine CGDs and transform CGDs into FRDs, was proposed and critically assessed for elastic beams with geometrical nonlinearities.

The capabilities and limitations of the refinement indicator for elastoplastic (geometrically nonlinear) beams have however not been investigated.

The main focus of this chapter is therefore the extension of the adaptive GQC (AGQC) framework of Chapter 3 towards elastoplastic lattice behavior. This extension significantly widens the applicability of AGQC: for metallic periodic lattices it would for instance yield more realistic lattice response predictions. Note that this chapter (similar to Chapter 3) only focuses on refinement of the spatial representation. In other words, coarsening, i.e. the FRD → CGD transition, is not considered here, being part of future work.

The structure of this contribution is as follows: in Section 4.2, the key concepts of AGQC are briefly revisited as to make this chapter self-contained. In Section 4.3, the development of AGQC for elastoplastic lattices is presented; the justification for employing a different elastoplastic beam FE than in Chapter 3 is also provided (although the proposed AGQC remains independent of the underlying FE formulation). In Section 4.4, a numerical example is used to assess the proposed AGQC scheme. This is followed by conclusions drawn in Section 4.5, together with an outlook on future work.

4.2. Summary of AGQC concepts

This section gives a brief recap of the generalized quasicontinuum method (GQC). A periodic lattice structure of which the struts are discretized using beam FEs is considered and it is subjected to external forces. Let $\mathbf{u}$ and $\mathbf{f}_{\text{ext}}$ denote the column matrices storing the kinematic variables of beam nodes and the corresponding external forces, respectively. Let $\boldsymbol{z}$ denote the column matrix that stores the plastic strain history variables of all beam FEs. The direct numerical simulation (DNS) of the lattice is performed by solving the following equations using Newton's method:

$$\delta\mathbf{u}^T(\mathbf{f}_{\text{int}}(\mathbf{u}^*,\boldsymbol{z}^*)+\mathbf{K}(\mathbf{u}^*,\boldsymbol{z}^*)d\mathbf{u})=\delta\mathbf{u}^T\mathbf{f}_{\text{ext}} \tag{4.1}$$

where $\mathbf{u}^*$ denotes an estimate of $\mathbf{u}$, $d\mathbf{u}$ represents the correction of $\mathbf{u}$. $\boldsymbol{z}^*$ denotes an estimation of $\boldsymbol{z}$. $d\mathbf{u}$ is fed into the plasticity theory to generate an correction of $\boldsymbol{z}$. $\mathbf{f}_{\text{int}}(\mathbf{u},\boldsymbol{z})$ denotes the column of internal forces and is obtained as:

$$\mathbf{f}_{\text{int}}(\mathbf{u},\boldsymbol{z})=\sum_{i=1}^{m}\int_{V_i}\sigma(\mathbf{u},\boldsymbol{z})dV \tag{4.2}$$

with m representing the total number of beam FEs in the lattice. V_i and σ are the volume and stress tensor of beam i, respectively. $\mathbf{K}$ denotes the tangential stiffness matrix and is obtained as:

$$\mathbf{K}(\mathbf{u},\boldsymbol{z})=\sum_{i=1}^{m}\int_{V_i}\frac{\partial\sigma(\mathbf{u},\boldsymbol{z})}{\partial\mathbf{u}}dV \tag{4.3}$$

The DNS is computationally too expensive to model large periodic lattices because (1) the large number of DoFs involved; (2) the large amount of beam FEs

which need to be visited to construct Eq. (4.2) and Eq. (4.3) in Newton's incremental-iterative procedure. The GQC proposed in Chapter 2 is a promising alternative to DNS by mitigating the computational cost and maintaining a satisfactory accuracy. GQC performs model reduction in two steps, i.e. *interpolation* and *summation*.

Interpolation divides the lattice into fully-resolved domains (FRDs) and coarse-grained domains (CGDs). In the FRDs, all the kinematic variables of the beam nodes (i.e. displacements and rotations) are preserved. In the CGDs, a mesh of interpolation elements (IPEs) is introduced so that only a few representative kinematic variables are allocated to the IPE nodes. The kinematic variables of all beam nodes within an IPE are interpolated from their representative counterparts at the IPE nodes using FE shape functions. Moreover, the beam nodes are categorized into different groups based on periodicity. The IPE nodes store a set of representative kinematic variables for each type of beam node so as to interpolate the kinematic variables of corresponding type of beam node independently. Fig. 4.1 represents a lattice with a $\times$ shaped unit cell with a GQC spatial representation. After interpolation, the preserved kinematic variables (i.e. the displacements and rotations of the beam nodes in the FRDs and the representative displacements and rotations of all node types at the IPE nodes) are stored in column matrix $\mathbf{u}_\mathrm{r}$, which can be related to $\mathbf{u}$ via interpolation matrix $\mathbf{N}$ through

$$\mathbf{u} = \mathbf{N}\mathbf{u}_\mathrm{r}. \tag{4.4}$$

After interpolation, Eq. (4.1) is revised as

$$\delta\mathbf{u}_\mathrm{r}^T(\mathbf{N}^T\mathbf{f}_\mathrm{int}(\mathbf{N}\mathbf{u}_\mathrm{r}^*, \boldsymbol{z}^*) + \mathbf{N}^T\mathbf{K}(\mathbf{N}\mathbf{u}_\mathrm{r}^*, \boldsymbol{z}^*)\mathbf{N}d\mathbf{u}_\mathrm{r}) = \delta\mathbf{u}_\mathrm{r}^T\mathbf{N}^T\mathbf{f}_\mathrm{ext} \tag{4.5}$$

with $\mathbf{u}_\mathrm{r}^*$ denoting an estimate of $\mathbf{u}_\mathrm{r}$ and $d\mathbf{u}_\mathrm{r}$ the correction of $\mathbf{u}_\mathrm{r}$.

In *summation*, rather than visiting all beam FEs in the lattice according to Eqs. (4.2) and (4.3), only a selection of beam FEs are sampled to approximate $\mathbf{f}_\mathrm{int}$ and $\mathbf{K}$:

$$\tilde{\mathbf{f}}_\mathrm{int}(\mathbf{u}_\mathrm{s}, \boldsymbol{z}_\mathrm{s}) = \sum_{i\in S}\omega_i\int_{V_i}\sigma(\mathbf{u}_\mathrm{s}, \boldsymbol{z}_\mathrm{s})dV \tag{4.6}$$

$$\tilde{\mathbf{K}}(\mathbf{u}_\mathrm{s}, \boldsymbol{z}_\mathrm{s}) = \sum_{i\in S}\omega_i\int_{V_i}\frac{\partial\sigma(\mathbf{u}_\mathrm{s}, \boldsymbol{z}_\mathrm{s})}{\partial\mathbf{u}_\mathrm{s}}dV \tag{4.7}$$

where S denotes the set of sampling beams, ω_i denotes the weight of sampling beam i, and $\mathbf{u}_\mathrm{s}$ the column matrix that stores the kinematic variables of the nodes of the sampling beams. $\boldsymbol{z}_\mathrm{s}$ represents the column matrix that stores the plastic strain history variables of all sampling beam FEs. Note that $\mathbf{u}_\mathrm{s}$ can be interpolated from $\mathbf{u}_\mathrm{r}$ using interpolation matrix $\mathbf{N}_\mathrm{s}$,

$$\mathbf{u}_\mathrm{s} = \mathbf{N}_\mathrm{s}\mathbf{u}_\mathrm{r}. \tag{4.8}$$

The governing equations of Eq. (4.5) can then be further revised as

$$\delta\mathbf{u}_\mathrm{r}^T(\mathbf{N}_\mathrm{s}^T\tilde{\mathbf{f}}_\mathrm{int}(\mathbf{N}_\mathrm{s}\mathbf{u}_\mathrm{r}^*, \boldsymbol{z}_\mathrm{s}^*) + \mathbf{N}_\mathrm{s}^T\tilde{\mathbf{K}}(\mathbf{N}_\mathrm{s}\mathbf{u}_\mathrm{r}^*, \boldsymbol{z}_\mathrm{s}^*)\mathbf{N}_\mathrm{s}d\mathbf{u}_\mathrm{r}) = \delta\mathbf{u}_\mathrm{r}^T\mathbf{N}^T\mathbf{f}_\mathrm{ext}. \tag{4.9}$$

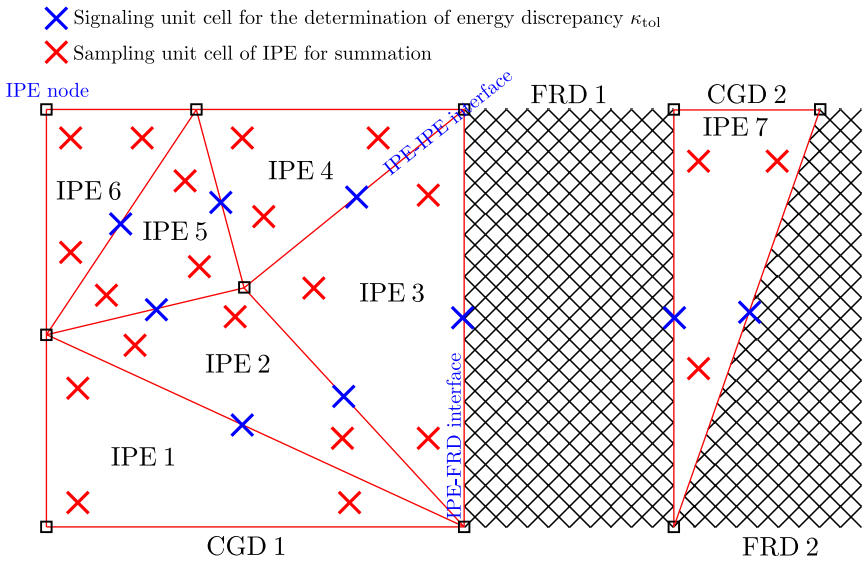

Figure 4.1: Illustration of key concepts of adaptive GQC method.

The reader is referred to Section 2.2.2 for details on how the sampling beams and their weights are selected in this thesis.

In order to trace the evolution of localized deformation/failure, an adaptive GQC (AGQC) framework was proposed in Chapter 3 for elastic periodic lattices. Elastic AGQC is based on monitoring a sum of energy discrepancies, κ, at IPE-IPE interfaces and IPE-FRD interfaces using signalling unit cells (See Fig. 4.1). The calculation of κ is detailed in Section 3.3 and is not repeated here for the sake of brevity. Within each increment, whenever the GQC model is equilibrated by solving Eq. (4.9), κ is evaluated for all IPE-IPE/IPE-FRD interfaces and compared to user defined threshold κ_{tol}. If the κ of an IPE-IPE interface exceeds κ_{tol}, the associated IPEs are refined into smaller IPEs. If the volume of the refined IPEs are smaller than user defined volume threshold V_{tol}, the associated IPEs are transformed into FRDs instead. If the κ of an IPE-FRD interface exceeds κ_{tol}, the associated IPEs are directly transformed into FRDs.

Either the refinement of IPEs or the transformation of IPEs into FRDs prompts the governing equations of Eq. (4.9) to be solved again for the current increment with the new GQC spatial representation in a so-called re-equilibration step.

4.3. Adaptive GQC scheme for elastoplastic periodic cellular lattices

This section upgrades the adaptive generalized quasicontinuum method (AGQC) of Chapter 3 so that elastoplastic behavior can be considered in lattices. The presented work thus combines the work in Chapter 2 (generalized QC for elastoplastic

behavior) and Chapter 3 (adaptive generalized QC for elastic behavior). The adaptive scheme is based on the novel refinement indicator of Chapter 3, complemented by a plastic flag. Note that the proposed AGQC scheme is of course independent from the used beam FE formulation (technical details may differ for the detection of plastic strain).

Each lattice strut is modeled using a string of elastoplastic 3D co-rotational beam FEs, for which the plasticity is implemented here through cross sectional discretization and a multi-axial yield surface [19]. Employing a different beam FE from Chapter 2 is motivated by its superior convergence rate compared to the embedded plastic hinge model of Chapter 2. For the embedded plastic hinge FE a consistent stiffness relationship cannot be formulated for general loading. The reason for this is that in the local coordinate frame, the nodal rotation of the 3D co-rotational framework is represented using a rotation vector. On the other hand, the embedded plastic hinge model requires the angular rotations as variables to evaluate the corresponding internal forces. Instead of deriving a rigorous transformation between the rotation vector and the angular rotations they are approximated to be equal. Such an approximation breaks the consistency of the tangential stiffness relationship, which is detrimental for the convergence rate (generally observed to be linear).

On the contrary, the new beam FE implementation [19] ensures a quadratic convergence rate in the implicit Newton scheme used in this work. The beam FE is assumed with a constant circular cross section. To avoid shear locking for the Timoshenko beam FE, integration points are seeded in only one cross section (i.e. the central cross section). 100 quadrature points are used in the circular beam cross section at which the elastoplastic stress update takes place (See Fig. 4.2). For more details about the Gauss quadrature rules in a circular domain, readers are referred to [20]. The 3D co-rotational framework elaborated in Section 2.3.1 decouples the overall beam motion (i.e. the nodal displacements and rotations at the beam ends in the global coordinate frame) into a rigid body movement (i.e. the displacements and rotations of the local coordinate frame) and a pure deformation (i.e. the displacements and rotations at the beam ends in the local coordinate frame). The displacements and rotations at the beam ends in the local coordinate frame are then used to interpolate the normal and shear strains at each integration points of the central cross section. Afterwards, a backward Euler scheme is used to enforce the incremental plastic flow and consistency condition with a von Mises's yield criterion. Once the stress components and the tangential material stiffness of each integration point are obtained from the return mapping procedure, they are integrated to generate the internal forces and the consistent stiffness relationship. For more details of the formulation, readers are referred to [19].

4.3.1. Specific features of elastoplastic AGQC

It is emphasized that in AGQC, new sampling beams emerge when the spatial representation of GQC is adjusted in the refinement process. The newly introduced sampling beams emerge from (1) the sampling unit cells of the refined IPEs and (2) the IPEs that are transformed into FRDs.

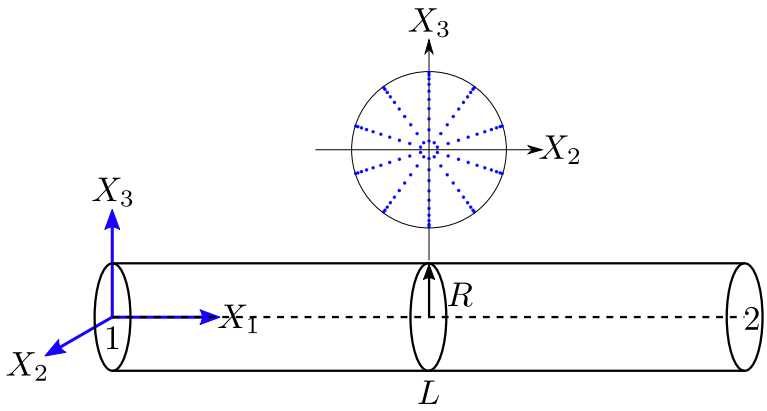

Figure 4.2: The integration scheme of the beam finite element. $\mathbf{X}_1$, $\mathbf{X}_2$, $\mathbf{X}_3$ span the local coordinate frame. Along the beam length direction, only the middle cross section is used for integration. In the central cross section, 100 Gauss quadrature points (×) are adopted.

Evaluating the internal forces and the tangential stiffness for these new sampling beams is required to solve the governing equations in Eq. (4.9). In case of elasticity, the evaluation of the internal forces and the tangential stiffness is independent of the deformation history. Consequently, in the elastic AGQC of Chapter 3, retrieving the internal forces and the tangential stiffness of new sampling beams is simple and performed in two steps: interpolating their kinematic variables (i.e. the initial guess) and re-equilibrating the unbalanced structural system by performing the structural computation of the current increment again with the updated spatial discretization. It is useful to note that this re-equilibration step was observed to always converge thanks to the history-independent behavior allowing for easy stress redistribution in the lattice. In case of elastoplasticity, the evaluation of the internal forces and the tangential stiffness is dependent on the cumulative plastic strain history variables that can only grow to remain physically acceptable.

Recall that the new sampling beams of AGQC come from either newly refined interpolation elements (IPEs) in CGDs or IPEs in CGDs that are transformed into FRDs. In both cases, the new sampling beams emerge from CGDs. This prompts two approaches to tackle plasticity in AGQC. The first is to allow plasticity in CGDs, in which case a carefully designed transfer of history variables is necessary. The second is to restrict plasticity to FRDs only, for which the transfer of history variables is circumvented and new sampling beams emerging from CGDs are presumed to be elastic before the re-equilibration step.

To assess the first approach, i.e. *to allow plasticity in CGDs*, uniaxial compression of an elastoplastic BCC lattice is considered first. Fig. 4.3 shows both the DNS and GQC results of a $12 \times 12 \times 12$ BCC lattice (comprising a volume of $24 \times 24 \times 24$ mm^3) under unconstrained uni-axial compression (see Section 3.3.4 for the geometrical configuration and the cross sections of BCC unit cell). The nominal

strain in the direction of compression in this example amounts to 20%, defined as $\epsilon_z = U_z/L_z \times 100\%$. Beyond this strain local buckling in the CGD sampling unit cell would occur and at much. At large compression strains (e.g. above 50%), the lattice enters the stage of densification where the inter-strut contact plays an important role. In that case the legitimacy of the current model is questionable because of the assumption of periodicity and smooth, non-localized strains supposed in the CGDs. The material parameters in all simulations in this chapter are: Young's modulus of 97 GPa, Poisson's ratio of 0.3, an initial yield stress of 325 MPa and a hardening modulus of 9.7 GPa. Linear hardening and the von Mises's yield criterion are employed.

The compression example in Fig. 4.3 shows that GQC can accurately capture the force–displacement curve (the defection at the displacement of 2.88 mm is to be investigated in future work), but *fails to capture the deformation localization* in Fig. 4.3b if plasticity in CGD is allowed. In further efforts aiming at plastic CGD-to-FRD transformation through transferring plastic strain history variables (one per cross sectional quadrature point) between sampling beams, the above led to significant convergence issues. It is believed that the lack of convergence is related to a failure of redistributing stresses from the homogeneously deformed plastic CGD pattern to an FRD pattern. Such a redistribution is expected to show strain localization at CGD-to-FRD transformation, while respecting the requirement of the monotonous increase of the accumulated plastic strain history variable. For these reasons, the framework of this chapter forbids the development of plasticity in CGDs. An extension of the framework in which plasticity can develop in CGDs may be part of future work.

Plasticity is thus restricted in the following to FRDs only. Because plasticity should more often than not be treated as a localized phenomenon in metal lattices (see strain localization in Fig. 4.3b), this option corresponds well to the fundamental idea of classical QC utilizing FRDs to trace localized deformation/failure. Under the assumption of restricting plasticity to FRDs, the adaptive scheme of Chapter 3 (see Section 3.3.3) was revised as Alg. 3 to account for elastoplasticity. The glossary of the symbols that are involved in the pseudo codes of Alg. 3 and its subroutine (i.e. Alg. 4) is in Table 3.2. The same definitions of the refinement indicator κ and the refinement of spatial discretization (IPE → smaller IPE; IPE → FRD) are used as given in Section 3.3.1 and 3.3.2 and are not recalled here for the sake of brevity.

Alg. 3 starts from an initial division of FRDs (i.e. Ω_0^{FRD}, does not exist when no FRD is assigned) and CGDs (i.e. Ω_0^{CGD}), the initial mesh of IPEs in the CGDs (i.e. τ_0) and the initial selection of sampling beams (i.e. S^0). The initial configuration is undeformed and stress-free.

For a given increment, t_k, the GQC model of the last converged increment, t_{k-1}, is preserved as the starting point of t_k (i.e. $\Omega_k^{\text{FRD}} \Leftarrow \Omega_{k-1}^{\text{FRD}}$, $\Omega_k^{\text{CGD}} \Leftarrow \Omega_{k-1}^{\text{CGD}}$, $\tau_k \Leftarrow \tau_{k-1}$ and $S^k \Leftarrow S^{k-1}$). Moreover, the kinematic variables and internal forces of the last converged increment (i.e. $\mathbf{u}_{\text{r}}^{k-1}$ and $\mathbf{f}_{\text{int}}^{k-1}$) serve as the initial guesses for their counterparts at t_k. The boundary conditions (BCs) at t_k (i.e. $\partial\Omega_k^{\text{FRD}}$ for BCs on Ω_k^{FRD}, $\partial\Omega_k^{\text{CGD}}$ for BCs on Ω_k^{CGD}) are also imposed. The obtained GQC model is then solved for the equilibrium equations in Eq. (4.9).

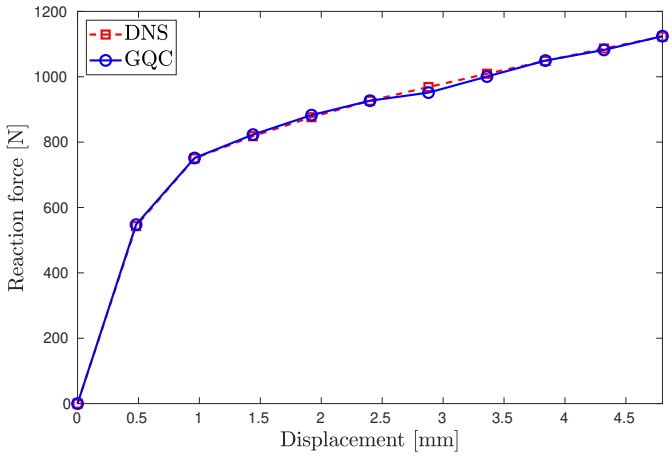

(a) Force–displacement curve.

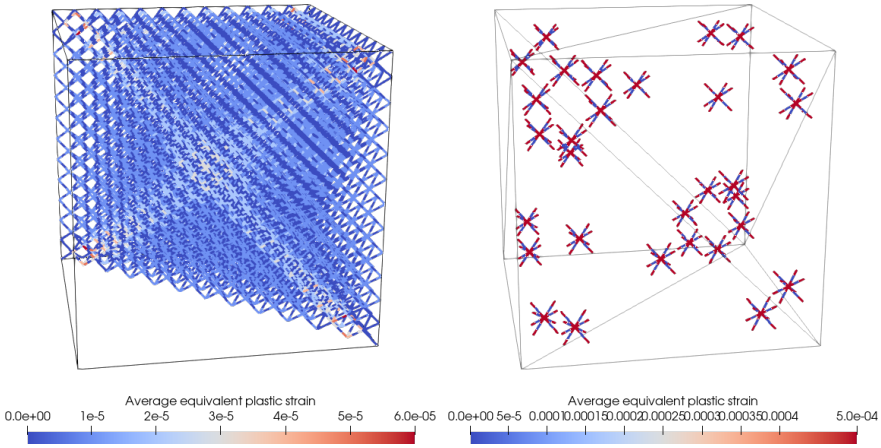

(b) Diagonal cut contour plot of averaged plastic strain of beams in DNS with sample compression strain of 0.2.

(c) Contour of averaged plastic strain of sampling beams in GQC with sample compression strain of 0.2.

Figure 4.3: Unconstrained vertical compression of a BCC lattice modeled using elastoplastic 3D co-rotational beam FEs.

Once the GQC model is in equilibrium after solving Eq. (4.9), it goes through three loops successively, i.e. Loop 1 (lines 6–10 in Alg. 3), Loop 2 (lines 11–15 in Alg. 3) and Loop 3 (lines 16–20 in Alg. 3). The three loops are identical, except for the different criteria that are applied to determine the target IPEs for refinement and a minor difference of refinement strategies. Loop 1 checks the sampling beams of all IPEs and targets the IPEs with plastified sampling beams for full resolution: IPEs flagged for plasticity are not refined but always transformed into FRDs. Loop

2 on the other hand checks the energy discrepancy, κ for IPE-IPE interfaces and flags the IPEs with $\kappa > \kappa_{\text{tol}}$ for refinement: IPEs to smaller IPEs and the refined IPEs with smaller volumes than V_{tol} are transformed into FRDs. Loop 3 checks the energy discrepancy, κ for IPE-FRD interfaces and flags the IPEs with $\kappa > \kappa_{\text{tol}}$ for full resolution.

Either the full resolution (Loop 1 & 3) or the IPE refinement (Loop 2) generates a refined GQC model with new division of FRDs ($\Omega_{k^*}^{\text{FRD}}$) and CGDs ($\Omega_{k^*}^{\text{CGD}}$), a new mesh of IPEs in CGDs (τ_{k^*}) and a new selection of sampling beams (S^{k^*}). This also creates new kinematic variables ($\mathbf{u}_{\text{r}}^{k^*}$) and corresponding internal forces ($\mathbf{f}_{\text{int}}^{k^*}$). Note that such a refined but not yet equilibrated GQC model at t_k is characterized by subscript/superscript k^* in order to distinguish it from the GQC model in equilibrium.

The refined GQC model is generally no longer in equilibrium, and structural equilibrium needs to be found for the new spatial discretization by solving again Eq. (4.9). First, the initial guesses of $\mathbf{u}_{\text{r}}^{k^*}$ and $\mathbf{f}_{\text{int}}^{k^*}$ are required. An interpolation matrix $\Phi_{k^*}^{k-1}$ between $\mathbf{u}_{\text{r}}^{k-1}$ and $\mathbf{u}_{\text{r}}^{k^*}$ is constructed (in the same manner as constructing $\mathbf{N}$ in Eq. (4.4)) so that the initial guess of $\mathbf{u}_{\text{r}}^{k^*}$ is set to $\Phi_{k^*}^{k-1}\,\mathbf{u}_{\text{r}}^{k-1}$. As for the initial guess of $\mathbf{f}_{\text{int}}^{k^*}$, the history variables of plastic sampling beams in S^{k-1} are transferred to their counterparts in S^{k^*}. It is worth noting that since only refinement is considered and plasticity is restricted to FRDs, the FRDs monotonically increase and all sampling beams of FRDs in S^{k-1} are also sampling beams in S^{k^*}, which enables a straightforward transfer of beam history variables (see Fig. 4.4). Afterwards, the transferred history variables and the initial guess of $\mathbf{u}_{\text{r}}^{k^*}$ are put into Eq. (4.6) to generate an initial guess for $\mathbf{f}_{\text{int}}^{k^*}$.

In the following section, the proposed adaptive scheme will be applied to model the elastoplastic response of periodic lattices.

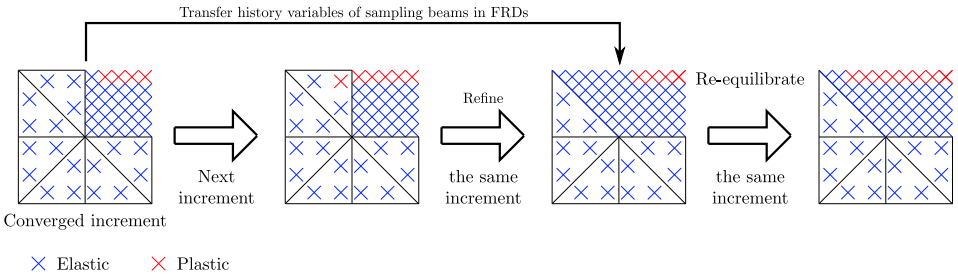

Figure 4.4: Illustration of transforming IPEs with plastic sampling beams into FRDs.

4.4. Elastoplastic response of large lattice structure

The upgraded AGQC is applied to simulate the elastoplastic scratching of a Kelvin lattice using a rigid sphere (the geometrical configuration of the Kelvin unit cell is the same as in Section 3.4). The categorizations of node types (for the purpose of applying GQC multi-field interpolation) and of beam types (for the purpose of

Algorithm 3: Adaptive scheme. The difference with Alg. 2 of Chapter 3 is indicated in blue.

Initialization prior to simulation: configure GQC model (Ω_0^{FRD}, Ω_0^{CGD}, τ_0, S^0), $\mathbf{u}_{\text{r}}^0 = \mathbf{0}$, $\mathbf{f}_{\text{int}}^0 = \mathbf{0}$.
for $k = 1,2,\ldots,n$ **do**
  Inherit GQC model ($\Omega_k^{\text{FRD}} \Leftarrow \Omega_{k-1}^{\text{FRD}}$, $\Omega_k^{\text{CGD}} \Leftarrow \Omega_{k-1}^{\text{CGD}}$, $\tau_k \Leftarrow \tau_{k-1}$, $S^k \Leftarrow S^{k-1}$), set initial guesses $\mathbf{u}_{\text{r}}^k \Leftarrow \mathbf{u}_{\text{r}}^{k-1}$, $\mathbf{f}_{\text{int}}^k \Leftarrow \mathbf{f}_{\text{int}}^{k-1}$.
  Apply boundary conditions at t_k.
  Equilibrate the GQC model by solving Eq. (4.9).
  Identify the IPEs with plastic sampling beams and collect them in set τ_{resolve}.
  while $\tau_{resolve} \neq \emptyset$ **do**
    Fully resolve IPEs in τ_{resolve}.
    Invoke subroutine in Alg. 4.
    Identify the IPEs with plastic sampling beams and collect them in set τ_{resolve}.
  Evaluate energy discrepancy κ for IPE-IPE interfaces in τ_{k}, identify the IPEs with $\kappa > \kappa_{\text{tol}}$ and collect them in set τ_{refine}.
  while $\tau_{refine} \neq \emptyset$ **do**
    Invoke refinement algorithm in Alg. 1 (see Section 3.3.2).
    Invoke subroutine in Alg. 4.
    Evaluate energy discrepancy κ for IPE-IPE interfaces in τ_{k}, identify the IPEs with $\kappa > \kappa_{\text{tol}}$ and collect them in set τ_{refine}.
  Evaluate energy discrepancy κ for IPE-FRD interfaces in τ_{k}, identify the IPEs with $\kappa > \kappa_{\text{tol}}$ and collect them in set τ_{resolve}.
  while $\tau_{resolve} \neq \emptyset$ **do**
    Fully resolve IPEs in τ_{resolve}.
    Invoke subroutine in Alg. 4.
    Evaluate energy discrepancy κ for IPE-FRD interfaces in τ_{k}, identify the IPEs with $\kappa > \kappa_{\text{tol}}$ and collect them in set τ_{resolve}.
  Store output data of current time step: Ω_k^{FRD}, Ω_k^{CGD}, τ_k, S^k, $\mathbf{u}_{\text{r}}^k$, $\mathbf{f}_{\text{int}}^k$.

evaluating the refinement indicator κ) in the Kelvin unit cell are shown in Fig. 3.9 and are not repeated here for the sake of brevity. Fig. 4.5 depicts the setup of the

Algorithm 4: Subroutine of structural re-equilibration.

Input: Refined by yet equilibrated GQC model ($\Omega_{k^*}^{\text{FRD}}$, $\Omega_{k^*}^{\text{CGD}}$, τ_{k^*}, S^{k^*}, $\mathbf{u}_{\text{r}}^{k^*}$, $\mathbf{f}_{\text{int}}^{k^*}$).

Input: GQC model of last converged increment ($\Omega_{k-1}^{\text{FRD}}$, $\Omega_{k-1}^{\text{CGD}}$, τ_{k-1}, S^{k-1}, $\mathbf{u}_{\text{r}}^{k-1}$, $\mathbf{f}_{\text{int}}^{k-1}$).

Output: Equilibrated GQC model (Ω_{k}^{FRD}, Ω_{k}^{CGD}, τ_{k}, S^{k}, $\mathbf{u}_{\text{r}}^{k}$, $\mathbf{f}_{\text{int}}^{k}$).

1 Compute interpolation matrix $\Phi_{k^*}^{k-1}$ between $\mathbf{u}_{\text{r}}^{k^*}$ and $\mathbf{u}_{\text{r}}^{k-1}$. Set the initial guess of $\mathbf{u}_{\text{r}}^{k^*}$ to be $\Phi_{k^*}^{k-1}\,\mathbf{u}_{\text{r}}^{k-1}$.

2 Transfer history variables of plastic sampling beams in $S^{\text{k-1}}$ to their counterparts in S^{k}.

3 Set the initial guess for $\mathbf{f}_{\text{int}}^{k^*}$ by solving Eq. (4.6).

4 Equilibrate the GQC model by solving Eq. (4.9).

scratch simulation. The depth of scratch (i.e. the penetration between the lowest point of the sphere and the surface of the lattice) is set to $0.1\ l_{\text{uc}}$ (l_{uc} denotes the length of a unit cell, $l_{\text{uc}} = 2$ mm). Only half of the lattice is considered thanks to the mirror plane symmetry. The contact between the rigid sphere and the beam FEs is frictionless and enforced using the penalty approach with a penalty stiffness of 10^3 N/mm. The (horizontal) displacement increment of the rigid sphere is set to $1.5\ l_{\text{uc}}$ and an automatic refinement of the increment is performed in case of divergence. The DNS includes 738 800 beam FEs and 2 272 800 DoFs and was not performed due to the required resources.

The initial setup of the AGQC model is shown in Fig. 4.6. An FRD of $10\times10\times10$ unit cells is located near the initial position of the rigid sphere, because contact is implemented between the sphere and the beams and not between the sphere and the IPEs. The rest of the domain is a CGD with a structured mesh of linear tetrahedral IPEs. 5 Gauss quadrature points (i.e. sampling unit cells) are adopted in each IPE.

4.4.1. Choice of control parameters of AGQC

Two control parameters (κ_{tol} and V_{tol}) need to be chosen for the AGQC simulation. κ_{tol} is the threshold of energy discrepancy for IPE-IPE and IPE-FRD interfaces. V_{tol} is the threshold below which an IPE is full resolved. Following the conclusion of Chapter 3 that a V_{tol} closer to its lower bound ($5l_{\text{uc}}^3$ in this case) yields more accurate results, and while ensuring that the IPEs (with volumes of $166l_{\text{uc}}^3$ in the initial mesh of Fig. 4.6) can be moderately refined before being fully resolved, V_{tol} is set to $10l_{\text{uc}}^3$ in this study.

The procedure for choosing an appropriate value for κ_{tol} is presented in the following. Specifically, to choose an appropriate κ_{tol}, the 1^{st} increment (during which contact is established) of the AGQC model of Fig. 4.6 is computed. The

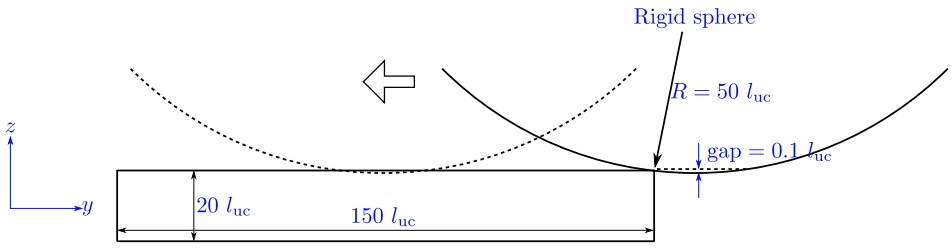

(a) Geometry of the scratch simulation, 2D view.

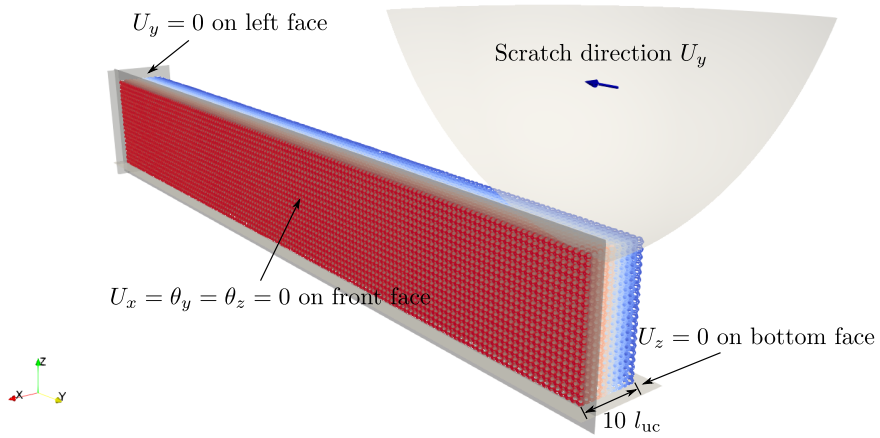

(b) 3D view.

Figure 4.5: Setup for scratching the Kelvin lattice using a rigid sphere.

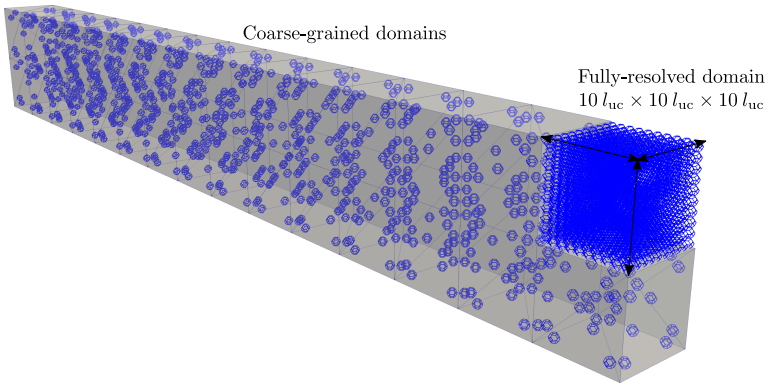

Figure 4.6: Initial configuration of the AGQC model for the elastoplastic scratch test. The distribution of sampling unit cells is also shown in blue.

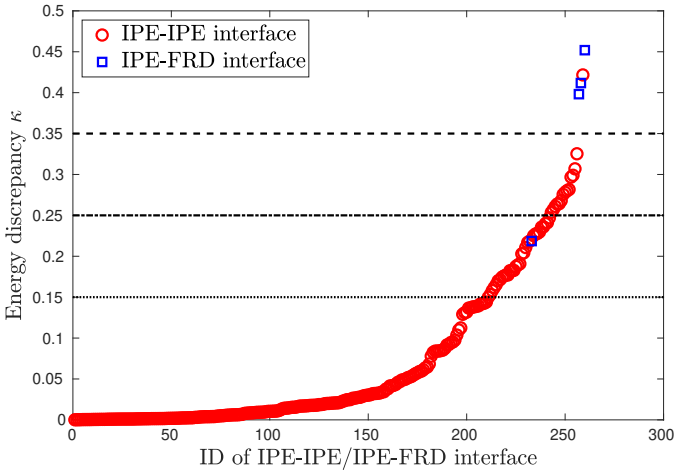

Figure 4.7: Distribution of energy discrepancy κ for IPE-IPE and IPE-FRD interfaces after the 1st increment of the AGQC model of Fig. 4.6. It is used to determine an appropriate value for κ_{tol} and predict corresponding extent of refinement.

resulting energy discrepancies of the IPE-IPE and IPE-FRD interfaces are presented in Fig. 4.7. It shows the range of the energy discrepancy at the beginning of the simulation. Three candidate values for κ_{tol} (0.15, 0.25 and 0.35) are chosen, which are expected to trigger different extents of refinement.

The CGDs and FRDs after refinement in the first increment are shown in Fig. 4.8. As expected, a small value for κ_{tol} value yields an increase of refinement. The overall time elapses of computing the 1st increment (on a server with a 18 cores Intel Xeon Gold 6140 @ 2.3 GHz CPU and 128 GB Kingston DDR4 @ 2666 MHz memory) are 3 224 seconds for $\kappa_{\text{tol}} = 0.35$, 6 043 seconds for $\kappa_{\text{tol}} = 0.25$ and 8 768 seconds for $\kappa_{\text{tol}} = 0.15$.

Fig. 4.9 shows the percentage difference of F_z (relative to F_z of $\kappa_{\text{tol}} = 0.15$), of the DoFs (relative to the DNS), of the sampling beams (relative to the DNS) and of the CGDs' volume (relative to the entire volume) as function of κ_{tol} for the 1st increment. F_z denotes the vertical contact force applied by the rigid sphere and is used as an indicator of the overall structural response. Smaller values for κ_{tol} yield more accurate simulations, but compromise the model reduction as it (most notably) increases the sizes of the FRDs.

As the vertical contact force hardly changes for the considered values for κ_{tol}, 0.35 is chosen as the optimal value for κ_{tol} to maximise the computational efficiency. However, since the DNS result is not available as reference, $\kappa_{\text{tol}} = 0.25$ is also considered in order to serve as reference.

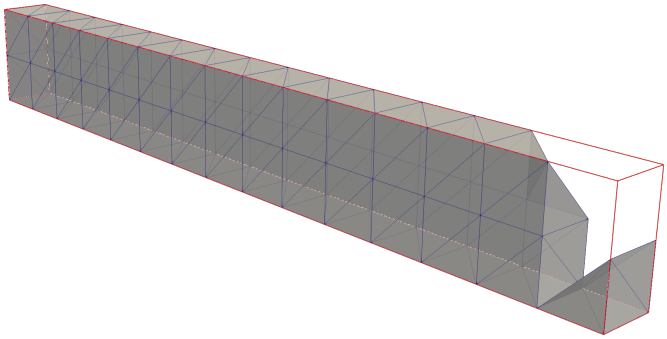

(a) $\kappa_{\text{tol}} = 0.35$, $V_{\text{tol}} = 10\ l_{\text{uc}}^3$.

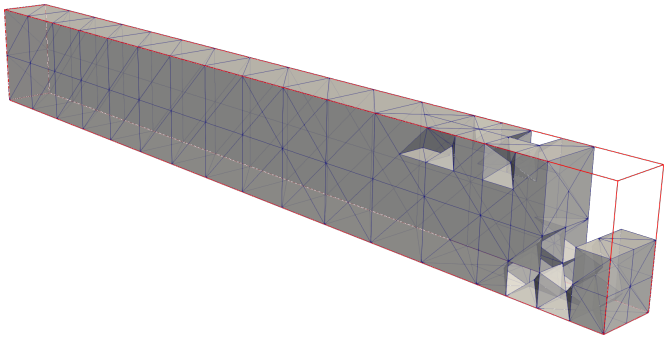

(b) $\kappa_{\text{tol}} = 0.25$, $V_{\text{tol}} = 10\ l_{\text{uc}}^3$.

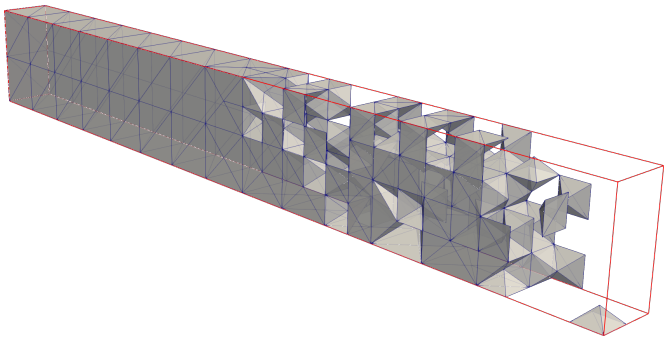

(c) $\kappa_{\text{tol}} = 0.15$, $V_{\text{tol}} = 10\ l_{\text{uc}}^3$.

Figure 4.8: IPEs after the 1st increment for different values for κ_{tol}. Voids represent FRDs.

4.4.2. Computational results of the elastoplastic scratch

The evolution of the IPEs and FRDs, of the deformation and of the plastic strains computed for the scratch test are presented in Fig. 4.10, clearly showing that the scratching induces strain localization just below the rigid sphere. The remaining (plastic) localization only reaches a few unit cells deep.

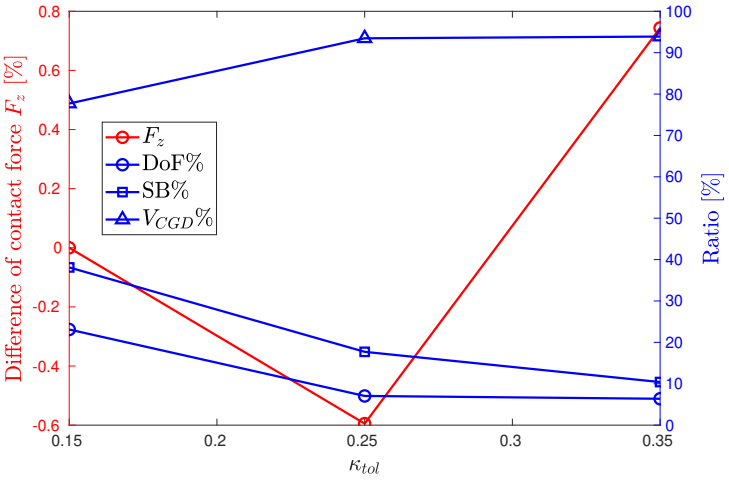

Figure 4.9: Percentage difference of: F_z (relative to F_z of $\kappa_{\text{tol}} = 0.15$), of the DoFs (relative to the DNS), of the sampling beams (relative to the DNS) and of the CGDs' volume (relative to the entire volume) as functions of κ_{tol} after refinement of the 1st increment.

The evolving IPEs and FRDs in the left column of Fig.4.10 clearly show the capacity of the enhanced AGQC to adapt the GQC model in the elastoplastic domain. The reasons for refinement are analyzed in detail later.

The vertical contact force versus the (horizontal) displacement of the rigid sphere is presented in Fig. 4.11, together with the number of active contact points. A comparison of the vertical and horizontal contact forces is shown in Fig. 4.12. In Fig. 4.11, the number of active contact points fluctuates. This is caused by the discrete nature of the lattice as beams come in and lose contact with the sphere during the sphere's horizontal movement. Note that the results for $\kappa_{\text{tol}} = 0.35$ and $\kappa_{\text{tol}} = 0.25$ are quite similar. This shows that $\kappa_{\text{tol}} = 0.35$ already leads to sufficiently accurate results. Synchronized periodic spikes can be observed for both F_y and F_z in Fig. 4.12. Although it is believed that the periodicity of the force response is caused by the periodicity of the lattice, a more thorough investigation will take place in the near future. Note furthermore that F_z is not presented in Fig. 4.12 as it is zero due to mirror plane symmetry.

Fig. 4.13 characterizes the progressive refinement of AGQC using the percentage of the DoFs, of the sampling beams and of the volume of the CGD. Throughout the scratch, more than 70% of the lattice is coarse grained. The number of sampling beams remains less than 50% of the DNS and the number of DoFs never exceeds 30% of the DNS. This constitutes a significant computational saving. The AGQC model for $\kappa_{\text{tol}} = 0.25$ is more refined compared to that of $\kappa_{\text{tol}} = 0.35$ because the percentages of the DoFs, of the sampling beams and of the volume of the CGDs are larger for $\kappa_{\text{tol}} = 0.25$. As can be seen, almost identical force–displacement curves

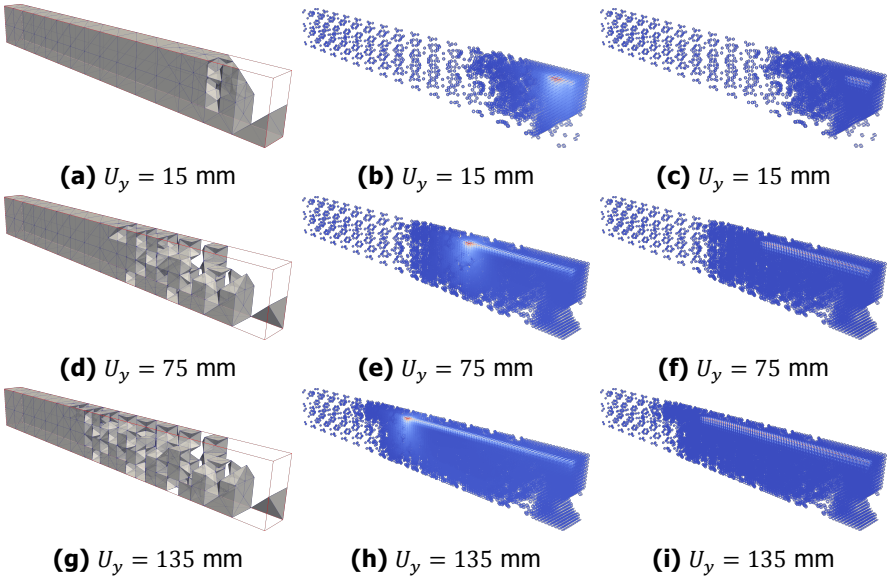

Figure 4.10: Results of AGQC simulation for $\kappa_{\text{tol}} = 0.35$ and $V_{\text{tol}} = 10\ l_{\text{uc}}^3$ as a function of the displacement of the rigid sphere (U_y). Left column: IPEs. Central column: displacement magnitude (i.e. $\sqrt{U_x^2 + U_y^2 + U_z^2}$) of sampling beams. The color bar ranges from 0 mm (blue) to 1.8 mm (red). Right column: average plastic strains in the sampling beams. The color bar ranges from 0 (blue) to 0.019 (red).

are obtained for $\kappa_{\text{tol}} = 0.35$ and $\kappa_{\text{tol}} = 0.25$, yet $\kappa_{\text{tol}} = 0.25$ leads to a substantially larger FRD volume fraction and hence, less computational savings. This confirms the validity of the aforementioned strategy when choosing the optimal value for κ_{tol}. Fig. 4.14 shows the number of refinement iterations per increment as the simulation proceeds. The total number of refinement iterations per increment is broken down into refinement iterations that occur in Loop 1 (refinement to forbid plasticity occurring in IPEs), Loop 2 (refinement because κ_{tol} is exceeded at IPE-IPE interfaces) and Loop 3 (refinement because κ_{tol} is exceeded at IPE-FRD interfaces), respectively. Fig. 4.14 shows that Loop 1 is a necessary enhancement to the refinement criterion of Chapter 3 if plasticity is to be restricted to FRDs. The AGQC of Chapter 3 alone was also applied to the scratch test but failed to converge. As can be seen from Fig. 4.14b, the refinement because κ_{tol} is exceeded at IPE-IPE interfaces occurs more often than refinement because κ_{tol} is exceeded at IPE-FRD interfaces. The latter, however, seems to occur more regularly. The refinement triggered by plasticity occurring in IPEs starts when the displacement of the rigid sphere reaches 20 mm and occurs regularly afterwards. The overall computational time of this example is approximately 360 hours with an in-house parallelized MATLAB codes running on 12 cores on the Hydra cluster (*https://hpc.vub.be/hydra.php*).

This computational example shows that the enhanced AGQC method is a pow-

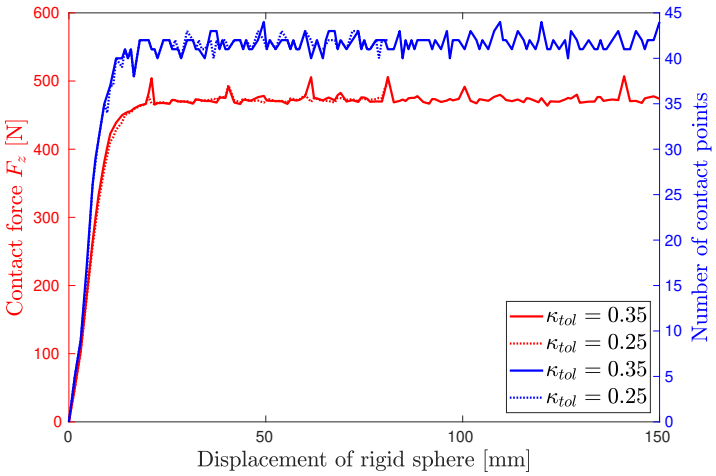

Figure 4.11: The vertical contact force F_z and the number of contact points as a function of the displacement of the rigid sphere. Only a displacement of up to 81 mm is considered for $\kappa_{\text{tol}} = 0.25$.

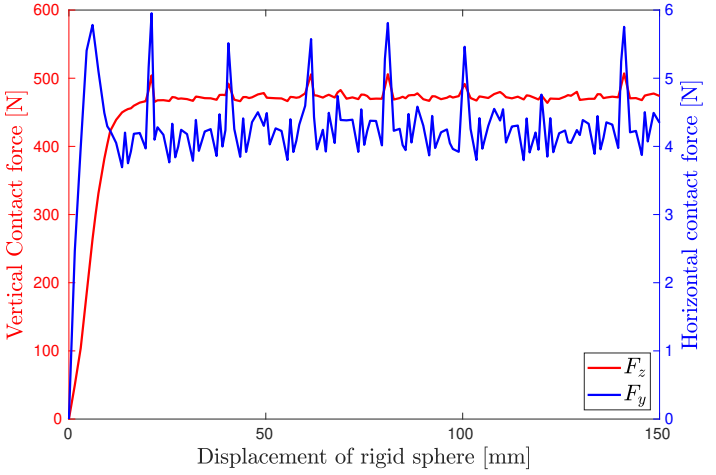

Figure 4.12: The vertical and horizontal contact forces as a function of the displacement of the rigid sphere for $\kappa_{\text{tol}} = 0.35$, $V_{\text{tol}} = 10l_{\text{uc}}^3$.

erful numerical tool to study the elastoplastic behavior of large structural lattices as it reduces the model size in terms of the number of DoFs and the number of sampling beams. More computational savings will occur for models in which localization occurs in smaller regions relative to the entire modelling domain. Vice

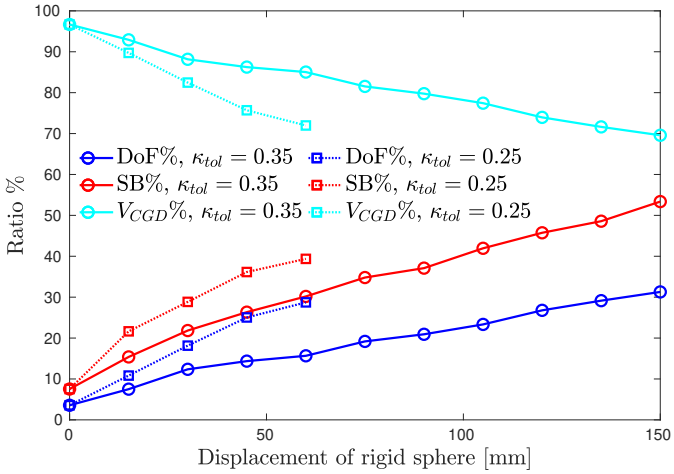

Figure 4.13: Percentages of the DoFs (relative to the DNS), of the sampling beams (relative to the DNS) and of the CGDs' volume (relative to the entire volume) as a function of the displacement of the rigid sphere. Only a displacement of up to 81 mm is considered for $\kappa_{\text{tol}} = 0.25$.

versa, if localization (e.g. long shear bands) appears throughout larger parts of the domain, less savings can be expected.

4.5. Conclusion and outlook

This work presents an essential improvement for the elastic adaptive generalized quasicontinuum method (AGQC) of Chapter 3 so that AGQC can account for elastoplastic periodic lattices with plasticity restricted to FRDs. To implement this improvement, all the sampling beams of interpolation elements (IPEs) in an AGQC model are monitored for plastic deformation. If any sampling beam of an IPE undergoes plastic deformation, the IPE is transformed into an FRD. Such an arrangement simplifies the transfer of history variables of sampling beams between the unrefined and refined GQC models. Because the history variables may only be non-zero in sampling beams of FRDs and the size of the FRDs monotonically increase, a plastic sampling beam of an FRD in the unrefined GQC model remains a sampling beam in the FRDs in the refined GQC model, for which the history variable can be directly inherited.

The enhanced AGQC was applied to study the behavior of an elastoplastic Kelvin lattice when it is scratched by a rigid sphere on the surface. It was shown that the lattice behavior can be simulated at a lower computational effort than direct numerical simulation (DNS) thanks to adaptive refinement. A detailed explanation of how to choose appropriate values for the control parameters (i.e. κ_{tol} and V_{tol}) of AGQC was also presented.

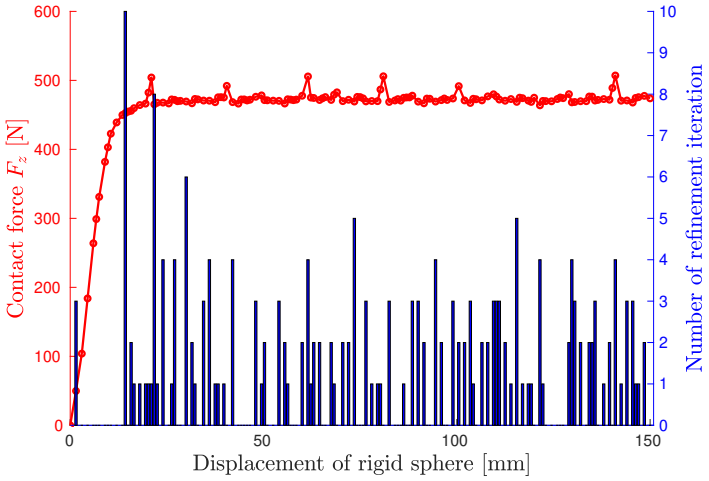

(a) The vertical contact force F_z and the number of refinement iterations as a function of the displacement of the rigid sphere. Each circle and bar corresponds to one increment.

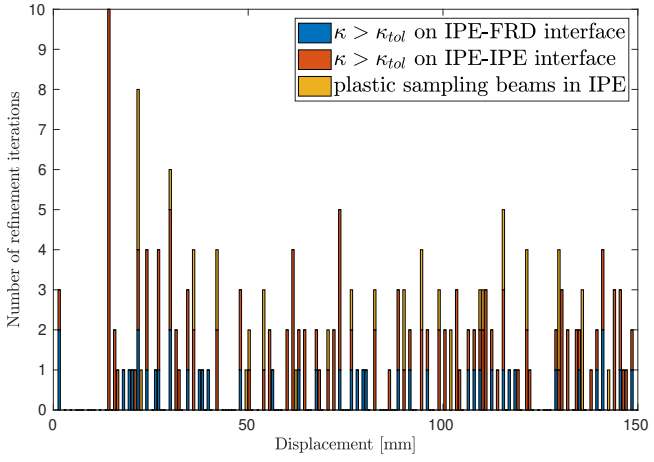

(b) Breaking down the number of refinement iterations according to the three loops in Alg. 3.

Figure 4.14: Refinement iterations in AGQC simulation of the scratch test using $\{\kappa_{\text{tol}} = 0.35, V_{\text{tol}} = 10\ l_{\text{uc}}^3\}$.

In future work, rather than restricting plasticity to the FRDs, the possibility of incorporating plasticity in coarse-grained domains (CGDs) can be further investigated. The coarsening of the elastoplastic AGQC model in the wake of refinement is a promising option to further boost the computational efficiency of AGQC, that can be examined in the future.

References

[1] M. Rashed, M. Ashraf, R. Mines, and P. Hazell, *Metallic microlattice materials: A current state of the art on manufacturing, mechanical properties and applications,* Materials & Design **95**, 518 (2016).

[2] C. M. Portela, J. R. Greer, and D. M. Kochmann, *Impact of node geometry on the effective stiffness of non-slender three-dimensional truss lattice architectures,* Extreme Mechanics Letters **22**, 138 (2018).

[3] H. D. Carlton, J. Lind, M. C. Messner, N. A. Volkoff-Shoemaker, H. S. Barnard, N. R. Barton, and M. Kumar, *Mapping local deformation behavior in single cell metal lattice structures,* Acta Materialia **129**, 239 (2017).

[4] R. Mines, *Some fundamental structural ideas for conventional metallic lattice structures,* in *Metallic Microlattice Structures: Manufacture, Materials and Application* (Springer International Publishing, Cham, 2019) pp. 7–15.

[5] P. Li, Z. Wang, N. Petrinic, and C. R. Siviour, *Deformation behaviour of stainless steel microlattice structures by selective laser melting,* Materials Science and Engineering: A **614**, 116 (2014).

[6] P. Li, *Constitutive and failure behaviour in selective laser melted stainless steel for microlattice structures,* Materials Science and Engineering: A **622**, 114 (2015).

[7] H. Cho, Y. Cho, and H. N. Han, *Finite element analysis for mechanical response of Ti foams with regular structure obtained by selective laser melting,* Acta Materialia **97**, 199 (2015).

[8] M. R. Karamooz-Ravari and M. Kadkhodaei, *A computationally efficient modeling approach for predicting mechanical behavior of cellular lattice structures,* Journal of Materials Engineering and Performance **24**, 245 (2015).

[9] M. R. Karamooz-Ravari and M. Kadkhodaei, *Finite element modeling of the elastic modulus of T-6Al-4V scaffold fabricated by SLM,* in *Fifth Biot Conference on Poromechanics*, edited by C. Hellmich, B. Pichler, and D. Adam, Technische Universitat Wein (American Society of Civil Engineers, Reston, Virginia, U.S., 1993) pp. 1021–1028, https://ascelibrary.org/doi/pdf/10.1061/9780784412992.122 .

[10] L. Liu, P. Kamm, F. García-Moreno, J. Banhart, and D. Pasini, *Elastic and failure response of imperfect three-dimensional metallic lattices: the role of geometric defects induced by selective laser melting,* Journal of the Mechanics and Physics of Solids **107**, 160 (2017).

[11] G. Campoli, M. S. Borleffs, S. A. Yavari, R. Wauthle, H. Weinans, and A. A. Zadpoor, *Mechanical properties of open-cell metallic biomaterials manufactured using additive manufacturing,* Materials & Design **49**, 957 (2013).

[12] M. Smith, Z. Guan, and W. J. Cantwell, *Finite element modelling of the compressive response of lattice structures manufactured using the selective laser melting technique,* International Journal of Mechanical Sciences **67**, 28 (2013).

[13] T. Tancogne-Dejean, A. B. Spierings, and D. Mohr, *Additively-manufactured metallic micro-lattice materials for high specific energy absorption under static and dynamic loading,* Acta Materialia **116**, 14 (2016).

[14] L. A. A. Beex, R. H. J. Peerlings, and M. G. D. Geers, *A multiscale quasicontinuum method for dissipative lattice models and discrete networks,* Journal of the Mechanics and Physics of Solids **64**, 154 (2014).

[15] O. Rokoš, L. A. A. Beex, J. Zeman, and R. H. J. Peerlings, *A variational formulation of dissipative quasicontinuum methods,* International Journal of Solids and Structures **102-103**, 214 (2016).

[16] L. A. A. Beex, P. Kerfriden, T. Rabczuk, and S. P. A. Bordas, *Quasicontinuum-based multiscale approaches for plate-like beam lattices experiencing in-plane and out-of-plane deformation,* Computer Methods in Applied Mechanics and Engineering **279**, 348 (2014).

[17] L. A. A. Beex, O. Rokoš, J. Zeman, and S. P. A. Bordas, *Higher-order quasicontinuum methods for elastic and dissipative lattice models: uniaxial deformation and pure bending,* GAMM-Mitteilungen **38**, 344 (2015), https://onlinelibrary.wiley.com/doi/pdf/10.1002/gamm.201510018 .

[18] L. Chen, L. A. Beex, P. Z. Berke, T. J. Massart, and S. P. Bordas, *Generalized quasicontinuum modeling of metallic lattices with geometrical and material nonlinearity and variability,* Computer Methods in Applied Mechanics and Engineering **366**, 112878 (2020).

[19] J. M. Battini and C. Pacoste, *Plastic instability of beam structures using co-rotational elements,* Computer Methods in Applied Mechanics and Engineering **191**, 5811 (2002).

[20] A. Mazzia and G. Pini, *Product gauss quadrature rules vs. cubature rules in the meshless local petrov–galerkin method,* Journal of Complexity **26**, 82 (2010).

5

Conclusions & Outlook

This chapter summarizes the conclusions that are derived from the development and application of the proposed adaptive generalized QC approach and lists a selection of identified future improvements.

The aim of this work was to develop a multi-scale computational tool to predict the mechanical behavior of periodic metallic lattices. Discrete geometrically nonlinear beam finite element (FE) networks were used to represent the unit cell (i.e. the smallest repeating volume of the periodic lattice) by representing each strut as a string of beam FEs. Since struts can have a varying diameter along their length due to the additive manufacturing process, the beam FEs in the numerical model can have different radii. Directly exploiting the discrete beam network description for industrially relevant (i.e. large) models is computationally prohibitive. To decrease the computational times, this thesis presents a generalization of the quasicontinuum (QC) method incorporating adaptivity in the elastoplastic domain.

Conventional QC does not allow incorporating several beam FEs along a strut, which substantially restricts the method's applicability. The presented work has successfully closed this gap in the literature by the proposal of a multi-field generalization of the method (Chapter 2). Moreover, a new adaptive refinement of the spatial representation (i.e. the division of the fully-resolved domains and coarse-grained domains, as well as the mesh of the interpolation elements in the coarse-grained domains) for the proposed generalized QC was proposed to enhance computational efficiency while maintaining a controlled accuracy for elastic (Chapter 3) and elastoplastic (Chapter 4) simulations in which localization spatially evolves. Whereas most previous refinement indicators for adaptivity in QC are defined in terms of quantities relevant for atomistics, the refinement indicators proposed in this thesis are widely applicable, as they can be exploited for elastic and elastoplastic lattices and for conventional as well as for the generalized QC method. The refinement indicators are original as they utilize so-called signalling unit cells, whose purpose is to flag domains for refinement. Thanks to the signalling unit cells employing co-rotational beam FE, the proposed refinement indicator is furthermore insensitive to rigid body rotations and translations, as well as to homogeneous deformation – something that cannot be said for all indicators in the literature.

Although metallic BCC (body centered cubic) and Kelvin lattices were considered in this work, it is emphasized that the proposed computational framework is independent from the base material and the shape of the unit cell for the lattice structure (although for other base materials and unit cell configurations differences in computational saving and accuracy may be observed). It is also worth to mention that besides the computational developments on the adaptive generalized QC method, two 3D co-rotational elastoplastic beam FEs were formulated and implemented in order to account for the geometrical and material nonlinear strut behaviors.

Other salient conclusions can be listed as follows:

- (1) Compared to conventional multi-scale approaches based on the computational homogenization, the generalized QC method does not require scale-separation. It is also as straightforward to implement for interpolation elements with higher-order polynomial interpolations as for interpolation elements with linear interpolation scheme. As most nested, concurrent multi-scale approaches, the generalized QC method requires smooth deformation fluctuations in the coarse-grained domains. Consequently, fully-resolved domains must be large enough to embrace localization (e.g. due to plasticity or

fracture). The approach is thus computationally most beneficial if the fully-resolved domain is small compared to the coarse-grained domain (as is the case for conventional nested, concurrent approaches).

- (2) The (adaptive) generalized QC frameworks were applied to elastoplastic lattice structures, which has shown that adaptive generalized QC is able to predict the failure modes of metallic lattice structures, e.g. buckling and plastic bending of individual struts. The number of degrees of freedom (DoFs) and the number of sampling beams (i.e. the beams exploited to approximate the governing equations) relative to the direct numerical simulations (DNS) were drastically reduced, whilst a high accuracy was maintained. It is worth noting that the lattices investigated in the present work remain of limited size, implying that an even larger computational saving is expected for true product-size models.

- (3) If the response of the unit cells is local (e.g. Kelvin unit cell), more significant model reduction can be achieved using the adaptive generalized QC framework, compared to lattices with a more nonlocal response (e.g. BCC unit cell). It was shown that the adaptive generalized QC frameworks are capable of tackling model sizes out of reach of DNS, by employing an automatic adaptation of the spatial discretization (interpolation elements in the coarse-grained domains and fully resolved domains are updated on the fly).

- (4) Interpolation element refinement is triggered when the relative difference between the energies of a signaling unit cell reaches a user defined threshold. If the volume of a newly created interpolation element falls below a user defined minimum, the interpolation element is fully resolved. This prompts fully-resolved domains to both evolve and be created where necessary.

- (5) The examples have revealed that the two user defined thresholds of the adaptivity have a fundamental impact on the performance. The influence of the selected values for the two thresholds is however case specific and depend on the shape of the unit cell, the beam discretization of the unit cell and the size of the lattice. A detailed explanation of how to choose appropriate values for the two thresholds was presented for the studied cases.

- (6) In the current implementation plasticity is restricted to the fully-resolved domains and therefore all sampling beams in interpolation elements are monitored for any plastic deformation. If any sampling beam in an interpolation element deforms plastically, the interpolation element is fully resolved. The advantage of restricting plasticity to develop in fully-resolved domains is the straightforward transfer of history variables between current and future refinements.

Based on the presented work, it seems beneficial to improve the adaptive generalized QC framework as follows:

- Rather than restricting plasticity to the fully-resolved domains, it is expected that if plasticity can also take place in coarse-grained domains, the resulting computational savings are higher. This would require i) a robust, yet more complicated transfer of the history variables between plastified sampling beams in an interpolation element and the new sampling beams that are generated as a result of the refinement of this interpolation element, as well as, ii) an extension of the refinement indicator towards dissipation.

- The coarsening of the adaptive generalized QC model in the wake of localization (e.g. behind the contact zone in a scratch simulation) is a promising option to further boost the computational efficiency. This would require i), a coarsening indicator in contrast to a refinement indicator, which decides on whether 1) smaller interpolation elements can be merged into larger interpolation elements, 2) fully-resolved domains can be replaced using interpolation elements at no expense of accuracy; ii) another type of transfer of history variables in which history variables of many sampling beams must be condensed to those of a few sampling beams.

To further assess the performance of the adaptive generalized QC framework it would also be interesting to validate the framework based on an experimentally tested lattice. More specifically, the compression test on pre-damaged lattices would be of great interest. To have a guided initiation of failure, removing certain struts to deliberately create weak spots in the lattice at which damage is triggered would make the experiments easier to model by QC. In this way, not only can the comparison between the experimental and numerical results be set on a sound basis, but the performance of the proposed adaptivity can be assessed by a direct experimental-numerical comparison of the evolution of localized deformation.

Other than the experimental validation, it would be scientifically challenging and useful if the beam representation of the struts could directly be obtained from 3D CT scans. This would require the development of a methodology, which statistically relates the strut morphology observed in the scans to the beam geometry in QC.

Another relevant future work is to compare the mechanical behavior of bending dominated and stretch dominated lattices using the proposed numerical framework. For bending dominated lattices the structural response is mainly determined by the bending resistance of the struts, while for stretch dominated lattices the structural response is more impacted by the tensile or compressive strength and local buckling in the struts. It would be interesting to see how these different underlying mechanisms can be captured by QC.

Acknowledgements

I owe my deepest gratitude to so many people, without whom this thesis would not have been possible. I would like to say big thanks to all of them from the bottom of my heart.

I am deeply grateful to my supervisor, Prof. Thierry J. Massart, for bringing me onboard such a challenging and meaningful PhD adventure. I feel so lucky to work with you, to be inspired by your meticulous working style. I am sure I will benefit from all of these for the rest of my life.

I am truly thankful to Prof. Péter Z. Berke for always being ready to advise me and show me the light. Working with you has been such a great pleasure for me and I am sure every member of SMC feels the same. You and Fernanda have made my expat life in Brussels so vivid.

I am sincerely grateful to Dr. Lars A. A. Beex for your professional guidance and admirable patience when presenting me the QC Universe. Working with you has been such an enjoyable experience, not to say your great sense of humor.

I am truly grateful to my supervisor, Prof. Stéphane P. A. Bordas, for welcoming me in the LegoTeam. There are so many outstanding researchers in the LegoTeam, from whom I could learn a lot. Moreover, I am deeply inspired by your devotion to research.

The countless hours of discussion with all of you has been such an invaluable part of my PhD experience and a precious inspiration for my professional career.

Next, I would like to thank all the administrators and secretaries at ULB and UniLu, who have offered their help for my paperwork. In particular, I do appreciate the help of Isabelle Toussaint, Dominique Pierson, Sue Black and Shayan Weber. I am also appreciative of Guy Paulus. He is a great helper whenever I encountered technical difficulties.

I sincerely thank Prof. Bertrand Francois, for chairing my PhD accompany committee at ULB, and Prof. Ludovic Noels, for the fruitful discussions at all of the EnlightenIt meetings.

I wish to thank my colleagues and friends at both ULB and UniLu, Batoma, Roland, Liesbeth, Anqi, Rohith, Ygee, Arash I, Arash II, Karim, Gerrit, Alexis, Marco, Benjamin, Jinyuan, Chensen, Haojie, Renaldo, Soumi, for contributing to a pleasant and social life.

I also wish to express my gratitude to FNRS of Belgium and FNR of Luxembourg for sponsoring our research.

My gratitude to my family is beyond the description of words. They are more than ready to listen to me and encourage me to overcome countless difficulties. They are the source of my power.

Li Chen

Belval, August 2020.

Curriculum Vitæ

Li Chen

Li Chen was born on 1st July 1990 in Tiantai County, Zhejiang Province, China. After completing his high school education in 2009, he entered the South China University of Technology in Guangzhou, China. After four years of undergraduate education, he obtained a Bachelor degree in Water Resources and Hydropower Engineering from the School of Civil Engineering & Transportation. He started his master in 2013 at Wuhan Institute of Rock and Soil Mechanics, Chinese Academy of Sciences in Wuhan, China. His master thesis, "Meso-structural modeling of soil-rock mixtures and study on its meso-structural mechanics based on Numeric Manifold Method", was carried out under the supervision of Dr. Hong Zheng, now a professor in the College of Architecture & Civil Engineering, Beijing University of Technology. In 2016 he moved to Belgium where he was appointed as a PhD researcher and started his four-year PhD project. He worked on quasicontinuum modeling of periodic lattice structures under the joint supervision of Prof. Thierry J. Massart and Prof. Péter Z. Berke at the Department of Building, Architecture and Town Planning, Université Libre de Bruxelles, as well as Prof. Stéphane P. A. Bordas and Dr. Lars A. A. Beex at the Faculty of Science, Technology and Medicine, Université du Luxembourg. The obtained results during his PhD are presented in this dissertation.